

**UNDERWATER ACOUSTIC COMMUNICATIONS IN
WARM SHALLOW WATER CHANNELS**

MANDAR CHITRE
B. Eng. (Hons), M. Eng., M. Sc.

A THESIS SUBMITTED FOR THE DEGREE OF
DOCTOR OF PHILOSOPHY

ELECTRICAL & COMPUTER ENGINEERING
NATIONAL UNIVERSITY OF SINGAPORE

2006

Acknowledgements

Although the completion of a Ph.D. is looked upon as an individual accomplishment, it is rarely achieved without the help of many people. The research presented in this thesis is no exception.

I would like to thank my supervisors, A/Prof. Ong Sim Heng and A/Prof. John Potter, for their support and guidance in my academic pursuits. A/Prof. Ong Sim Heng has supported me through several projects over the past years, allowing my research interests in underwater acoustics and digital image processing an avenue for growth. A/Prof. John Potter introduced me to underwater acoustics and guided me through the learning process involved in theoretical and experimental aspects of the subject. Without his mentoring and support, I would not be pursuing independent research in this field today.

I would also like to thank Prof. Chan Eng Soon, who first recognized my research interests during my undergraduate studies and helped me find numerous opportunities to further them. He has since supported me in several endeavors, eventually leading to my current research in underwater acoustics.

I would like to express my gratitude towards the DSTA^a and the ARL^b for supporting most of the research presented in this thesis. Mr. Shiraz Shahabudeen, Dr. Venugopalan Pallayil, Mr. Koay Teong Beng, Ms. Tan Soo Pieng, Dr. Paul Seekings, Mr. Alan Low and Mr. Mohan Panayamadam contributed to numerous discussions, experimental deployments and data collection in support of this project, for which I am grateful.

^a Defence Science & Technology Agency (DSTA), Singapore – <http://www.dsta.gov.sg>

^b Acoustic Research Laboratory (ARL), Tropical Marine Science Institute (TMSI), National University of Singapore (NUS) – <http://www.arl.nus.edu.sg>

I would also like to thank Prof. Lawrence Wong and Dr. Goh Joo Thiam, who kindly agreed to find time from their busy schedules to help monitor the technical progress during the course of the research. Their comments and feedback during the Ph.D. qualification defense proved valuable in helping define some of the key research directions for the project.

Lastly, I would like to thank my lovely wife, Yun Ping, and my loving parents for their support, understanding and unconditional love. Without them, none of this work would have been possible.

Table of Contents

Summary.....	5
List of Tables	7
List of Figures.....	8
Abbreviations and Symbols	11
1. Introduction.....	1
1.1. Motivation.....	1
1.2. Objectives	2
1.3. Thesis Contributions	2
1.4. Thesis Organization	4
2. Background	5
2.1. Brief History	5
2.2. Review of Research in UWA Communications	5
2.3. Signal Processing in Impulsive Noise.....	11
2.4. Practical Considerations.....	14
2.5. Performance of Modems in Singapore Waters	16
2.6. Conclusions.....	20
3. Ambient Noise Model	22
3.1. Power Spectrum	22
3.2. Probability Distribution	24
3.3. The S α S Noise Model.....	26
3.4. Properties of the S α S Random Variables	30
3.5. Signal-to-Noise Ratio.....	33
3.6. Conclusions.....	34
4. Signal Detection in SαS Noise	36
4.1. Signal Detection.....	36
4.2. Locally Optimal Detector	36
4.3. Maximum Likelihood Estimator.....	38
4.4. Sign Correlation Detector	39
4.5. Simulated Detection Performance	39
4.6. Experimental Validation	43
4.7. Conclusions.....	44
5. Communication in SαS Noise	45

5.1. Antipodal Signaling	45
5.2. Tail Probability of S α S Noise.....	46
5.3. Antipodal Signaling in S α S Noise.....	47
5.4. Coded Communications in S α S Noise	50
5.5. Conclusions.....	64
6. Channel Model	65
6.1. Physical of Underwater Acoustic Propagation	65
6.2. Channel Measurements.....	70
6.3. Time-varying Channel	77
6.4. The Channel Model.....	80
6.5. Comparison with Experimental Data.....	82
6.6. Conclusions.....	85
7. Proposed Communication Scheme	87
7.1. Communication Scheme	87
7.2. Selection of Parameters.....	97
7.3. Simulations	102
7.4. Conclusions.....	107
8. Experimental Results.....	109
8.1. Sea Trial 1	109
8.2. Sea Trial 2	117
8.3. Conclusions.....	125
9. Conclusions & Further Research	126
9.1. Conclusions.....	126
9.2. Further Research	128
Bibliography	130
Appendix A: Simulation of a Random Process with Exponential Correlation..	137
Appendix B: Related Publications.....	140

The ability to communicate effectively underwater has numerous applications for marine researchers, oceanographers, marine commercial operators, off-shore oil industry and defense organizations. As electromagnetic waves propagate poorly in sea water, acoustics provides the most obvious choice of medium to enable underwater communications. Underwater acoustic (UWA) communications has been a difficult problem due to unique channel characteristics. Attempts at adapting communication techniques developed for other channels have yielded successful implementations in vertical deep water channels, but have had limited success in shallow water channels. One of the most challenging UWA communication channels is the medium-range very shallow warm water channel, common in tropical coastal regions such as Singapore. This warm shallow water acoustic (WSWA) channel exhibits two key features – extensive time-varying multipath and high levels of non-Gaussian ambient noise due to snapping shrimp – both of which limit the performance of traditional communication techniques.

We develop a physics-based channel model for the WSWA channel. The model also includes time-varying statistical effects observed during channel studies. The model is calibrated and its accuracy validated using channel measurements made at sea. In contrast with most UWA communications research which assumes Gaussian noise, we model the ambient noise as a symmetric α -stable ($S\alpha S$) noise. We show that this model accurately describes the ambient noise found in WSWA channels. This has profound implications on the design of communication systems for the WSWA channel. Many commonly used techniques such as the linear correlator and the soft-decision Viterbi algorithm with Euclidean branch metric perform poorly the

in presence of S α S noise. We develop computationally efficient near-optimal solutions such as the sign correlator for detection and the 1-norm Viterbi decoder for decoding convolutional codes in the presence of S α S noise.

Based on our channel and noise models, we develop an orthogonal frequency division multiplexing (OFDM) based communication scheme for use in WSWA channels. We adopt differential quadrature phase shift keying (QPSK) and a cyclic prefix to eliminate the need for an equalizer. We use a convolutional code and a channel interleaver to benefit from the time-frequency diversity available in the channel. The 1-norm Viterbi decoder ensures good decoding performance in impulsive noise. We adapt a method to use the cyclic prefix for symbol synchronization in the presence of S α S noise.

Given estimates of channel coherence time and delay spread, we suggest an approach to determine the OFDM parameters to use. We use the channel model to simulate OFDM communications with the chosen parameters prior to field deployments. We tested the method via an experiment at sea. More than 27 kb of data was transmitted without errors at a data rate of 7.6 kbps at a range of 1 km. More than 54 kb of data was transmitted at 15 kbps and a BER of 10^{-4} or better at a range of 800 m. Thus, we demonstrated reliable communications in very shallow waters in Singapore at ranges of 800 m and 1 km. This is a large improvement when compared to the performance of the best commercial modems in similar environments.

List of Tables

Table 2.1. Sea trial results for the Evologics S2C modem	20
Table 6.1. Simulation parameters	83
Table 6.2. Comparison of simulated channel statistics against experimental channel statistics	85
Table 7.1. Simulated performance of various OFDM schemes at 1 km range using soft-decision Viterbi decoding with 1-norm metric	107
Table 8.1. Measured channel coherence time and delay spread	111
Table 8.2. Comparison of measured delay spreads against predictions based on simulation	112
Table 8.3. Raw performance of OFDM with differential PSK during Sea Trial 1	114
Table 8.4. Coded performance of OFDM with differential PSK during Sea Trial 1.	115

List of Figures

Figure 2.1. Attenuation of sound in shallow warm sea water.....	15
Figure 2.2. Sea trial setup for Evologics S2C modem (side view).....	19
Figure 3.1. Ambient noise PSD for a coral reef site	22
Figure 3.2. Ambient noise PSD for a shipping anchorage and channel	23
Figure 3.3. Normal probability plot of acoustic pressure of ambient noise.....	25
Figure 3.4. Best Gaussian fit for probability density of ambient noise	25
Figure 3.5. Best S α S fit for probability density of ambient noise	28
Figure 3.6. Amplitude probability plot of snapping shrimp dominated ambient noise showing that the probability distribution can be well approximated using a S α S distribution	29
Figure 4.1. Sample LO transfer function for S α S with $\alpha = 1.5$ and $c = 1$	37
Figure 4.2. Detection performance for ML, LO, SC and LC detectors at SNR of 5 dB	40
Figure 4.3. Detection performance for ML, LO, SC and LC detectors at SNR of 10 dB	41
Figure 4.4. Detection performance for ML, LO, SC and LC detectors at SNR of 15 dB	41
Figure 4.5. Performance of a detector based on ML, LO, SC and LC	42
Figure 5.1. Detection performance for antipodal signaling in AWS α SN for various values of α - based on Q_α , Cauchy upper bound, asymptotic approximation, performance in Gaussian noise and simulation results	49
Figure 5.2. Uncoded performance, theoretical upper bound and simulation results for hard-decision decoding	60
Figure 5.3. Uncoded performance, theoretical upper bound, closed-form approximation and simulation results for 1-norm decoding	61
Figure 5.4. Performance of uncoded system in comparison to coded system with hard- decision decoding, Euclidean metric, 1-norm metric and ML decoding in presence of Gaussian noise	62
Figure 5.5. Performance of uncoded system in comparison to coded system with hard- decision decoding, Euclidean metric, 1-norm metric and ML decoding	63

Figure 6.1. Schematic showing a Pekeris waveguide model of the WSWA channel..	66
Figure 6.2. A typical sound speed profile from Singapore waters showing variation of less than 1 m/s over the depth of the water column	67
Figure 6.3. Multipath arrival structure for 100 signal transmissions at 50 m and 100 m range.....	72
Figure 6.4. Cumulative distribution function of signal strength showing fading behavior of direct arrival at 50 m.....	74
Figure 6.5. Cumulative distribution function of signal strength showing fading behavior of the combined arrival at 1020 m, compared against Rayleigh fading and simulated 2-path Rayleigh fading	76
Figure 6.6. Comparison of multipath arrival structure between experiment and simulation.....	84
Figure 7.1. Statistic Λ shows a peak at the start of each OFDM symbol	94
Figure 7.2. Overview of proposed OFDM communication scheme	96
Figure 7.3. Ratio L_A/N_A plotted as a function of frequency at various transmission ranges	98
Figure 7.4. A plot of various OFDM schemes on a N_c - N_p plane and constraint boundaries for good performance marked for $\tau_c = 70$ ms, $\tau_{ds} = 1.5$ ms and $W = 25$ kHz.....	101
Figure 7.5. Encoder and decoder structures for serial concatenated convolutional codes	103
Figure 7.6. Simulation results showing raw BER for 11 OFDM schemes at 1 km range	104
Figure 7.7. Simulation results showing raw BER as a function of range for various OFDM schemes with $N_p = 32$	105
Figure 7.8. Simulation results showing the 1/3 rate coded performance of OFDM with $N_c = 128$, $N_p = 32$ with hard-decision decoding, soft-decision decoding with Euclidean norm and soft-decision decoding with 1-norm	106
Figure 8.1. Schematic representation of the setup for Sea Trial 1	110
Figure 8.2. Performance of differential BPSK, QPSK and 8-PSK based OFDM schemes with different degrees of coding.....	116
Figure 8.3. Performance of OFDM-128/32 at 800 m range without coding	119
Figure 8.4. Performance of OFDM-128/32 at 800 m range with 1/3 rate coding	120
Figure 8.5. Performance of OFDM-512/32 at 800 m range without coding	120

Figure 8.6. Performance of OFDM-512/32 at 800 m range with 1/3 rate coding	121
Figure 8.7. Performance of OFDM-128/32 at 1 km range without coding	122
Figure 8.8. Performance of OFDM-128/32 at 1 km range with 1/3 rate coding	123
Figure 8.9. Performance of OFDM-512/32 at 1 km range without coding	124
Figure 8.10. Performance of OFDM-512/32 at 1 km range with 1/3 rate coding	124

Abbreviations and Symbols

Abbreviations

ARL	Acoustic Research Laboratory
AWGN	additive white Gaussian noise
AWS α SN	additive white symmetric α -stable noise
BER	bit error rate
bps	bits per second
BPSK	binary phase shift keying
BSC	binary symmetric channel
CDF	cumulative distribution function
DFT	discrete Fourier transform
DPSK	differential phase shift keying
DSSS	direct sequence spread spectrum
DSTA	Defence Science and Technology Agency
FDM	frequency division multiplexing
FHSS	frequency hopping spread spectrum
FLOM	fractional low-order moment
FIR	finite impulse response
GPS	global positioning system
IDFT	inverse discrete Fourier transform
i.i.d.	identical and independently distributed
ISI	inter-symbol interference
kbps	kilobits per second
LC	linear correlator
LO	locally optimal
MIMO	multiple input multiple output
ML	maximum likelihood
OFDM	orthogonal frequency division multiplexing
PAPR	peak-to-average power ratio
PDF	probability density function
PSD	power spectral density

PSK	phase shift keying
QPSK	quadrature phase shift keying
SISO	single input single output
SOVA	soft output Viterbi algorithm
RMS	root mean square
S α S	symmetric α -stable
SC	sign correlator
SNR	signal-to-noise ratio
TRM	time reversal mirror
UWA	underwater acoustic
WSWA	warm shallow water acoustic

Commonly Used Symbols

α	Characteristic exponent of the S α S distribution
γ	Dispersion of the S α S distribution
f_α	S α S probability density function (PDF)
F_α	S α S cumulative density function (CDF)
Q_α	Tail probability function for the S α S distribution
c	Speed of sound in water
R	Code rate
E_b	Energy per data bit
E_c	Energy per coded bit
N_0	Spectral noise level
P_b	Probability of bit error
p_d	Pairwise probability of error between codewords
N_c	Number of OFDM carriers
N_p	OFDM cyclic prefix length
W	Bandwidth
τ_{ds}	Delay spread of the channel
τ_c	Coherence time of the channel

1. Introduction

1.1. Motivation

The ability to communicate effectively underwater has numerous applications for marine researchers, oceanographers, marine commercial operators, off-shore oil industry and defense organizations. As electromagnetic waves cannot propagate over long distances in sea water, acoustics provides the most obvious choice of energy propagation to enable underwater communications.

Underwater acoustic (UWA) communications has been a difficult problem due to unique channel characteristics such as fading, extended multipath and refractive properties of the sound channel [1;2]. Attempts at adapting communication techniques developed for other channels have yielded successful implementations in vertical deep water channels, but have had limited success in shallow^{*} water channels [2-4]. One of the most challenging UWA communication channel is believed to be the medium range[†] very shallow[‡] warm water channel, common in tropical coastal regions such as Singapore waters. This warm shallow water acoustic (WSWA) channel presents two key features – extensive time-varying multipath [5] and high levels of non-Gaussian ambient noise due to snapping shrimp [5-7] – both of which limit the performance of traditional communication techniques.

Several commercial and research acoustic modems are available for use in deep waters and some are available for use in shallow waters. Although the shallow water modems demonstrate good performance in some shallow water environments, many

^{*} Water depths of 50 m to 200 m are considered *shallow*.

[†] Distances in the range of 200 m to 2 km are considered to be *medium range*.

[‡] Water depths of less than 50 m are considered *very shallow*. Most coastal regions in Singapore have water depth of less than 30 m.

of them perform poorly in Singapore waters. The research presented here seeks to better understand the warm shallow water environment in Singapore and develop suitable channel propagation and noise models. It also aims to develop a communication scheme that would provide robust performance in such environments.

Although directional receivers and spatially distributed transmitters and receivers can significantly improve communication performance, we focus our efforts on the development of communication systems with a single omni-directional transducer. Such single-input-single-output (SISO) communication systems tend to yield relatively small, portable and low-cost implementations which are important in many underwater applications.

1.2. Objectives

With an aim to develop a better understanding of acoustic communications in WSWA channels, the primary objectives of the project are as follows.

- ∞ To develop an ambient noise model for warm shallow waters.
- ∞ To develop signal processing techniques to communicate effectively in presence of non-Gaussian ambient noise.
- ∞ To develop a time-varying multipath propagation model for the medium range very shallow water environment.
- ∞ To develop techniques for reliable high-performance communications in WSWA channels.

1.3. Thesis Contributions

Communication systems have been the subject of study for many decades. Most communication systems have evolved to be highly sophisticated and encompass several sub-systems such as modulation, signal detection, synchronization and coding.

This thesis contributes to our understanding of the WSWA channel and the design of several sub-systems for communications in WSWA channels. The key contributions are listed below.

1. Non-Gaussian ambient noise from snapping shrimp in warm shallow waters is identified as a key performance hurdle for communication systems. It is shown that the Symmetric α -Stable (S α S) distributions model the observed ambient noise accurately.
2. A theoretical framework for performance analysis of uncoded and coded communication systems in S α S noise is developed. The effect of S α S noise on antipodal communications is studied using this framework.
3. A computationally simple detector – the sign correlator – is shown to be near-optimal in the presence of S α S noise. Its performance with relation to the commonly used linear correlator and computationally intensive optimal detectors is studied.
4. To combat S α S noise, the adoption of a 1-norm metric in the Viterbi algorithm is proposed. The performance of the modified Viterbi algorithm is shown to be near-optimal in S α S noise.
5. A physics-based channel model is proposed for very shallow water channels. The model is calibrated and validated via comparison with experimental results. A simulation software has been developed to enable researchers to perform numerical experiments using the channel model.
6. Based on our improved understanding of the WSWA channel and signal processing in snapping shrimp noise, an orthogonal frequency division multiplexing (OFDM) based communication scheme is proposed for communications in the WSWA channels. The scheme was tested in

Singapore waters and was shown to demonstrate better performance as compared to the expected performance of commercial modems.

1.4. Thesis Organization

Chapter 2 presents a literature survey on shallow water ambient noise, underwater acoustic communications and OFDM communications in non-Gaussian noise. The results from tests of a commercial modem in Singapore waters are also presented to benchmark available commercial technology.

Chapter 3 introduces S α S random variables and presents their key properties. The snapping shrimp dominated ambient noise from Singapore waters is shown to be modeled accurately using S α S random process. Chapter 4 presents an analysis of the performance of signal detection in S α S noise. Near-optimal detectors are developed and studied in this chapter. Chapter 5 presents an analysis of coded and uncoded communication performance in the presence of S α S noise. The 1-norm metric based Viterbi algorithm is developed and studied in this chapter.

Chapter 6 presents a physics-based channel propagation model. The model is calibrated and validated against experimental results.

In light of the findings from Chapters 3-6, an OFDM based communication scheme is proposed in Chapter 7. The scheme was tested in simulation using the channel and noise models developed. The scheme was further tested via a set of field experiments in Singapore waters and shown to demonstrate good performance. The results from these experiments are presented in Chapter 8.

Chapter 9 summarizes the key findings from the research and outlines directions for further research.

2. Background

2.1. Brief History

The UWA channel is band-limited and reverberant. Until the late 1970's, communication systems had no means of mitigating the distortion introduced by such channels [8]. With the advent of digital communications and parallel developments in severely fading radio channels, some level of channel compensation and explicit error correction became possible. Since then UWA communications has seen a steady improvement in data rate and reliability. The initial improvements were based on incoherent modulation techniques such as frequency shift keying (FSK) due to their robustness. In the early 1980's it was believed that phase coherent modulation techniques would not work in UWA channels. However, interest in phase coherent systems due to their higher bandwidth efficiency led to a large number of publications in the 1990's. Powerful receiver algorithms coupled with decision feedback equalizers (DFE) and second-order phase-locked-loop (PLL) enabled phase coherent algorithms to achieve rates of up to 10 kbps in a medium range shallow UWA channel [9;10]. Later, data rates of 20 kbps have been reported in a very shallow UWA channel at Woods Hole harbor [11] while rates of nearly 15 kbps have been reported in the Baltic Sea [12].

2.2. Review of Research in UWA Communications

Several review papers on underwater acoustic communications have appeared in the literature [1;2;4;8]. These papers provide an excellent overview of advances in the field of underwater communications in the past decades. In this section, we review some of the key papers and ideas relevant to the research presented in this thesis.

2.2.1. Channel Propagation Modeling

A good understanding of the communications channel is important in the design of a communication system. It aids in the development of signal processing techniques as well as in the testing of the techniques via simulation. Ray theory and the theory of normal modes have provided the basis for such channel modeling [13]. At high frequencies, ray tracing is an appropriate model and is commonly used to determine the coarse multipath structure of the channel.

In [14], Essebbbar, Loubet and Vial have developed a ray tracing based channel simulator. They model the ocean as a layered medium with a constant sound velocity gradient in each layer. The simulator also takes into account the effects of the movement of the receiver on the channel. Apart from the movement of the receiver, the surface movement and environmental changes can contribute significantly to the variability of a channel. These have been modeled and measured in [15] and [16]. A simpler stochastic channel model has been presented in [17]. The model is validated against experimental results from a very shallow water channel in Southampton, UK.

In wireless communications, it is common to model a multipath channel using a tapped delay line with tap gains as stochastic processes [18]. When the tap gains are modeled using complex Gaussian processes, the resulting channel is the well known Rayleigh fading channel. Some researchers consider the shallow water medium range channel to exhibit Rayleigh fading [1]. Experimental support for such claims is found in [17] and [19]. However, the model has been challenged in [14] and [20].

A hybrid model where the multipath tap delays are computed using a ray model and the tap variation is modeled using Ricean statistics is proposed in [20]. The motivation for such a channel model is discussed in depth but no results or validation

is presented. Although the model is physics-based, the model does not include known acoustic propagation physics such as spreading, absorption, etc.

Currently there seems to be no consensus among researchers as to which channel model is best suited for very shallow water medium range channels.

2.2.2. Channel Noise Modeling

The natural soundscape in Singapore waters is dominated by shipping below 1 kHz. Reclamation noise contributes between 300 Hz and 3 kHz. Beyond about 2 kHz, the ambient noise is dominated by snapping shrimp [6;7]. Snapping shrimp noise is expected in all warm shallow waters, except with very high winds or precipitation. Most medium range communication systems are expected to operate at snapping shrimp dominated frequency bands.

Snapping shrimp are impulsive sources and the noise power distribution due to snapping shrimp is known to be approximately log-normal [7]. The pressure amplitude distribution is also known to be heavy tailed [5]. The noise amplitude distribution (pressure amplitude in case of acoustics) plays an important role in the analysis of communication schemes. A linear communication receiver designed with a Gaussian noise assumption is sub-optimal in the presence of non-Gaussian noise. With knowledge of the noise distribution, optimal or near-optimal non-linear receivers can be designed to outperform the linear receiver [21]. The development of such receivers is usually heuristic and is undertaken in communications only as a special case [22]. Such a development has not been undertaken for UWA channels with snapping shrimp noise.

2.2.3. Communication Techniques

As UWA propagation is predominantly linear, the frequency content of communication signals remains largely contained within its original frequency band.

The phase and amplitude of the signal can, however, vary widely. This observation led to the use of FSK as the incoherent method of choice for early UWA communication systems [8]. However, most incoherent communication systems yield relatively low data rates. Although it was believed in 1980s that coherent communication in UWA channels would not be possible, the 1990s saw the development of many coherent systems.

Phase-coherent UWA communications has evolved significantly in the past two decades. Based on the carrier synchronization method, coherent communications falls into two categories – differentially coherent (such as differential phase shift keying or DPSK) or purely coherent (such as phase shift keying or PSK). Although differentially coherent methods use a simpler synchronization technique, they incur a performance penalty as compared to purely coherent methods [18]. The use of PLL and DFE in UWA were key milestones that made coherent UWA communication possible [10]. A coherent communication scheme with joint channel synchronization and equalization was presented and experimentally tested in [10]. A high-rate QPSK communication scheme with adaptive equalization was presented in [11]. In this paper, the authors showed that a high-rate system performed better in a medium-range shallow water channel due to enhanced tracking of the channel by the equalizer as a result of more frequent sampling of the channel.

Spread spectrum systems provide robust communication in many frequency-selective fading environments. As the UWA channel exhibits frequency-selective fading, one would expect that spread spectrum communications may perform well in such a channel. The performances of frequency-hopping spread-spectrum (FHSS) and direct-sequence spread-spectrum (DSSS) were studied in [23]. The authors found that both FHSS and DSSS performed well in two experimental scenarios. The DSSS raw

performance was better than that of FHSS. However, the simplicity of FHSS and its intrinsic near-far resistance make it attractive in some circumstances. Although spread spectrum systems provide robust performance, they are not bandwidth efficient except in the case of multi-user systems [24]. In bandwidth limited UWA channels, the low bandwidth efficiency of spread spectrum systems is a key drawback.

The concept of using parallel data transmission by means of frequency division multiplexing (FDM) was published in the 1950s and 1960s. In 1971, the discrete Fourier transform (DFT) was identified as a convenient way to achieve FDM [25]. This led to the development of efficient OFDM systems in the 1980s and 1990s. The use of OFDM with a cyclic prefix simplifies the receiver structure in a frequency-selective channel as each sub-carrier only experiences flat fading [26]. Additionally, robust performance can be achieved by introducing redundancy across carriers through the use of coding. UWA communication schemes based on coded OFDM were studied theoretically in a series of papers [27-30]. The authors, however, did not publish experimental results based on any of these schemes. Coatelan and Glavieux [31] designed and tested a low-speed OFDM communication scheme in cold shallow waters. Bejjani and Belfiore [32] studied a multi-carrier QAM/QPSK UWA communication scheme. They modeled the UWA channel as a Rician or Rayleigh fading channel for simulation, but did not present any experimental results. Kim and Lu [33] studied the effect of frequency and time selectivity on OFDM underwater communications via simulation and concluded that a robust scheme could be developed. Zhakharov and Kodanev [34] demonstrated a low-frequency long-range OFDM communication link the Baltic sea by exploiting the multipath Doppler diversity in the channel. Yeung et al. [35;36] demonstrated a high-speed multi-carrier communication link in very shallow coastal waters near Hong Kong. More recently,

Frassati et al. [37] successfully demonstrated low-speed long-range OFDM communication in the Mediterranean sea.

OFDM has been used in many telecommunication systems, especially to combat impulsive noise [38-40]. As warm shallow waters have impulsive ambient noise, OFDM may be suitable for UWA applications. However, this property of OFDM has not been exploited by researchers in UWA communications.

Time reversal mirroring (TRM) has been implemented in the laboratory and in the ocean [41;42]. Such mirrors utilize the time-symmetry in the wave equation to refocus energy back at a source despite the complexity of the channel by effectively using the ocean as an analog computer. This naturally leads to the idea of communication using TRM [43]. TRM requires that the acoustic propagation through the ocean does not vary significantly over the communication period. Long coherence times have been demonstrated at low-to-mid frequencies in shallow and deep waters. However, one would expect that small variations in the environment (such as wave action on the surface) would become significant at high frequencies. This would lead to very short coherence times, making the use of TRM for high-frequency communication impractical. TRM is often implemented using a large array of transducers. Although it may be possible to implement TRM with a single transducer, the gain from TRM in such a setup is expected to be very small. Hence we do not consider TRM as a serious candidate for a high-frequency single transducer UWA communication system.

More recent research in UWA communications has focused on multiple input multiple output (MIMO) systems, space-time coding and spatial diversity processing [9;44;45]. As all of these techniques utilize arrays at the transmitter and/or receiver, they are not of direct relevance to the work presented in this thesis.

2.3. Signal Processing in Impulsive Noise

As mentioned in the previous section, the ambient noise in Singapore waters is impulsive. Several signal processing and communication techniques have been developed for impulsive noise channels. We review some of the key noise models and signal processing techniques.

2.3.1. Impulsive Noise Models

The Middleton Class A and Class B noise models represent impulsive noise in a variety of environments [46;47]. The Class A model is applicable when the noise bandwidth is small or comparable to the receiver bandwidth. The Class B model is used if the receiver bandwidth is small as compared to the noise bandwidth. The model consists of a Gaussian noise component and an impulsive noise component. The impulsive component is governed by a Poisson process and impulse duration. The Johnson S_u noise model, a parametric family of densities with heavy tails, has been used to represent underwater acoustic noise from biological sources [48]. The Laplacian density has been used to model a number of noise environments, including underwater acoustic channels [49]. Other densities such as the Gaussian mixture densities have also been used to model impulsive noise environments. However, none of these noise models have a strong physical or theoretical justification for use in the description of ambient noise in warm shallow waters.

The family of *stable* distributions provide a useful theoretical tool for impulsive noise environments [50]. These distributions are a direct generalization of the Gaussian distribution and include the Gaussian as a limiting case. The stable family of distributions arises out of a *generalized Central Limit Theorem* which states that the sum of independent and identically distributed random variables with or without a finite variance converges to a stable distribution by increasing the number of variables

[51]. The S α S noise model arises as a special case of stable noise, if the positive and negative noise amplitudes are equally likely. The S α S noise model describes the ambient noise in warm shallow waters accurately, as we shall show in Chapter 3.

2.3.2. Signal Detection in Impulsive Noise

The problem of detecting a known signal with unknown amplitude in noise is commonly encountered in areas such as communications, target detection, ranging and environmental sensing. If the noise statistics are known, an optimal detector can be designed based on the maximum-likelihood (ML) criterion. When the noise is Gaussian and white, the ML detector is the linear correlator (LC) [21]. Unlike a general ML detector, the LC does not require knowledge of the parameters of the underlying probability distribution. In the presence of non-Gaussian noise, the LC is no longer optimal. In spite of this, many signal processing algorithms still use the LC for signal detection in non-Gaussian noise due to its simple implementation and the lack of detailed statistical information about the noise.

Since the LC is not optimal in snapping shrimp dominated ambient noise, a significant potential exists for enhancing the detection performance of signal processing algorithms in these waters. Nielsen and Thomas [52] explored the use of non-parametric detectors in snapping shrimp noise but concluded that the LC performed better than non-parametric techniques. This conclusion is not in agreement with the results obtained during our research (presented in Section 4.1). More recently, Bertilone and Killeen [53] modeled snapping shrimp noise using a Gaussian-Gaussian mixture but concluded that there were some inconsistencies. They found that locally optimal (LO) detectors performed better than the LC at low signal-to-noise ratio (SNR) but failed at high SNR.

Nikias and Shao [50] explored the development of optimal detectors in presence of S α S noise. They showed that a globally optimal (commonly known as *uniformly most powerful* or UMP) receiver does not exist in the general S α S noise case. However, LO detectors can be designed for detection of weak signals by introducing a non-linear transfer function before a standard LC detector. These detectors perform better than LC detectors in detecting weak signals in the presence of S α S noise. However, they require detailed parametric knowledge of the noise distribution in order to design the non-linear transfer function.

2.3.3. Communication in Impulsive Noise

Soon after Middleton proposed his impulse noise models, Spaulding and Middleton [54;55] published a series of papers on optimum reception in impulsive noise. They developed detection algorithms for optimal detection in Middleton Class A noise and showed that a substantial saving in power could be achieved with these algorithms. Although the optimal algorithms were computationally impractical, they showed that a locally optimal algorithm with lower complexity could be developed.

Tsihrintzis and Nikias [21;56] studied the performance of various coherent and incoherent receivers in the presence S α S noise. They showed that the linear receiver performed poorly in the presence of S α S noise. On the other hand, a Cauchy receiver exhibited relatively robust performance.

As coded OFDM has been used in telecommunication systems to combat impulse noise, several publications on OFDM communications in impulse noise are available (e.g. [38-40]). However, none of the publications develop optimal coded OFDM receivers or analyze the performance of coded OFDM in the presence of S α S noise.

2.4. Practical Considerations

Shannon showed that the channel capacity is a function of bandwidth and SNR [57]. If the communication is not inter-symbol-interference (ISI) -limited, SNR can be improved by increasing transmission power. Thus data rates can be increased by increasing signal bandwidth or power. In case of ISI-limited communication, increasing the transmission power increases the power of the ISI and thus does not improve communication performance. Communication channels are often classified as band-limited or power-limited based on the primary constraint limiting the data rate. The UWA channel is both power- and band-limited, thus imposing an upper bound on achievable data rates.

2.4.1. Bandwidth Limitations

The available communication bandwidth is determined by the upper and lower limits of the frequency band. The band is theoretically limited on the lower side at 0 Hz, but practically limited by transducer characteristics and increased ambient noise [58]. Ambient noise levels in Singapore waters can be as high as 70-90 dB re^{*} 1 μ Pa²/Hz at 1 kHz, reducing to 50-70 dB re 1 μ Pa²/Hz by 100 kHz [7]. Additionally, low frequency transducers are physically larger and require more power. Transmissions at higher frequencies are typically limited by sound attenuation due to relaxation of MgSO₄ in sea water and viscous absorption [59]. Attenuation increases rapidly with frequency (Figure 2.1); in warm shallow waters, it is about 0.4 dB/km at 10 kHz and increases to >30 dB/km by 100 kHz.

The frequency band for communication should be chosen based on local ambient noise conditions, acceptable SNR, transmission range, available power,

^{*} with reference to

electronics and transducers. For a typical 1 to 2 km transmission range, this results in a bandwidth availability of about 50 to 70 kHz.

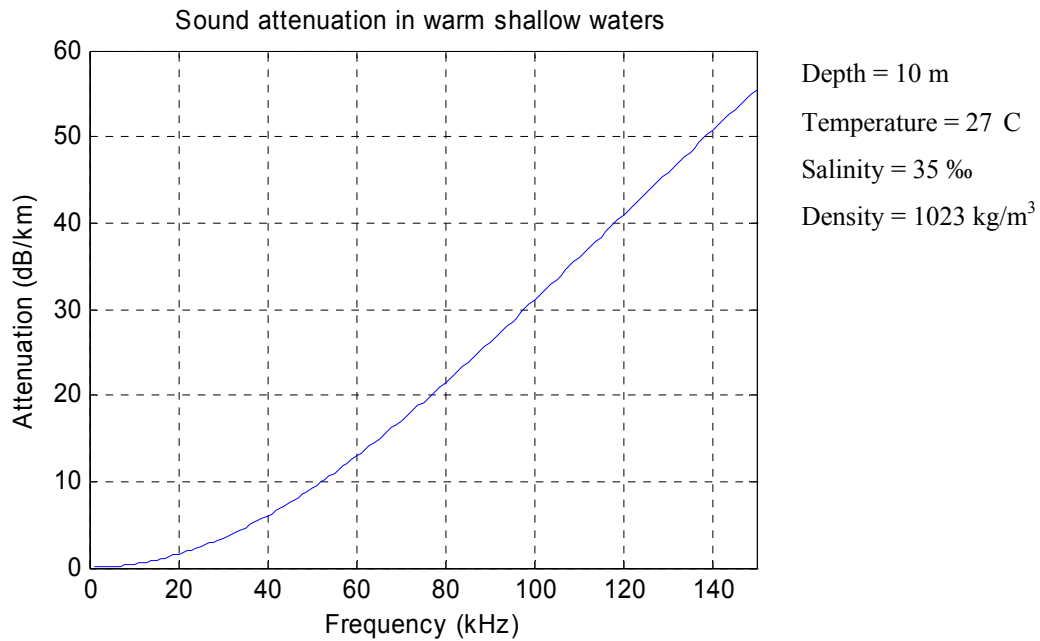


Figure 2.1. Attenuation of sound in shallow warm sea water

2.4.2. Transmission Power Limitations

Transmission power is typically limited by electrical power availability considerations (such as battery life), electronics, transducers and cavitation limitations. Cavitation is the process in which vapor pockets are formed in the liquid medium due to very low instantaneous pressure as a result of a strong sound source. Cavitation reduces transmission efficiency, causes damage to transducer surface and introduces undesirable non-linear effects. The cavitation threshold depends on the size of the transducer producing the sound, depth of the transducer, frequency, pulse length and properties of sea water [58]. In very shallow waters, typical high frequency transducers can produce source levels of up to about 210 dB re 1μPa at 1m without significant danger of cavitation. Higher source levels may be produced if needed by careful design of transmitters. However, higher source levels increase the risk of biological damage and have safety and environmental implications. Practical

considerations on electronics and battery life limit communication systems to work at lower power levels of about 185 to 195 dB re 1 μ Pa at 1m.

2.5. Performance of Modems in Singapore Waters

Although data rates of up to 20 kbps have been reported for horizontal transmissions in shallow waters, these data rates do not seem to be representative of the communication data rates in Singapore waters. Based on discussions with leading commercial UWA modem vendors, most vendors do not expect to get more than about 1 kbps in medium range WSWA channels*. Although the Evologics modem (based on technology published in [12]) claims to work at up to 33 kbps[†], the modems failed to establish a link during a test in Singapore waters at distances greater than 100 m[‡]. The experimental setup and results are presented in the following sections.

The lower performance of the modems in Singapore waters may be explained if the WSWA channel exhibits more time-variability as compared with the Baltic Sea. Comparative time-variability measurements are currently not available to verify this. Ambient noise in Singapore waters is known to be dominated by heavy shipping and snapping shrimp and consequently non-Gaussian in power distribution [6;7]. We believe that this may be a significant factor in the observed poor performance of commercial modems in these waters. In Chapters 3, 4 and 5, we demonstrate that

* The rates quoted are based on personal discussions with prominent modem vendors, LinkQuest and Benthos, during MTS/IEEE Oceans 2003 conference in San Diego. These rates are in agreement with modem specifications available at <http://www.link-quest.com/html/models1.htm> (as of November 2, 2005) for modems UWM2000H and UWM3000H.

[†] See <http://www.evologics.de/documents/S2C%20180%20modem.pdf> (as of November 2, 2005).

[‡] The experimental results have been documented in a technical report submitted to Defence Science & Technology Agency (DSTA) in February 2004 – “TDP Ocean Acoustic Research Works D11: Trial / experimentation report on testing of acoustic modems and communication technology in Singapore shallow waters (version 1.1)”.

Gaussian noise based signal processing techniques degrade rapidly in the presence of snapping shrimp noise.

2.5.1. Modems tested in Singapore Waters

To build an understanding of performance limitations in Singapore waters, the ARL* invited several modem manufacturers for performance tests in early 2004. LinkQuest, Benthos and Evologics, three key players in the underwater acoustic modem market, were invited. Although all three parties initially expressed interest in the tests, Benthos later did not wish to participate. They orally indicated that they did not expect their modems to perform reliably with more than a few hundred bps in the noise and multi-path conditions expected in Singapore waters. Informal tests with the short-range LinkQuest modems (UWM1000 series) showed that they often failed to establish communication links in Singapore waters beyond about 50 to 100 m. LinkQuest believed that their newer longer-range modems (UWM3000 series) would perform much better in Singapore waters and recommended the use of those for the tests. The published data rates for the UWM3000 series modems are in the range of 80 to 320 bps. As the expected data rate of the modem is quite low and the rental costs quite high, LinkQuest modems were eventually not included in these tests. Evologics is a spin-off company from the technical university at Berlin. They have developed acoustic communication technology, which has performed well (approximately 33 kbps) over medium range (1.7 km) in shallow-water conditions in the Baltic Sea. Evologics was confident that their S2C modem would be able to achieve high data rates (several tens of kbps) in Singapore waters, and kindly agreed to come to Singapore in February 2004 to test the modems.

* Acoustic Research Laboratory (ARL), Tropical Marine Science Institute (TMSI), National University of Singapore (NUS) – <http://www.arl.nus.edu.sg>

The key technology used by the S2C modem is a sweep spread-spectrum communication scheme [12;60]. The communication is implemented over a linear frequency-sweep carrier. The advantage of such a carrier is in the separation of multi-path arrivals. Applying a transform to the received signal, the linear sweep can be rotated in time-frequency space such that the multi-path arrivals are separated in frequency rather than in time. The strongest multi-path arrival can then be selected via a band-pass filter and then decoded to recover the transmitted data. The modem uses a frequency band between 40 kHz and 80 kHz (6 dB points) with a source level of about 194 dB re $1\mu\text{Pa}^2$ with a peak power consumption of 400 W.

2.5.2. Experimental Setup

The sea trial was performed at Selat Pauh ($1^\circ 13.39'$ N $103^\circ 44.59'$ E) in coastal Singapore waters. The water depth at the barge was approximately 15 m, with a relatively flat bathymetry over the experimental site. The S2C modems were mounted at the bottom of a 4 m pole. The setup is shown in Figure 2.2. One modem was mounted on the side of a barge while the other modem was mounted from the bow of a boat. The boat moved to various distances from the barge and made transmissions. The S2C modems have directivity with a beam-width of about 60° , and had to be continuously aligned in order to test with optimal signal strength.

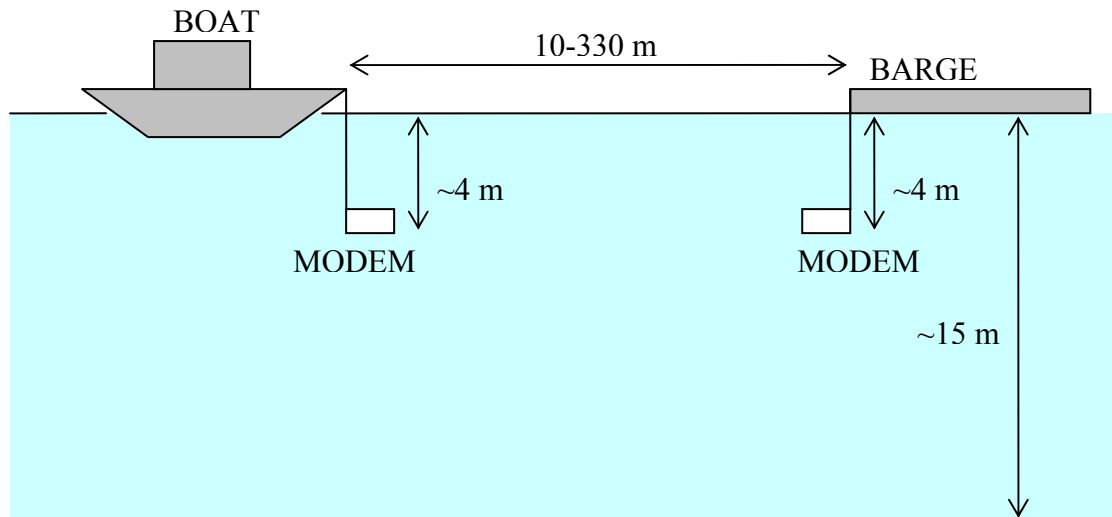


Figure 2.2. Sea trial setup for Evologics S2C modem (side view)

The experiment consisted of sending files of varying sizes over a connection established between the two modems. The file sizes sent were varied depending on the quality of the connection. Modem parameters that affected performance were tuned before each quoted measurement was made. The success of transfer, raw data rate and effective data rate were recorded. The raw data rate is the data rate of the raw data transmitted, and does not take into account the overheads of forward error correction, packet headers, delay between packets and retransmissions. The effective data rate was computed based on the file size and the time taken to transfer the file.

2.5.3. Experimental Results

During the trials, the S2C modems managed to establish connection up to a distance of 330 m. The results of each transmission tests are shown below. The transmissions worked up to about 100 m, beyond which they consistently failed to establish a link. Many transmission failures occurred within a 100 m range as well. The transmission rates achieved were about 6 kbps at 10 m range, steadily reducing to about 1 kbps at 90 m range.

Table 2.1. Sea trial results for the Evologics S2C modem

Range (m)	Connection Status	File Size (bytes)	Elapsed Time (s)	Raw Rate (bps)	Effective Rate (bps)
10	Online	9,372	12.33	33,333	6,081
30	Online	18,955	83.00	12,500	1,827
40	Online	1,028	24.00	10,400	343
40	Online	3,072	8.00	15,000	3,072
40	Online	1,028	7.50	15,384	1,096
70	Online	1,028	43.00	9,600	191
70	Online	1,541	73.00	3,610	169
90	Online	2,936	26.53	7,462	885
90	Online	2,936	22.80	5,780	1,030
90	Online	1,541	29.71	6,410	415
90	Online	2,936	29.78	7,200	789
130	Online	1,024	Very long	-	-
130	Online	56	Short	-	-
330	Online	Unable to transmit, intermittent connection failure			

The S2C modems did not achieve the expected performance of several tens of kbps up to 1 km. The same modems achieved data rates of 33 kbps up to 1.7 km in the Baltic Sea. This shows that the environmental conditions in Singapore waters are significantly different than those in many other shallow water areas; the measurements in other areas should not be used as a benchmark of performance for Singapore waters.

2.6. Conclusions

In this chapter, we briefly reviewed UWA channel models, ambient noise models and communication techniques. Although several channel models have been developed, there is no consensus among researchers on a suitable model for medium-range very shallow water channels. Researchers have been using a Gaussian noise

model for analysis of communication systems. This model is violated substantially and consistently in Singapore waters. Coherent PSK with PLL and DFE are the primary communication techniques for single-transducer UWA communications today. Spread spectrum communications are also often used to add robustness at the cost of reduced data rates due to lower bandwidth efficiency.

We also reviewed several impulsive noise models and optimal or near-optimal detectors and receivers. Most detectors/receivers are based critically on the noise model and hence sensitive to the noise parameters. The Cauchy receiver is among one of few receivers which demonstrates robust behavior in S α S noise. Coded OFDM is known for its robustness to impulse noise. However, no theoretical framework for analysis of performance of coded OFDM in S α S impulse noise exists.

We outlined the practical limitations on a medium-range UWA communication system in terms of bandwidth and power constraints. Finally, we presented the results from an experiment where a commercial modem was tested in Singapore waters. Although the modem demonstrated excellent shallow water performance in the Baltic Sea, its performance in Singapore water was very poor. We believe that this poor performance was primarily due to differences such as non-Gaussian noise between WSWA channels and other shallow water channels.

3. Ambient Noise Model

As one of the key differences between the WSWA channel and other channels is the ambient noise structure, we seek to understand the characteristics of ambient noise found in warm shallow waters around Singapore.

3.1. Power Spectrum

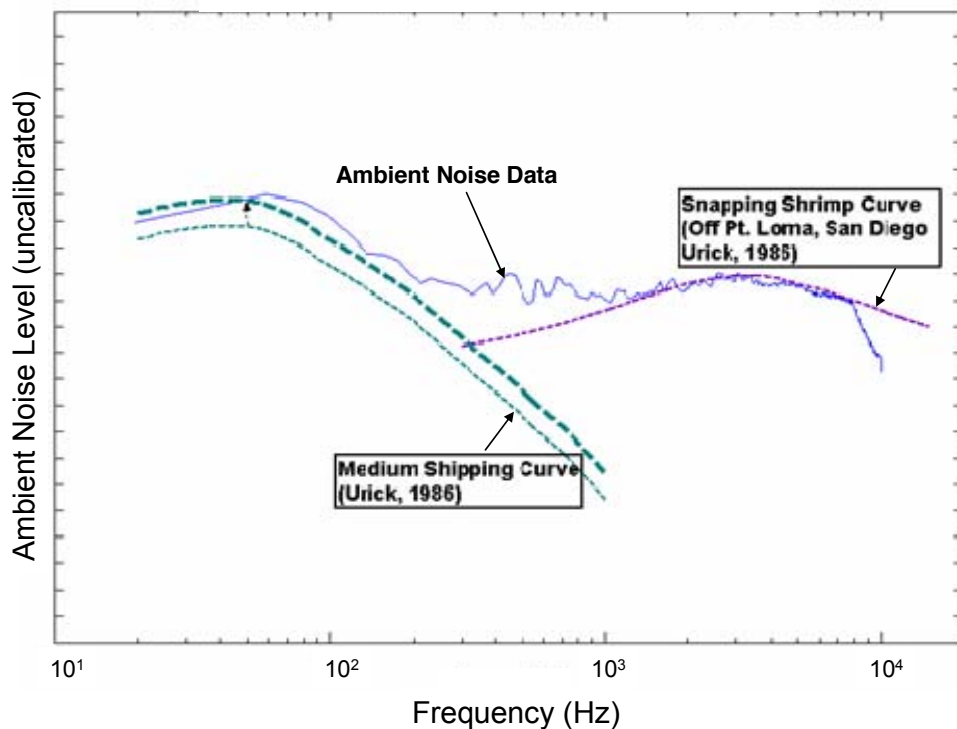


Figure 3.1. Ambient noise PSD for a coral reef site

The ambient noise is believed to be dominated by shipping below 1 kHz and snapping shrimp above 2 kHz [6]. Reclamation noise contributes between 300 Hz and 3 kHz. Figure 3.1 and Figure 3.2* show sample Power Spectral Density (PSD) of ambient noise from sites in Singapore waters [61] as compared to documented curves

* Both figures are reproduced here from [61] for ease of reference. The y-axis in both figures is marked as uncalibrated due to confidentiality requirements imposed by the funding agency of the data collection project.

[62]. At the coral reef site, the medium shipping curve had to be shifted up slightly to fit the data. At the shipping anchorage and channel site, the heavy shipping curve had to be significantly shifted up. This can be explained by the fact that Singapore is a busy port. In both cases, the snapping shrimp curve fit the data at higher frequencies very well. It is evident from the curves that while low frequency ambient noise is dominated by shipping, the high frequency ambient noise is dominated by snapping shrimp.

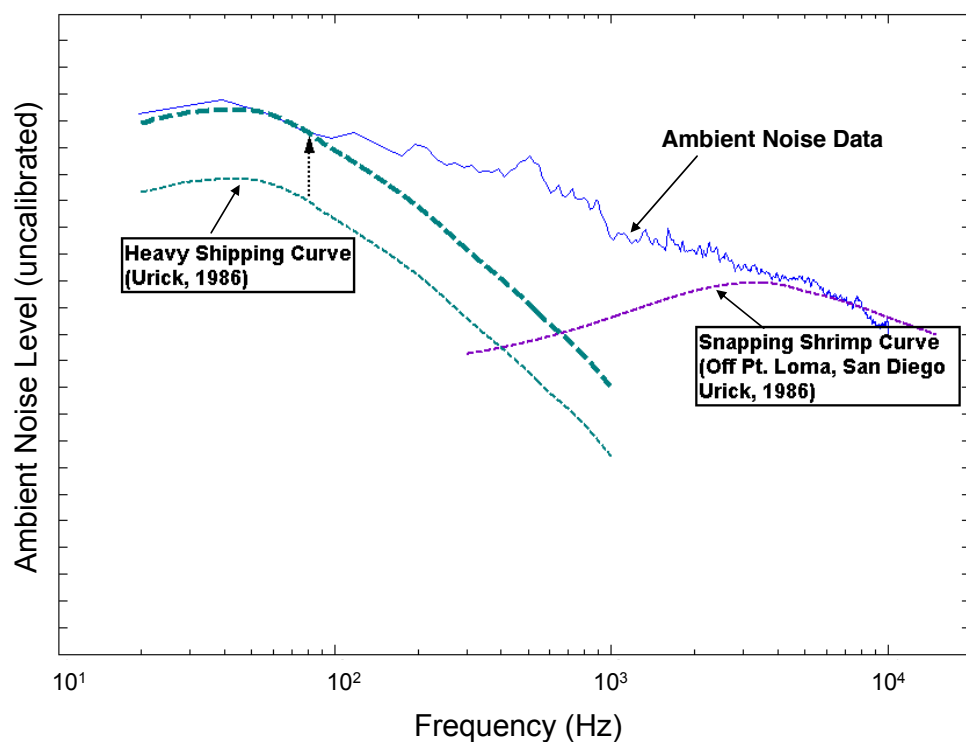


Figure 3.2. Ambient noise PSD for a shipping anchorage and channel

As the attenuation of sound in the ocean is a frequency-dependent process, the ocean acts as a low-pass filter for ambient noise. The ambient noise PSD is thus usually “pink” i.e. the noise has more power at lower frequencies and less power at higher frequencies.

3.2. Probability Distribution

Snapping shrimp noise is expected to dominate high frequency ambient noise in all warm shallow waters, except with very high winds or precipitation. Snapping shrimp are highly impulsive noise sources. Although each shrimp produces a distinct “snap”, the observed ambient noise is composed of a large number of overlapping snaps from many colonies of shrimp [63] and the reflected sounds from the sea surface and bottom [64]. The noise power distribution due to the snapping shrimp is known to be approximately log-normal [7]. The noise pressure amplitude distribution is of more interest in communication studies than the noise power distribution. As we shall see, the ambient noise pressure amplitude distribution is also highly non-Gaussian.

Gaussian distributed data appear linear on a normal probability plot, while deviation from linearity indicates non-Gaussian data. A representative normal probability plot [65] of the noise pressure amplitude is shown in Figure 3.3. The plot shows a non-Gaussian distribution with heavy tails. A plot of the empirical probability density function (PDF) of the noise sample against the best Gaussian fit^{*} (Figure 3.4) shows that Gaussian PDF is a poor approximation of the observed PDF. The trimmed[†] Gaussian fitting yields a better fit, but is still quite poor. The improvement in fit is expected as trimming removes part of the heavy tails of the observed distribution and hence the fit in the central part of the distribution is better.

^{*} The best Gaussian fit was computed using the MATLAB normfit function, which estimates the fit by computing the sample mean and sample standard deviation.

[†] The trimming was performed by removing all samples more than 3 sample standard deviations away from the mean.

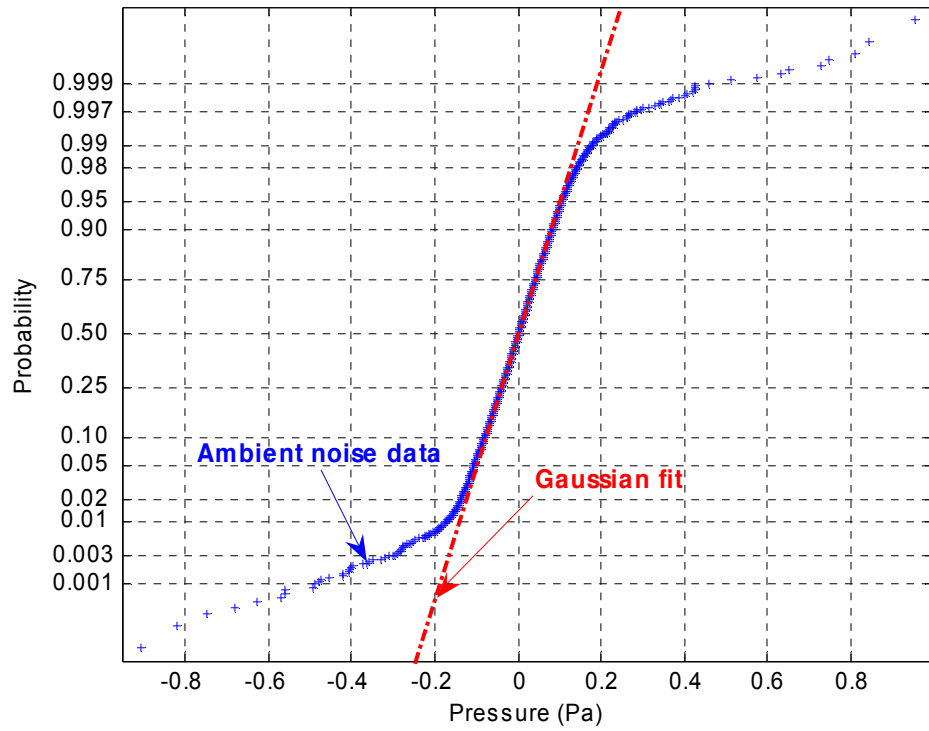


Figure 3.3. Normal probability plot of acoustic pressure of ambient noise

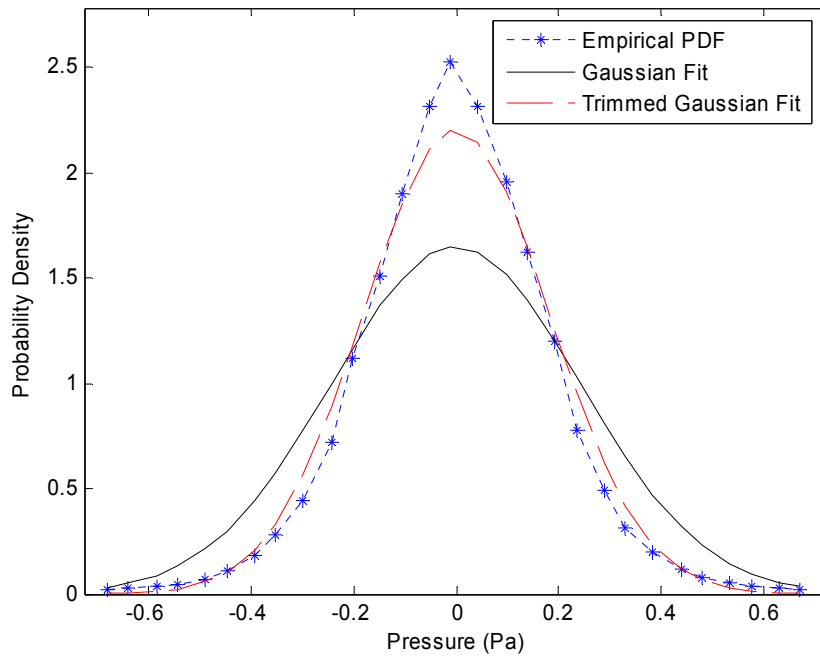


Figure 3.4. Best Gaussian fit for probability density of ambient noise

Several well-known PDFs were unsuccessfully tested for fit to the measured data. Gaussian mixture, generalized Gaussian and Gaussian double exponential

distributions have been reported to fit some non-Gaussian data well [66]. However, none of these PDFs were found to approximate the observed data accurately.

3.3. The S α S Noise Model

Impulsive noise tends to produce large-amplitude excursions from the average more frequently than Gaussian signals. The PDF for such noise decays less rapidly than the Gaussian PDF. It is for such signals that the *stable* distributions provide a useful theoretical tool [50]. Stable distributions are a direct generalization of the Gaussian distribution and include the Gaussian as a limiting case. A parameter, known as the *characteristic exponent* $(\alpha)^*$, of the distribution controls the heaviness of its tails. A small positive value for α represents highly impulsive distributions while α close to 2 indicates Gaussian-like behavior. When $\alpha = 2$, the distribution reduces to a Gaussian distribution. The stable family of distributions arises out of a *generalized Central Limit Theorem* which states that the sum of independent and identically distributed random variables with or without a finite variance converges to a stable distribution by increasing the number of variables [51]. The defining feature of stable distributions is the *stability property*, which states that the sum of two independent stable random variables with the same characteristic exponent is stable with the same characteristic exponent [50].

The stable distribution can be most conveniently described by its characteristic function [50]:

$$\varphi(t) = \exp[j\alpha t - \gamma |t|^\alpha \{1 + j\beta \operatorname{sgn}(t)\omega(t, \alpha)\}] \quad (3.1)$$

where $j = \sqrt{-1}$ and

* The characteristic exponent is represented by the symbol α such that $0 < \alpha \leq 2$. The distribution derives its name from this parameter, and therefore is often called the α -stable distribution.

$$\omega(t, \alpha) = \begin{cases} \tan \frac{\alpha\pi}{2}, & \text{if } \alpha \neq 1 \\ \frac{2}{\pi} \log |t|, & \text{if } \alpha = 1. \end{cases}$$

In the above expression, α is the characteristic exponent controlling the heaviness of the tails, β is a symmetry parameter, γ is a scale parameter and a is the location parameter. The scale parameter (γ), also known as *dispersion*, determines the spread of the distribution in a similar way as the variance in a Gaussian distribution. When $\alpha = 2$, γ equals half the variance. For all other values of α , the variance of the stable distribution is infinite. A related parameter often used with stable distributions is the scale parameter (defined as $\gamma^{1/\alpha}$), which plays the same role as standard deviation in the case of Gaussian random variables. The location parameter (a) is the mean of the distribution when $\alpha > 1$ and median of the distribution otherwise. The mean of stable distributions with $\alpha \leq 1$ is infinite.

The inverse Fourier transform of the characteristic function gives us the PDF. Unfortunately, no closed-form expressions exist for the general stable density and distribution functions, except for the Gaussian ($\alpha = 2$), Cauchy ($\alpha = 1$, $\beta = 0$) and Pearson ($\alpha = 1/2$, $\beta = -1$) cases [50]. An important subclass of the α -stable distributions, known as the symmetric α -stable (S α S) distribution, is characterized by $\beta = 0$ and $a = 0$. Efficient numerical methods exist for computing the PDF of S α S distributions [67].

For modeling of ambient noise in the ocean, S α S distributions seem to be ideally suited due to their impulsive behavior. The mean noise pressure must be zero by definition; hence the location parameter for the distribution must be zero. Other parameters of the distribution need to be estimated. Several estimators for parameters of S α S have been developed [50]. Of these, fractile based estimators are easy to use

and are known to work well. To estimate parameters of ambient noise, we use a fractile estimator for α developed by McCulloch [68] and a fractile estimator for c developed by Fama and Roll [69]. After estimating the parameters for a noise realization, the empirical PDF of the data is compared against the estimated S α S fit ($\alpha = 1.563$, $c = 0.1178$ Pa) in Figure 3.5. It is clear that the fit is much better than the Gaussian fit shown in Figure 3.4.

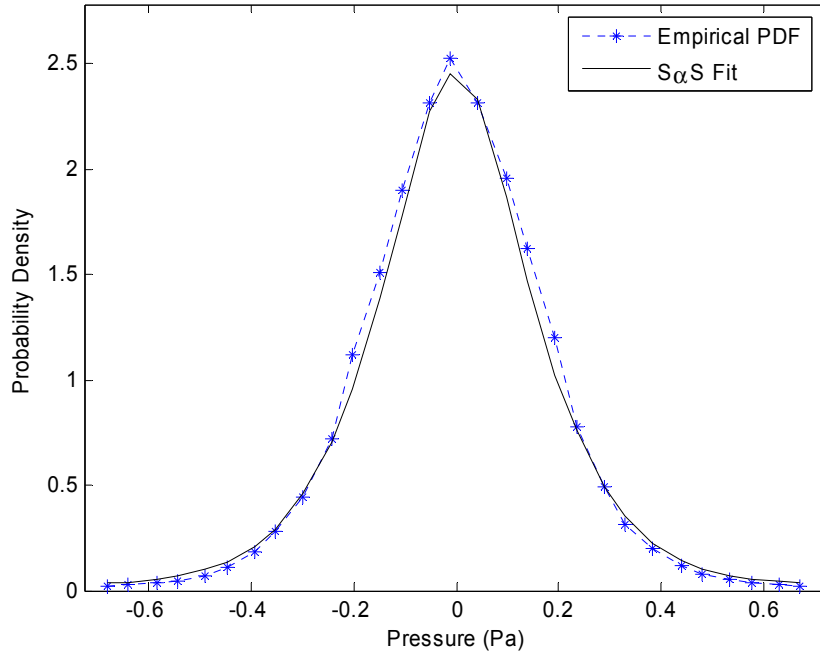


Figure 3.5. Best S α S fit for probability density of ambient noise

A plot of PDF on a linear scale does not show detailed behavior of the tails of the distribution. As the difference between the Gaussian distribution and the S α S distribution is primarily in the tails, it is useful to study the amplitude probability (double-sided tail probability) plots of the distribution. These plots show the probability of the noise exceeding a given amplitude on a logarithmic scale. Differences in tail behavior can be seen more clearly on such plots. Figure 3.6 shows the best Gaussian and S α S fit for ambient noise data collected from a location in

Singapore waters. It is clearly seen that the S α S distribution provides a much better fit for the ambient noise than the Gaussian distribution.

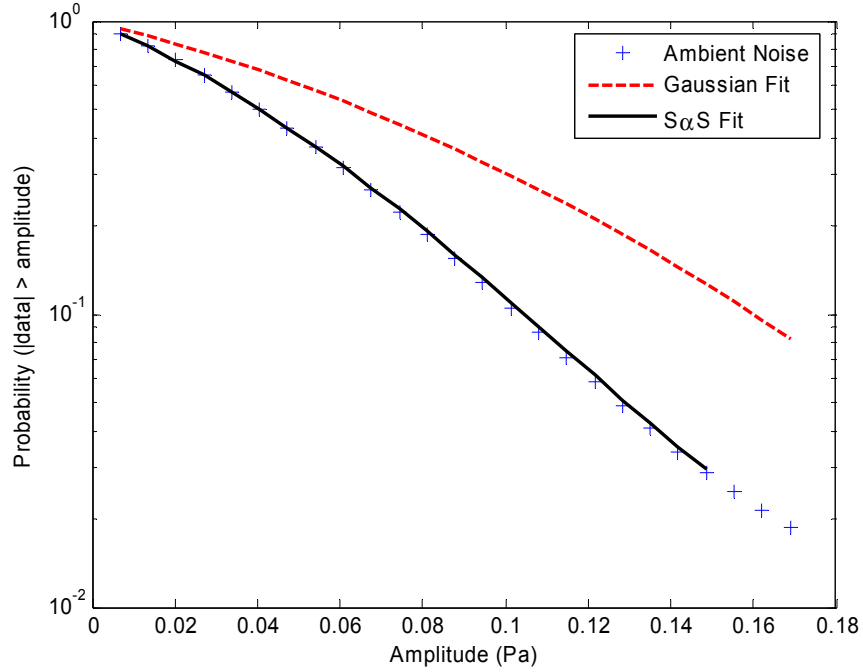


Figure 3.6. Amplitude probability plot of snapping shrimp dominated ambient noise showing that the probability distribution can be well approximated using a S α S distribution

To ensure that the S α S distributions are indeed good approximations of real ambient noise data, several samples of ambient noise collected at various times from different parts of Singapore waters were tested. All the samples yielded PDFs which could be approximated well by the S α S PDF with appropriate parameters. The values of α obtained were in the range of 1.5 to 1.9.

The Chi-square test [70] and the Kolmogorov-Smirnov test [71] were applied to 10,000 samples randomly chosen from the sample data sets to test the goodness of fit of the specified probability distribution to the data. The hypothesis that the data was obtained from a Gaussian distribution was rejected for sample data sets at a 1% level of significance in both tests. The hypothesis that the data was obtained from an S α S

distribution could not be rejected for sample data sets at a 1% level of significance in both tests.

3.4. Properties of the S α S Random Variables

As univariate S α S random variables and complex isotropic S α S random variables are extensively used to model noise in this thesis, we list down some of the important properties of these distributions. These properties and their proofs are given in [50;72].

Theorem 1: Stability Property

A random variable X has a stable distribution if and only if for all X_1 and X_2 which are independent random variables with the same distribution as X , and for arbitrary constants k_1 and k_2 , there exists a constant k , such that

$$k_1 X_1 + k_2 X_2 \stackrel{d}{=} kX \quad (3.2)$$

with

$$k_1^\alpha + k_2^\alpha = k^\alpha$$

where α is the characteristic exponent of X . The symbol $\stackrel{d}{=}$ denotes equivalence in probability distribution.

Theorem 2: Generalized Central Limit Theorem

The random variable X is the limit in distribution of normalized sums of the form

$$S_n = (X_1 + X_2 + \dots + X_n)/a_n - b_n \quad (3.3)$$

where X_1, X_2, \dots, X_n , are identical and independently distributed (i.i.d.) and $n \rightarrow \infty$, if and only if the distribution of X is stable.

In particular, if X_i have finite variance, the limit distribution is Gaussian, in line with the ordinary central limit theorem. However, when X_i have infinite variance, the limit distribution is stable. Additionally, if X_i have zero-mean symmetric distribution, the limit distribution is SoS provided $b_n = 0$.

Theorem 3: Existence of Moments

Let X be a SoS random variable with characteristic exponent α . The p -order moment of X can be expressed as $E|X|^p$. If $\alpha < 2$,

$$\begin{aligned} E|X|^p &< \infty \quad \text{if} \quad 0 \leq p < \alpha \\ E|X|^p &= \infty \quad \text{if} \quad p \geq \alpha. \end{aligned} \tag{3.4}$$

When $\alpha = 2$,

$$E|X|^p < \infty \quad \forall p. \tag{3.5}$$

When $\alpha < 1$, the SoS distribution has no finite first- or higher-order moments. For $1 < \alpha < 2$, the SoS distribution has a finite first-order moment and fractional low-order moments (FLOM) but an infinite variance and higher-order moments. When $\alpha = 2$, all moments exist.

Theorem 4: Fractional Low-Order (and Negative-Order) Moments

Let X be a SoS random variable with characteristic exponent α and dispersion γ .

For $-1 < p < \alpha$,

$$E|X|^p = C_{p\alpha} \gamma^{p/\alpha} \tag{3.6}$$

where

$$C_{p\alpha} = \frac{2^{p+1} \Gamma\left(\frac{p+1}{2}\right) \Gamma\left(-\frac{p}{\alpha}\right)}{\alpha \sqrt{\pi} \Gamma\left(-\frac{p}{2}\right)}.$$

Here, $C_{p\alpha}$ depends only on p and α and not on X , and $\Gamma(\dots)$ denotes the Gamma function [73].

Theorem 5: Closed-form Distributions

The S α S distribution does not have a general closed-form PDF. However, in the special cases of $\alpha = 1$ and $\alpha = 2$, the S α S distribution reduces to Cauchy and Gaussian distributions respectively. For $\alpha = 1$ and $\alpha = 2$, the PDF $f_\alpha(x; \gamma)$ can be expressed in closed-form as

$$f_1(x; \gamma) = \frac{\gamma}{\pi(x^2 + \gamma^2)} \quad (3.7)$$

and

$$f_2(x; \gamma) = \frac{1}{2\sqrt{\pi\gamma}} \exp\left(-\frac{x^2}{4\gamma}\right). \quad (3.8)$$

The S α S distribution does not have a general closed-form cumulative distribution function (CDF), $F_\alpha(x; \gamma)$. In the special case of the Cauchy distribution ($\alpha = 1$), a closed-form CDF exists as

$$F_1(x; \gamma) = \frac{1}{2} + \frac{1}{\pi} \arctan\left(\frac{x}{\gamma}\right). \quad (3.9)$$

Theorem 6: Asymptotic Tail Probability

Let X be a S α S random variable with characteristic exponent α ($0 < \alpha < 2$) and unit dispersion. The asymptotic behavior of the tail probability* of X is algebraic:

$$\lim_{x \rightarrow \infty} [1 - F_1(x; 1)] = \frac{C_\alpha}{2} x^{-\alpha} \quad (3.10)$$

where

* Throughout this thesis, we use the term *tail probability* to mean *right tail probability*

$$C_\alpha = \frac{1-\alpha}{\Gamma(2-\alpha)\cos\left(\frac{\pi\alpha}{2}\right)}.$$

Theorem 7: Complex Isotropic S α S Random Variables

A complex S α S random variable $X = X_1 + jX_2$ is isotropic (or rotationally invariant) if X_1 and X_2 are S α S random variables and

$$e^{j\phi} X \stackrel{d}{=} X \quad \forall \quad \phi \in [0, 2\pi) \quad (3.11)$$

If $\alpha = 2$, the random variable is a complex isotropic Gaussian random variable. In this case, the isotropy condition is satisfied by X for i.i.d. X_1 and X_2 with Gaussian distributions. This is the well known fact that complex Gaussian noise has independent real and imaginary components.

For $\alpha < 2$, the X_1 and X_2 cannot be independent [72]. This implies that the real and imaginary components of complex isotropic S α S noise processes are dependent.

3.5. Signal-to-Noise Ratio

The performance of communication systems is commonly measured in terms of SNR. As an alternative to SNR, it is also common to use the ratio of signal energy per bit (E_b) to noise spectral density (N_0). Both definitions are in terms of noise power, a quantity which is related to the variance of the noise. As the variance of S α S noise with $\alpha < 2$ is infinite*, this definition cannot be directly used to measure communication performance in an additive S α S noise channel. The signal to dispersion ratio has been previously used as a measure of SNR [50]. As the units of

* As the variance of S α S noise is infinite, the power of discrete-time S α S noise is also infinite. However all practical systems have limited dynamic range. Hence the observed noise will be clipped and thus have finite power.

dispersion depend on the value of α , this definition does not lead to a dimensionless quantity for SNR.

We define N_0 in terms of the dispersion (γ) of the S α S noise, such that

$$\gamma = \left(\frac{\sqrt{N_0}}{2} \right)^\alpha. \quad (3.12)$$

When $\alpha = 2$, this definition reduces to the standard definition of N_0 for Gaussian white noise:

$$\begin{aligned} \gamma &= \left(\frac{\sqrt{N_0}}{2} \right)^2 = \frac{N_0}{4} \\ \therefore 2\gamma &= \frac{N_0}{2} \\ \therefore \sigma^2 &= \frac{N_0}{2} \end{aligned} \quad (3.13)$$

where σ^2 is variance of the Gaussian white noise. Our generalized definition of N_0 is thus consistent with previous literature. We use this generalized definition of N_0 throughout this thesis to compute SNR and E_b/N_0 . This enables us to study the performance of signal processing techniques in S α S noise for a given value of α , by varying SNR as a function of the noise dispersion γ .

3.6. Conclusions

In this chapter, we studied the power spectrum and PDF of ambient noise in WSWA channels. The snapping shrimp dominated ambient noise from these channels has a non-Gaussian PDF. We demonstrated that the S α S distribution accurately models the ambient noise pressure distribution. We listed some of the key properties of S α S distributions that will be useful in subsequent chapters. Finally, we modified

the commonly used definition of SNR to obtain a useful measure of SNR in SoS noise.

4. Signal Detection in S α S Noise

In the previous chapter, we have shown that the ambient noise in WSWA channels is accurately modeled using the S α S distribution. In this chapter, we look at a common problem in communication systems where a known signal is to be detected in an additive noise channel, where the noise is S α S distributed and uncorrelated [74].

4.1. Signal Detection

Detection of a known signal with unknown amplitude in noise has important applications in communication systems. Known signals are commonly used as preambles to help achieve frame synchronization. A set of pre-determined signals is also used as a signal constellation in most modulation schemes used in communication.

Conventional communication systems make the assumption that the noise is additive white Gaussian in nature. Although this leads to a simple linear detector structure, the receiver is sub-optimal if the assumption is not met [21]. The ambient noise in WSWA channels is represented accurately by a S α S random process with α between 1.5 and 1.9. The impulsive nature of this noise significantly degrades the performance of conventional communication systems. Non-linear detectors can be developed for optimal or near-optimal performance in non-Gaussian noise; we shall explore a few such detectors in this chapter.

4.2. Locally Optimal Detector

Nikias and Shao have explored the development of optimal detectors in the presence of S α S noise [50]. They showed that a globally optimal (commonly known

as *uniformly most powerful* or UMP) receiver does not exist in the general S α S noise case. However, locally optimal (LO) detectors can be designed for detection of weak signals by introducing a non-linear transfer function before a standard linear correlation (LC) detector. These detectors perform better than LC detectors in detecting weak signals in the presence of S α S noise. The non-linear transfer function can be determined from the noise PDF [50]:

$$g(x) = -\frac{1}{f_{\alpha}(x; \gamma)} \frac{\partial f_{\alpha}(x; \gamma)}{\partial x} \quad \text{where } f_{\alpha}(x; \gamma) \text{ is the noise PDF.} \quad (4.1)$$

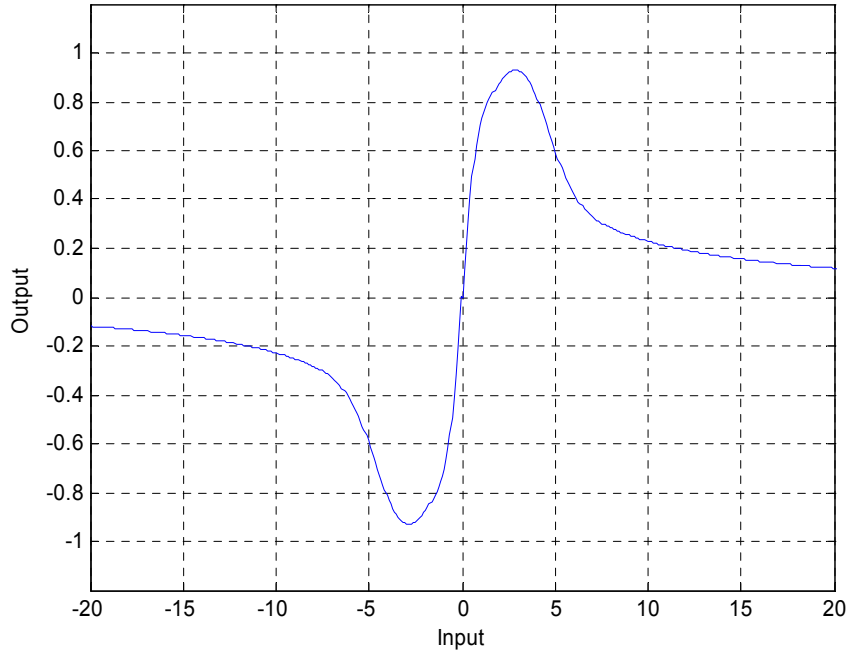


Figure 4.1. Sample LO transfer function for S α S with $\alpha = 1.5$ and $c = 1$

A typical transfer function is shown in Figure 4.1. For small values, the transfer function is approximately linear. For large values, the transfer function vanishes. This retains weak signals with minimal distortion while suppressing large amplitude noise, thus improving detector performance for very weak signals. However, when the signal is stronger, the signal gets distorted as well and the performance of the detector drops.

4.3. Maximum Likelihood Estimator

A maximum likelihood (ML) estimator can be developed for signals of arbitrary strength in S α S noise. Letting s_k be the signal, A the signal strength, n_k the noise and k be the discrete-time index, the observed data x_k can be written as

$$x_k = As_k + n_k. \quad (4.2)$$

Given the noise PDF $f_n(n)$ of n_k , a likelihood function L can be developed as a function of the estimated signal strength A as

$$L = \prod_k f_n(x_k - As_k). \quad (4.3)$$

Maximizing the likelihood L , or equivalently minimizing the negative log-likelihood \tilde{L} then gives us the best estimate of signal strength \hat{A} :

$$\begin{aligned} \tilde{L} &= -\log L = -\sum_k f_n(x_k - As_k) \\ \hat{A} &= \arg \min_A \tilde{L} \end{aligned} \quad (4.4)$$

The estimated signal strength is expected to be close to zero when no signal is present.

For the S α S distribution, the minimization of \tilde{L} does not yield a closed-form solution in general. Numerical minimization of \tilde{L} leads to an optimal estimate of signal strength, but typically it is computationally very intensive.

In the special case of $\alpha = 2$ and real x_k and s_k , the S α S distribution reduces to a Gaussian distribution and the minimization results in the familiar LC detector.

$$\hat{A} = \frac{\sum_t x_k s_k}{\sum_t |s_k|^2} \quad (4.5)$$

4.4. Sign Correlation Detector

The sign correlation (SC) detector is obtained by the introduction of a simple non-linearity (the sign function, sgn) in the LC detector. It is known that the sign correlation detector has robust performance in many types of non-Gaussian noise^{*} [66]. As the detection statistic does not have any interpretation as an estimate of signal strength, the scale factor (denominator) in the linear correlation estimator can be dropped. The SC detector is thus given by

$$T = \sum_t \text{sgn}(x_k) s_k \quad (4.6)$$

where

$$\text{sgn}(x) = \begin{cases} 1 & \text{if } x > 0 \\ 0 & \text{if } x = 0 \\ -1 & \text{if } x < 0. \end{cases}$$

The sign correlation detector is computationally simple and easy to implement, but sub-optimal. It has the advantage that it is non-parametric i.e. the parameters of the noise PDF are not required.

4.5. Simulated Detection Performance

We tested the effectiveness of LC, ML, LO and SC detectors for detecting a signal in additive ambient noise using Monte-Carlo simulations with 50,000 iterations. During each iteration, a direct-sequence spread spectrum signal (50 kHz center frequency, 15 kHz spread, 2 ms length) was randomly added to a recorded ambient noise sample ($\alpha = 1.9$). The detection performance of the detectors was then computed based on their ability to correctly determine the presence or absence of the

^{*} The SC detector is a locally optimal detector in double exponential density noise.

signal. The simulations were repeated for varying values of signal strength to test performance as a function of SNR.

Figure 4.2 shows the detection performance for the detectors at a low SNR of 5 dB. It is seen that the ML and LO detectors display the best performances with the SC detector slightly worse than these optimal detectors. The LC detector has the worst performance as it is unable to achieve low false alarm probabilities (P_{FA}). At higher P_{FA} , the LC detection probability is slightly better than the SC. However, it is more common to operate the detector at low values of P_{FA} .

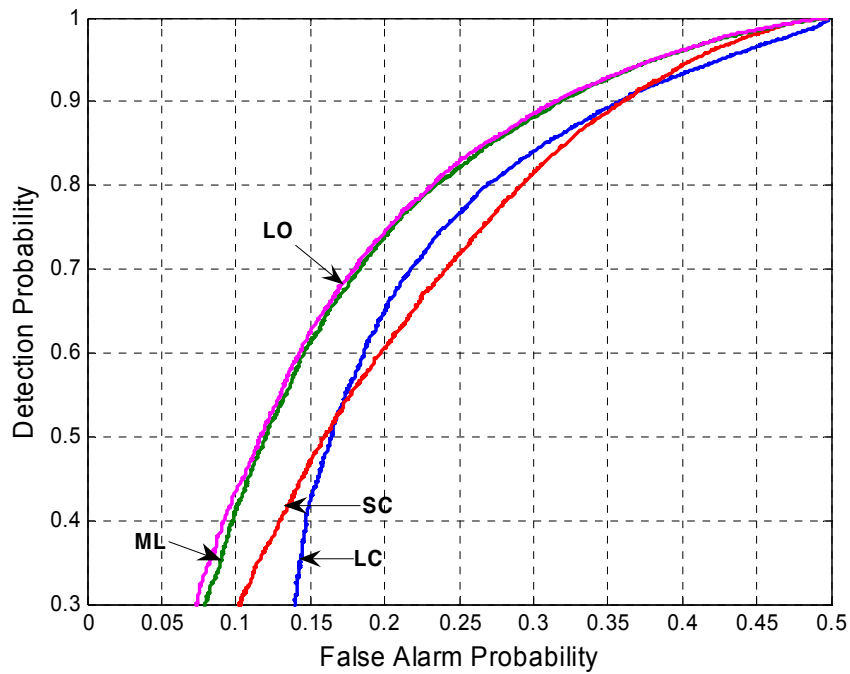


Figure 4.2. Detection performance for ML, LO, SC and LC detectors at SNR of 5 dB

Figure 4.3 shows the detection performance at a moderate SNR of 10 dB. The same trend is clearly visible; the ML and LO detectors are the best, followed by the SC and then the LC. The LC again cannot achieve as low a P_{FA} as the others. At high values of detection probability and consequently P_{FA} , the LC performance is slightly worse than the other detectors. At intermediate values of P_{FA} , the SC and LC performances are similar, but not as good as the ML and LO detectors.

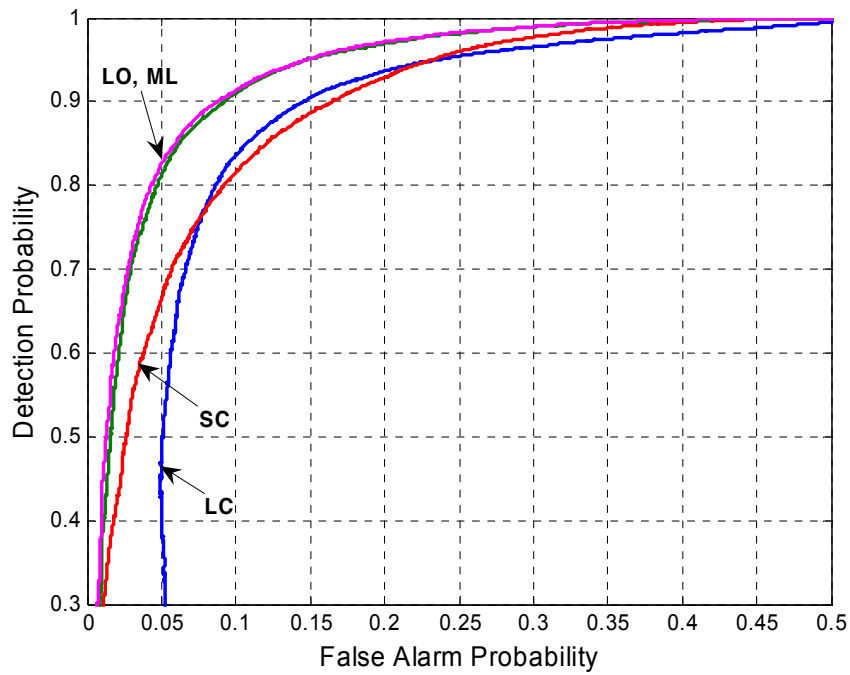


Figure 4.3. Detection performance for ML, LO, SC and LC detectors at SNR of 10 dB

At a high SNR of 15 dB, the SC performs only slightly worse than the ML and LO (Figure 4.4). The LC is consistently inferior; it fails to achieve low P_{FA} and this trend continues even at higher SNR.

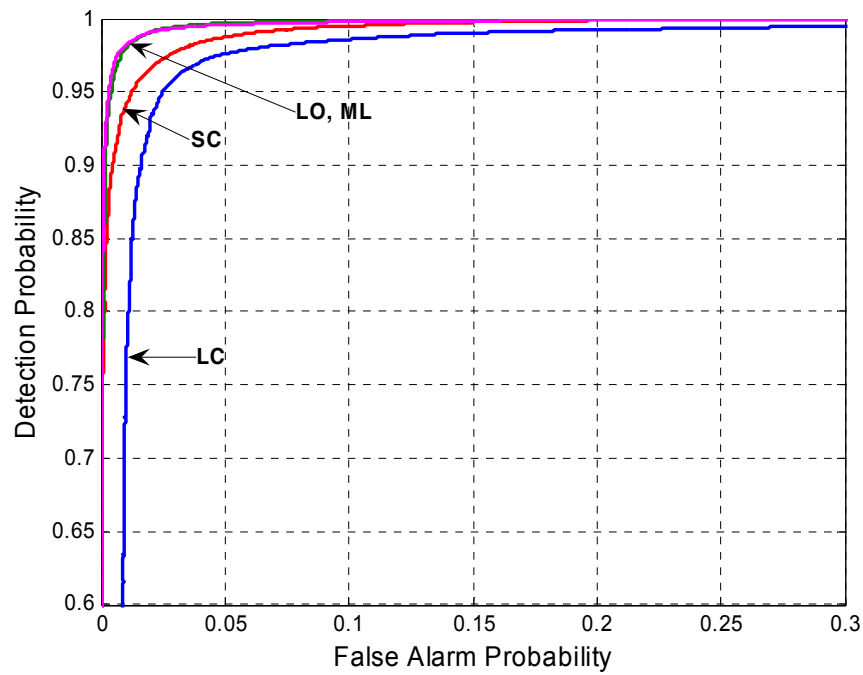


Figure 4.4. Detection performance for ML, LO, SC and LC detectors at SNR of 15 dB

Figure 4.5 shows the performances of the detectors over a SNR range from 0 dB to 30 dB for a probability of false alarm of 10^{-3} selected by choosing a detection threshold empirically. Although the detection curves suggest that the ML and LO detectors are significantly better than the SC detector, the performance of the SC detector is only slightly inferior to the ML and LO detectors. The LC detector is considerably poorer, with a requirement of about 5-10 dB extra SNR to deliver the same detection performance as the other detectors. The LC detector performance shows considerable variation as its performance does not asymptotically converge due to the infinite variance of the SoS noise.

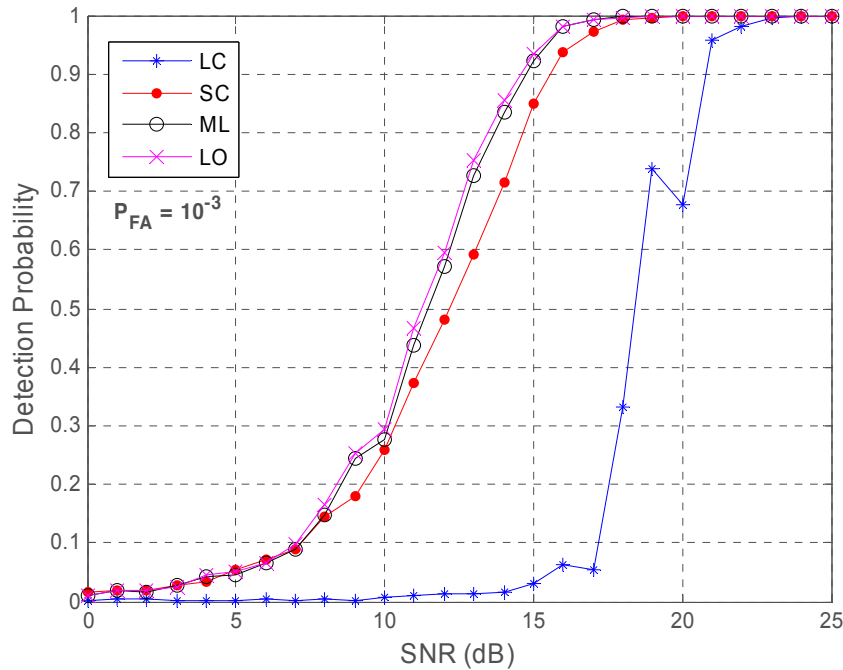


Figure 4.5. Performance of a detector based on ML, LO, SC and LC

The near-optimal performance and low complexity of the SC detector at low SNR makes it attractive for use as a detector in snapping-shrimp dominated ambient noise channels. When performance requirements are critical and the noise probability distribution parameters are known, an ML or LO detector may be used. The LO detector is simpler to implement and computationally less intensive than the ML

detector. However, the latter has the advantage that it also provides an estimate of the signal amplitude, which the LO and SC detectors cannot do.

4.6. *Experimental Validation*

Although the simulations used ambient noise data recordings from the sea, actual mixing of the noise with the signal was performed numerically. The tests suggested that the SC detector should have a superior performance to the LC detector for data recorded in Singapore waters. To test whether this is indeed true, we tested both detectors with field data. The ML and LO detectors were not tested due to computational limitations and the unavailability of independent ambient noise samples to obtain detailed noise statistics.

A spread-spectrum signal with center frequency 40 kHz, spread 40 kHz and duration 30 ms was transmitted and recorded over a distance of 550 m in Singapore waters. The signal was repeated 100 times at a repetition rate of 10 transmissions per second. The signal was acquired at a sampling rate of 250 kSa/s and stored for later analysis.

Before detection, the received signal was pre-whitened and band-pass filtered to reduce out-of-band noise. The pre-whitening is necessary to compensate for the low-pass filtering effect of the ocean as a result of higher absorption at high frequencies. The filtered signal was then passed through LC and SC detectors with a threshold chosen to satisfy a P_{FA} of 10^{-6} . For this false alarm rate and a 10 second data set sampled at 250 kSa/s, one would expect 2.5 false alarms. Of the 100 transmissions, the LC detector correctly identified 40 transmissions with 3 false alarms. The SC detector correctly identified 59 transmissions with 1 false alarm. The performance of the SC was better than the LC in terms of detection probability and number of false

alarms. As the SNR during the experiment is unknown, the results cannot be compared to the simulated results. However, the prediction that the SC performs better than the LC at low P_{FA} is validated by the experimental data.

4.7. Conclusions

The knowledge of the noise probability distribution of ambient noise has enabled us to develop optimal ML and LO detectors. The performance of these detectors was found to be significantly better than the conventional LC detector. For weak signals, a lower SNR could produce the same detection performance if an optimal detector is used instead of a LC detector. When the noise distribution parameters are unknown, a non-parametric SC detector may be used. The performance of this detector was found to be comparable but slightly inferior to the optimal detectors. The simple implementation and near-optimal performance of the SC detector make it an attractive choice for communication systems in the presence of S α S noise.

5. *Communication in S α S Noise*

In Chapter 3, we have shown that the ambient noise in WSWA channels is accurately modeled using the S α S distribution. In Chapter 4, we analyzed the performance of linear and non-linear detectors in the presence of S α S noise. In this chapter, we analyze the performance of antipodal signaling in the presence of S α S noise. We also analyze the performance of coded communications based on antipodal signaling in the S α S noise channel using Viterbi decoding. We show that the use of a 1-norm metric (rather than the commonly used Euclidean metric) provides robust soft-decision decoding performance in the presence of S α S noise [75].

5.1. *Antipodal Signaling*

Antipodal signaling is one of the basic signaling methods in digital communications. The commonly used BPSK modulation is antipodal. Although QPSK is not antipodal, a QPSK-based communication system is modeled using a pair of orthogonal BPSK systems. However, such analysis should take into consideration that the complex isotropic S α S noise process, which is relevant for QPSK systems has dependent real and imaginary components (Theorem 7). More complex modulation schemes such as OFDM often use BPSK or QPSK to modulate individual sub-carriers. Thus these schemes can also be analyzed in terms of antipodal signaling.

Additive white Gaussian noise (AWGN) is perhaps the most common noise model used for the analysis of communication systems. The use of Gaussian noise is justified by the central limit theorem which states that the sum of a large number of i.i.d. finite variance random variables tends towards a Gaussian distribution. The use is further motivated by the fact that the Gaussian distribution has an exponential form

which leads to mathematically tractable closed-form solutions in most cases. Antipodal communications in AWGN is well studied.

In the case of the WSWA channel, the noise is known to be highly non-Gaussian. Antipodal communications in the presence of non-Gaussian noise has received comparatively little attention. In this chapter, we develop a framework for the analysis of uncoded and coded antipodal communications in presence of non-Gaussian noise modeled using the S α S distribution.

We consider a channel which corrupts a signal only via additive S α S noise. If signal x_k is passed through the channel, we receive y_k such that

$$y_k = x_k + n_k \quad (5.1)$$

where n_k is a sequence of independent S α S noise samples. In line with an AWGN channel, we call this channel an additive white S α S noise (AWS α SN) channel. As ambient noise samples typically yield values of α between 1.5 and 1.9, we analyze the performance of this channel under the assumption $\alpha > 1$.

5.2. Tail Probability of S α S Noise

The tail probabilities of the noise distribution are of interest in analysis of communication systems. In the case of AWGN, the tail probability of the Gaussian distribution is of interest. This is defined by the commonly used Q function:

$$Q(x) = 1 - F_2\left(x, \frac{1}{2}\right) = \frac{1}{\sqrt{2\pi}} \int_x^\infty \exp\left(-\frac{t^2}{2}\right) dt \quad (5.2)$$

Analogous to the Q function, we define a tail probability function $Q_\alpha(x)$ for the S α S distribution:

$$Q_\alpha(x) = \int_x^\infty f_\alpha(t, 1) dt \quad (5.3)$$

The choice of $\gamma = 1$ ensures that $Q_\alpha(x)$ reduces to $Q(x)$ when $\alpha = 2$. $Q_\alpha(x)$ is not known in closed-form. However, we can list several useful properties of this function:

1. The tail probability function is the complement of the standard cumulative distribution function:

$$Q_\alpha(x) = 1 - F_\alpha(x; 1) \quad (5.4)$$

2. For $\alpha = 1$, $Q_\alpha(x)$ is known in closed-form. From Theorem 5 and (5.4), we have:

$$Q_1(x) = 1 - F_1(x; 1) = \frac{1}{2} - \frac{1}{\pi} \arctan(x) \quad (5.5)$$

3. For $\alpha = 2$, $Q_\alpha(x)$ can be defined in terms of $Q(x)$:

$$Q_2(x) = Q\left(\frac{x}{\sqrt{2}}\right) \quad (5.6)$$

4. The asymptotic behavior of the tail probability is given by the algebraic tail behavior of stable distributions (Theorem 6):

$$\lim_{x \rightarrow \infty} Q_\alpha(x) = \frac{C_\alpha}{2} x^{-\alpha} \quad (5.7)$$

5. The tails of the S α S distribution become heavier as α decreases. Provided x is not too small ($x > 1$), the tail probability is bounded by the Gaussian and Cauchy tail probabilities:

$$Q_2(x) \leq Q_\alpha(x) < Q_1(x) \quad (5.8)$$

5.3. Antipodal Signaling in S α S Noise

In the following analysis we assume that bits 0 and 1 are transmitted with equal probability. Antipodal signals ψ_0 and ψ_1 (representing 0 and 1 respectively) can be represented in a one-dimensional signal space:

$$\begin{aligned}
x_t &= \psi_0 \text{ or } \psi_1 \\
\psi_0 &= -\sqrt{E_b} \\
\psi_1 &= \sqrt{E_b}.
\end{aligned} \tag{5.9}$$

The performance of a communication system is usually measured in terms of the probability of bit error P_b . It can be expressed in terms of the tail probability of the noise for any γ as $\gamma^{1/\alpha}$ is a scale parameter of the SoS distribution [50], such that

$$P_b = Q_\alpha \left(\frac{\sqrt{E_b}}{\gamma^{1/\alpha}} \right) = Q_\alpha \left(\frac{\sqrt{E_b}}{\sqrt{N_0}/2} \right) = Q_\alpha \left(2\sqrt{\frac{E_b}{N_0}} \right). \tag{5.10}$$

For $E_b/N_0 > 0.25$ (i.e. -6 dB), P_b is upper bounded by the tail probability of the impulsive Cauchy distribution. From Theorem 5 and (5.10), we have

$$P_b < \frac{1}{2} - \frac{1}{\pi} \arctan \left(2\sqrt{\frac{E_b}{N_0}} \right) \quad \text{if } \frac{E_b}{N_0} \geq \frac{1}{4}. \tag{5.11}$$

For large E_b/N_0 , the performance can be approximated using the asymptotic tail probability. From (5.10) and (5.7), we have

$$\begin{aligned}
P_b &= \frac{C_\alpha}{2} \left(2\sqrt{\frac{E_b}{N_0}} \right)^{-\alpha} \quad \text{as } \frac{E_b}{N_0} \rightarrow \infty \\
&= \frac{C_\alpha}{2^{1+\alpha}} \left(\frac{E_b}{N_0} \right)^{-\alpha/2}.
\end{aligned} \tag{5.12}$$

When $\alpha = 2$, (5.10) and (5.6) gives us the well known probability of bit error in case of antipodal BPSK in AWGN as

$$P_b = Q \left(\sqrt{2\frac{E_b}{N_0}} \right) \quad \text{if } \alpha = 2. \tag{5.13}$$

The numerical approximation of (5.10) based on (5.4) and [67], the Cauchy upper bound (5.11), the asymptotic approximation (5.12) and the AWGN case (5.13) are compared against simulation results in Figure 5.1. The random SoS noise samples were generated for the simulation using the method described in [76].

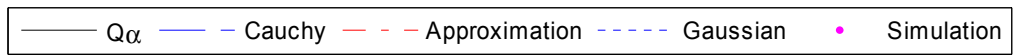
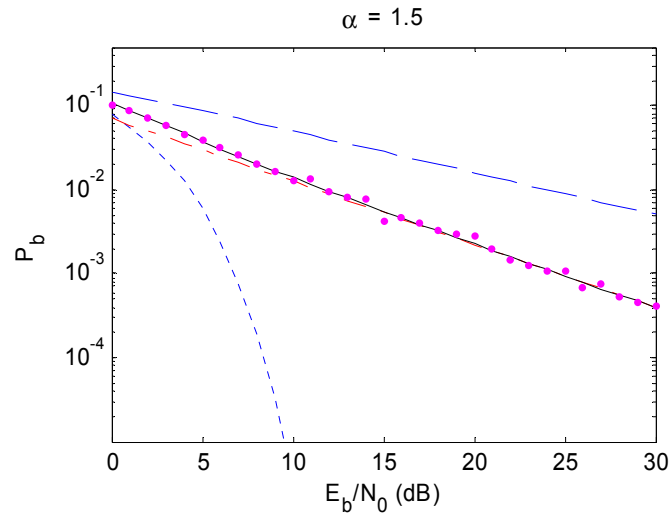
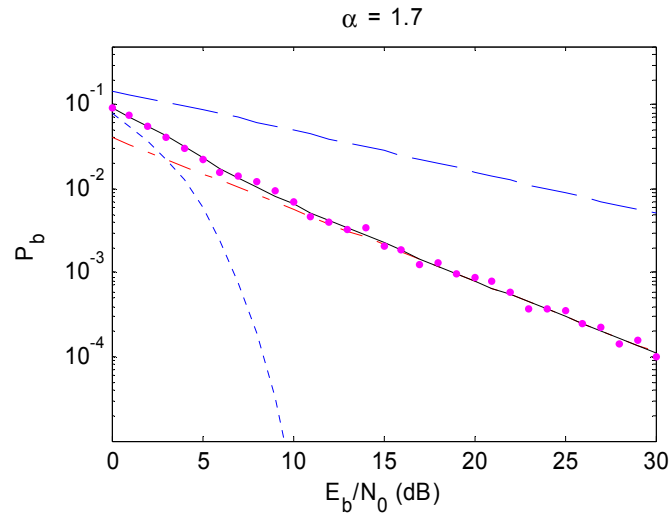
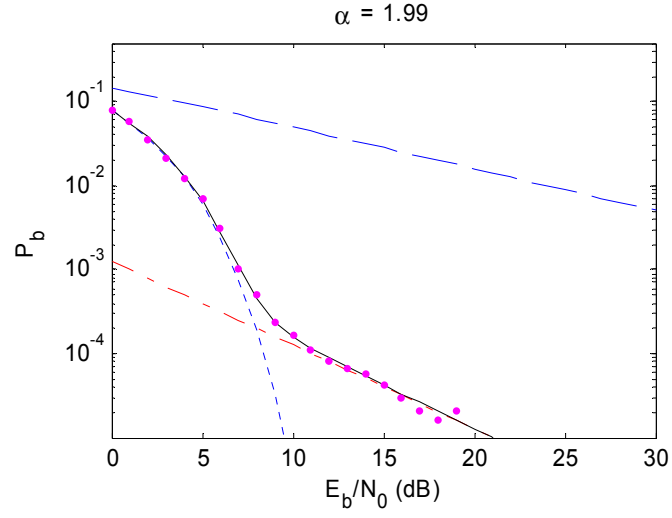


Figure 5.1. Detection performance for antipodal signaling in AWS α SN for various values of α - based on Q_α , Cauchy upper bound, asymptotic approximation, performance in Gaussian noise and simulation results

It can be seen from Figure 5.1 that the simulation results agree closely with the theoretical prediction based on (5.10). The performance in AWS α SN is significantly poorer at high E_b/N_0 as compared to AWGN even when the deviation from Gaussian noise is small (e.g. $\alpha = 1.99$). At high values of α and low E_b/N_0 , the performance is similar to the AWGN channel. At high E_b/N_0 , the asymptotic approximation is quite accurate. The Cauchy upper bound is quite loose at high E_b/N_0 , especially when the value of α is also high.

5.4. Coded Communications in S α S Noise

5.4.1. Viterbi Decoding of Convolutional Codes

Convolutional codes are among the popular error control codes, routinely used in communication applications today. Convolutional codes can be represented using a trellis. The Viterbi decoding algorithm provides an efficient yet optimal algorithm to decode convolutional codes by searching through the trellis for the most probable sequence.

We summarize the Viterbi algorithm here based on the description in [77]. A more complete treatment of the Viterbi algorithm is presented in [77] and [18].

1. Assuming that the convolutional encoder is at state zero initially, assign Viterbi metric zero to the initial node. Set depth m to zero.
2. Increment m by 1. For each node j at depth m , find for each of the predecessor i at depth $m-1$ the sum of the Viterbi metric of the predecessor and the branch metric m_{ij} of the connecting branch. Determine the maximum (in case of a likelihood metric, or minimum in case of cost metric) of these sums and assign it to this node; label the node with the shortest path to it.

3. If we have reached the end of the trellis, then stop and choose as the decoded codeword a path to the terminating node with the largest Viterbi metric; otherwise go to step 2.

The exact probability of bit error for a coded communication system with Viterbi decoding is difficult to determine. However, an upper bound on the probability of bit error can be obtained in terms of the information error weight coefficients c_d [18] as

$$P_b < \sum_{d=d_f}^{\infty} c_d p_d \quad (5.14)$$

where d_f is the free distance of the code and p_d is the pairwise probability of error with weight d . The free distance d_f and the weights c_d for some good codes are published in papers such as [78]. Although the summation in (5.14) has an infinite number of terms, the series is convergent and the terms decrease in magnitude. Typically, the summation of the first few terms provides an acceptable upper bound.

In the following sections, we analyze the performance of the Viterbi algorithm to decode convolutional codes in the presence of S α S noise.

5.4.2. Hard-decision Decoding

In a hard-decision decoded communication system, the receiver determines each received bit based on the output of the detector. The decisions are fed to the Viterbi decoder. The decoder selects the most likely transmitted data by minimizing the Hamming distance between the received data and all possible transmitted code words i.e. the Viterbi branch metric is the Hamming distance.

Hard-decision decoding effectively converts the AWS α SN channel into a binary symmetric channel (BSC) with a transition probability given by

$$\varepsilon = Q_\alpha \left(2 \sqrt{\frac{E_c}{N_0}} \right) \quad (5.15)$$

where E_c is the energy per coded bit. If R is the code rate,

$$E_c = RE_b. \quad (5.16)$$

$$\therefore \varepsilon = Q_\alpha \left(2 \sqrt{R \frac{E_b}{N_0}} \right). \quad (5.17)$$

The pairwise probability of error for a BSC is upper bounded by [18;77]

$$p_d < \left(2\sqrt{\varepsilon(1-\varepsilon)} \right)^d. \quad (5.18)$$

Combining (5.14) and (5.18), we have

$$P_b < \sum_{d=d_f}^{\infty} c_d \left(2\sqrt{\varepsilon(1-\varepsilon)} \right)^d. \quad (5.19)$$

5.4.3. Maximum Likelihood Decoding

The Viterbi algorithm can be used with unquantized decisions from the detector to perform maximum likelihood decoding of the received sequence. The branch metric used for unquantized maximum likelihood decoding is the logarithm of the joint probability of the sequence conditioned on the transmitted sequence [18]

$$^m_{ij} = \log p(\mathbf{y} | \mathbf{x}^m_{ij}) \quad (5.20)$$

where $^m_{ij}$ is the branch metric for node j at depth m and predecessor i , \mathbf{y} is the received sequence, \mathbf{x}^m_{ij} is the transmitted sequence for the branch and $p(\mathbf{y}|\mathbf{x})$ is the conditional probability function or conditional probability density function of the received sequence conditioned on the transmitted sequence.

In the case of the AWS α SN channel, $p(\mathbf{y}|\mathbf{x})$ is given by

$$p(\mathbf{y} | \mathbf{x}) = \prod_k f_\alpha(y_k - x_k; \gamma) \quad (5.21)$$

The pairwise probability of error is then [77]

$$p_d = P\left(\sum_{k=1}^d \log \frac{p(y_k | x_k = \psi_1)}{p(y_k | x_k = \psi_0)} > 0\right) \quad (5.22)$$

where $P(X)$ denotes the probability of event X and the probability of error is measured without loss of generality between a codeword with weight d and the all zero codeword.

In case of the AWS α SN channel, (5.22) cannot be simplified any further. Hence we are unable to obtain an analytical bound on the performance. However, we can implement the branch metric specified by (5.20) and (5.21) and investigate the performance of the maximum likelihood decoder via simulation. The results from such simulations are presented later in this chapter.

5.4.4. Euclidean Norm Branch Metric

In an AWGN channel, (5.20) and (5.22) can be simplified further. From (5.21) with $\alpha = 2$, Theorem 5 and (5.20), we have

$$\begin{aligned} m_{ij}^m &= \sum_{k=1}^d \left[-\log(2\sqrt{\pi\gamma}) - \frac{(y_k - x_{ijk}^m)^2}{4\gamma} \right] \\ &= -d \log(2\sqrt{\pi\gamma}) - \frac{1}{4\gamma} \sum_{k=1}^d (y_k - x_{ijk}^m)^2. \end{aligned} \quad (5.23)$$

As the Viterbi metric can be translated and scaled without any effect on the algorithm, we can simplify the branch metric further to

$$m_{ij}^m = -\sum_{k=1}^d (y_k - x_{ijk}^m)^2. \quad (5.24)$$

This is the Euclidean norm branch metric, commonly used in the soft-decision Viterbi algorithm. It is equivalent to the maximum likelihood metric when the channel is AWGN. However, in the AWS α SN channel, the Euclidean norm metric is not optimal.

From (5.21) with $\alpha = 2$, Theorem 5 and (5.22), we have

$$\begin{aligned}
p_d &= P\left(\sum_{k=1}^d \frac{1}{4\gamma} \left\{ (y_k - \sqrt{E_c})^2 - (y_k + \sqrt{E_c})^2 \right\} > 0\right) \\
&= P\left(\sum_{k=1}^d -\frac{y_k \sqrt{E_c}}{\gamma} > 0\right) = P\left(\sum_{k=1}^d y_k < 0\right).
\end{aligned} \tag{5.25}$$

As the transmitted codeword has weight d , we can assume $x_1 \dots x_d$ to be 1. Substituting (5.1) and (5.16) in the above, we get

$$\begin{aligned}
p_d &= P\left(\sum_{k=1}^d (x_k + n_k) < 0\right) \\
&= P\left(d\sqrt{RE_b} + \sum_{k=1}^d n_k < 0\right).
\end{aligned} \tag{5.26}$$

The noise term $\sum n_k$ is the sum of d SoS random variables with dispersion γ . From Theorem 1, the sum is also a SoS random variable with dispersion $d\gamma$. Using (3.12) and (5.25), we get

$$\begin{aligned}
p_d &= Q_\alpha\left(\frac{d\sqrt{RE_b}}{(d\gamma)^{1/\alpha}}\right) \\
&= Q_\alpha\left(2d^{1-1/\alpha} \sqrt{R \frac{E_b}{N_0}}\right).
\end{aligned} \tag{5.27}$$

Substituting (5.27) in (5.14), we get an upper bound on the bit error probability for Viterbi decoding with Euclidean metric in an AWS α SN channel as

$$P_b < \sum_{d=d_f}^{\infty} c_d Q_\alpha\left(2d^{1-1/\alpha} \sqrt{R \frac{E_b}{N_0}}\right). \tag{5.28}$$

5.4.5. 1-norm Branch Metric

As the variance of SoS random variables is infinite, the expected value of the Euclidean norm metric in (5.24) is infinite. Hence the Viterbi algorithm does not perform well with this metric.

It is known that the p -norm ($p < \alpha$) is often a more robust cost function than the Euclidean norm in the presence of α -stable noise [50]. Inspired by this heuristic, we

use the p -norm as a branch metric for the Viterbi algorithm in presence of S α S noise. For mathematical simplicity and because $\alpha > 1$, we select $p = 1$. This yields the 1-norm branch metric which has been noted for its robustness in non-Gaussian noise [79;80]

$$m_{ij} = -\sum_{k=1}^d |y_k - x_{ijk}^m|. \quad (5.29)$$

The probability of bit error is then given by

$$p_d = P\left(\sum_{k=1}^d \left\{ |y_k - \sqrt{E_c}| - |y_k + \sqrt{E_c}| \right\} > 0\right). \quad (5.30)$$

We introduce a new function $g(y)$ for convenience:

$$\begin{aligned} g(y) &= \frac{1}{2} \left\{ |y + \sqrt{E_c}| - |y - \sqrt{E_c}| \right\} \\ &= \begin{cases} \sqrt{E_c} & \text{if } y \geq \sqrt{E_c} \\ y & \text{if } -\sqrt{E_c} < y < \sqrt{E_c} \\ -\sqrt{E_c} & \text{if } y \leq -\sqrt{E_c}. \end{cases} \end{aligned} \quad (5.31)$$

Hence,

$$p_d = P\left(\sum_{k=1}^d -2g(y_k) > 0\right) = P\left(\sum_{k=1}^d g(y_k) < 0\right). \quad (5.32)$$

As the transmitted codeword has weight d , we can assume $x_1 \dots x_d$ to be 1. Combining (5.1) and (5.32),

$$p_d = P\left(\sum_{k=1}^d g(\sqrt{E_c} + n_k) < 0\right). \quad (5.33)$$

Although the random variable n_k has an infinite variance, the random variable $g(\sqrt{E_c} + n_k)$ has a finite variance as $g(y)$ is bounded. For large d , the summation in (5.33) is the sum of a large number of finite variance i.i.d. random variables and hence approximately Gaussian. The mean and variance of the Gaussian distribution

can be computed if the mean and variance of $g(\sqrt{E_c} + n_k)$ are known. The PDF of $g(\sqrt{E_c} + n_k)$ is given by

$$f_g(x) = \begin{cases} \frac{1}{2} \delta(x - \sqrt{E_c}) + Q_\alpha \left(\frac{2\sqrt{E_c}}{\gamma} \right) \delta(x + \sqrt{E_c}) \\ \quad + f_\alpha(x - \sqrt{E_c}; \gamma) & \text{if } -\sqrt{E_c} \leq x \leq \sqrt{E_c} \\ 0 & \text{otherwise} \end{cases} \quad (5.34)$$

where $\delta(\dots)$ is the Dirac delta function and γ is given by (3.12).

Unfortunately, the mean and variance of $g(\sqrt{E_c} + n_k)$ cannot be evaluated from (5.34) as the PDF $f_\alpha(\dots)$ does not have a closed-form expression. However, we can find an upper bound on p_d by assuming a Cauchy distribution for n_k , which underestimates the mean μ_g and overestimates the variance σ_g^2 of $g(\sqrt{E_c} + n_k)$. With $\alpha = 1$ and from Theorem 5, (5.34) and (5.5), we get

$$\begin{aligned} \mu_g &= \int_{-\sqrt{E_c}}^{\sqrt{E_c}} x f_g(x) dx \\ &= \frac{2\sqrt{E_c}}{\pi} \arctan \left(4 \sqrt{\frac{E_c}{N_0}} \right) - \frac{\sqrt{N_0}}{4\pi} \log \left(1 + 16 \frac{E_c}{N_0} \right) \end{aligned} \quad (5.35)$$

and

$$\begin{aligned} \sigma_g^2 &= \int_{-\sqrt{E_c}}^{\sqrt{E_c}} x^2 f_g(x) dx - \mu_g^2 \\ &= \frac{\sqrt{E_c N_0}}{\pi} - \frac{\sqrt{E_c N_0}}{2\pi} \log \left(1 + 16 \frac{E_c}{N_0} \right) \\ &\quad + E_c - \frac{N_0}{4\pi} \arctan \left(4 \sqrt{\frac{E_c}{N_0}} \right) - \mu_g^2. \end{aligned} \quad (5.36)$$

The approximate mean and variance of the summation in (5.33) are d_g and $d\sigma_g^2$ respectively. Hence,

$$p_d < Q\left(\sqrt{d \frac{\tilde{\sigma}_g^2}{\sigma_g^2}}\right). \quad (5.37)$$

As (5.37) depends only on the ratio of $\tilde{\sigma}_g^2$ and σ_g^2 , we can divide (5.35) by $\sqrt{N_0}$ and (5.36) by N_0 without changing the upper bound on p_d . Combining this with (5.16), we have

$$p_d < Q\left(\sqrt{d \frac{\tilde{\sigma}_g^2}{\sigma_g^2}}\right). \quad (5.38)$$

Substituting (5.38) in (5.14), we get an upper bound on the bit error probability for Viterbi decoding with a 1-norm metric in an AWS α SN channel:

$$P_b < \sum_{d=d_f}^{\infty} c_d Q\left(\sqrt{d \frac{\tilde{\sigma}_g^2}{\sigma_g^2}}\right) \quad (5.39)$$

where

$$\begin{aligned} \tilde{\sigma}_g^2 &= \frac{2}{\pi} \sqrt{R \frac{E_b}{N_0}} \arctan\left(4 \sqrt{R \frac{E_b}{N_0}}\right) \\ &\quad - \frac{1}{4\pi} \log\left(1 + 16R \frac{E_b}{N_0}\right) \\ \tilde{\sigma}_g^2 &= \frac{1}{\pi} \sqrt{R \frac{E_b}{N_0}} - \frac{1}{2\pi} \sqrt{R \frac{E_b}{N_0}} \log\left(1 + 16R \frac{E_b}{N_0}\right) \\ &\quad + R \frac{E_b}{N_0} - \frac{1}{4\pi} \arctan\left(4 \sqrt{R \frac{E_b}{N_0}}\right) - \tilde{\sigma}_g^2. \end{aligned}$$

Due to the Cauchy noise assumption, the above bound is somewhat loose. To obtain a better approximation for higher values of α , we numerically computed the integrals in (5.35) and (5.36) using a numerical approximation of the PDF f_α based on [67]. The ratio $\tilde{\sigma}_g^2/\sigma_g^2$ was computed for values of α in the range 1.1 to 1.9 (in steps of 0.1) and values of E_b/N_0 in the range of 0 dB to 15 dB (in steps of 1 dB). Fitting a

surface on the resulting numerical values of the ratio, we obtained an empirical expression for $\frac{2}{\sigma_g^2}$ in terms of α and E_c/N_0 ,

$$Z_g\left(\frac{E_c}{N_0}; \alpha\right) = \frac{\frac{2}{\sigma_g^2}}{\sigma_g^2} = a_\alpha \left(\frac{E_c}{N_0}\right)^{b_\alpha} \quad (5.40)$$

where

$$\begin{aligned} a_\alpha &= \exp(p_{21}\alpha^2 + p_{11}\alpha + p_{01}) \\ b_\alpha &= p_{22}\alpha^2 + p_{12}\alpha + p_{02} \\ p_{21} &= 0.0566, p_{11} = 0.3850, p_{01} = -0.4077 \\ p_{22} &= 0.0766, p_{12} = 0.0417, p_{02} = 0.1860. \end{aligned}$$

Using (5.40), (5.37) and (5.14), we have an approximate bit error probability for Viterbi decoding with a 1-norm metric in an AWS α SN channel,

$$P_b \approx \sum_{d=d_f}^{\infty} c_d Q\left(\sqrt{d Z_g\left(\frac{E_c}{N_0}; \alpha\right)}\right). \quad (5.41)$$

5.4.6. Simulations

We simulated a coded BPSK communication system in an AWS α SN channel for various values of α (between 1.5 and 2) and E_b/N_0 (between 0 and 10 dB). The code used was a 1/2 rate Odenwalder code with constraint length 7, generator polynomials (133, 171 octal) and free distance of 10 [81]. The distance spectrum and information error weights of this code are given in [78].

Viterbi decoding algorithms with hard-decision, maximum likelihood metric, Euclidean norm metric and 1-norm metric were used to decode the data and compute bit error rates (BER). During each run, 10^5 bits were transmitted through the channel. The observed BER was used as an estimate of the probability of bit error (P_b).

The results from these simulations are presented in the next section.

5.4.7. Results

Figure 5.2 compares the theoretical upper bound derived in (5.19) against the simulated performance of hard-decision decoding for varying noise impulsiveness. The bound is approximately 1 dB higher than the simulation results. The performance of the uncoded system is also shown for reference. As expected, the coded system performs better than the uncoded system. The theoretical upper bound derived in (5.28) for Euclidean norm decoding becomes trivial (>1) for most values of α and E_b/N_0 . This is not surprising as the Euclidean norm has an infinite expected value in the presence of SoS noise.

Figure 5.3 compares the theoretical upper bound derived in (5.39) and the closed-form approximation in (5.41) against the simulated performance of 1-norm decoding for varying noise impulsiveness. The upper bound is approximately 2 to 4 dB higher than the simulation results. At high values of α and low values of E_b/N_0 , the bound is quite loose. It becomes tighter when the noise becomes more impulsive and at higher values of E_b/N_0 . The closed-form approximation is quite close to the simulation results for $\alpha = 1.5$ and $\alpha = 1.7$. The performance of the uncoded system is also shown for reference. As expected, the coded system performs better than the uncoded system.

Figure 5.4 compares the performance of various decoding schemes in Gaussian noise. As the Euclidean metric is equivalent to maximum likelihood decoding in Gaussian noise, the two performance curves overlap. The decoding using the 1-norm metric is only slightly inferior to the decoding using the Euclidean metric. As expected, the hard-decision decoding performs about 2 dB worse than the Euclidean metric.

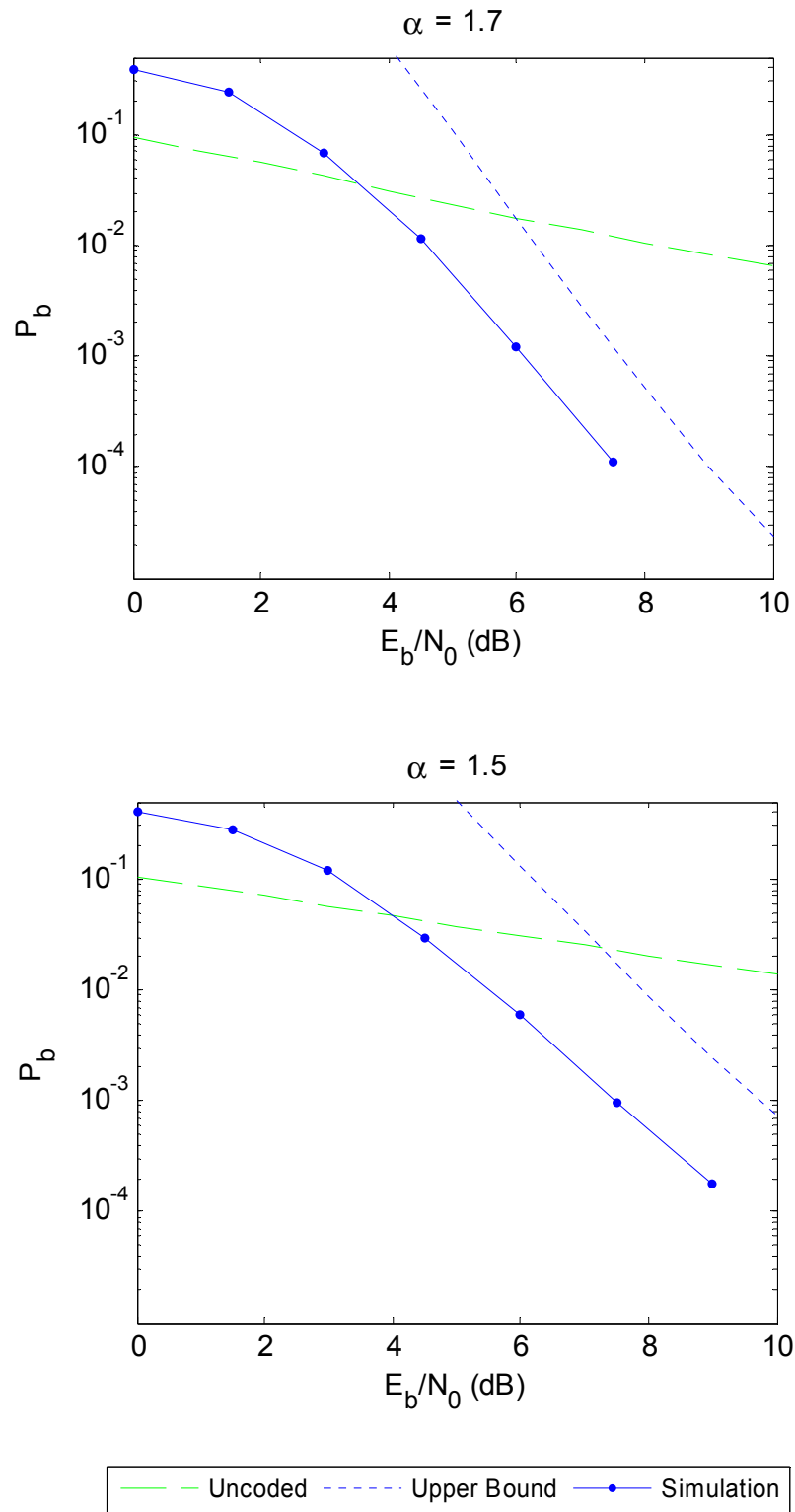


Figure 5.2. Uncoded performance, theoretical upper bound and simulation results for hard-decision decoding

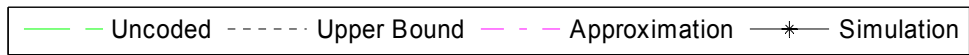
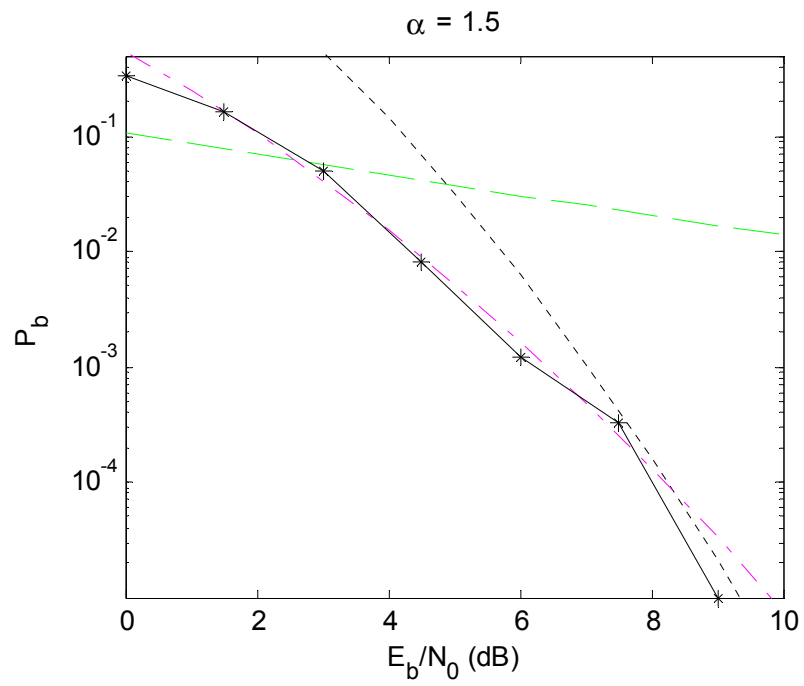
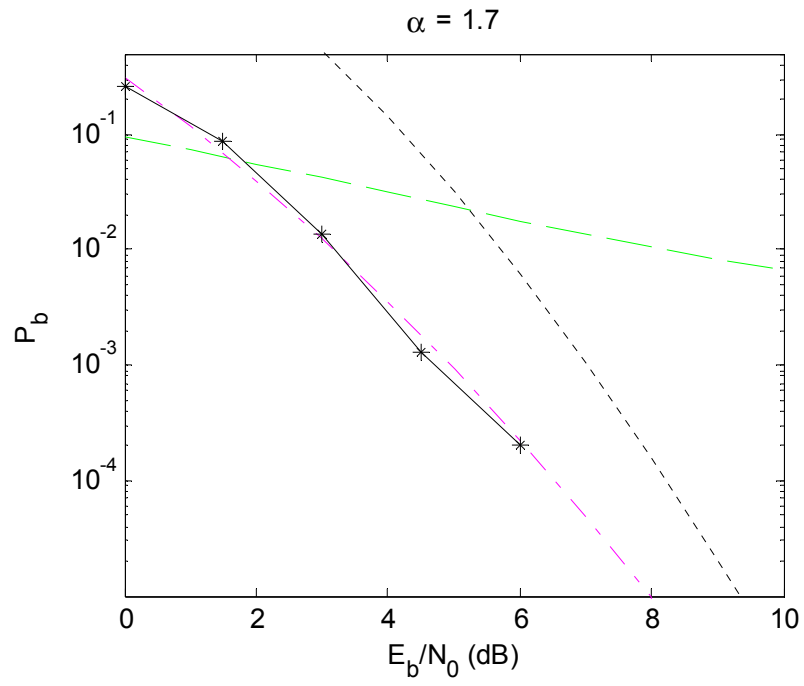


Figure 5.3. Unencoded performance, theoretical upper bound, closed-form approximation and simulation results for 1-norm decoding

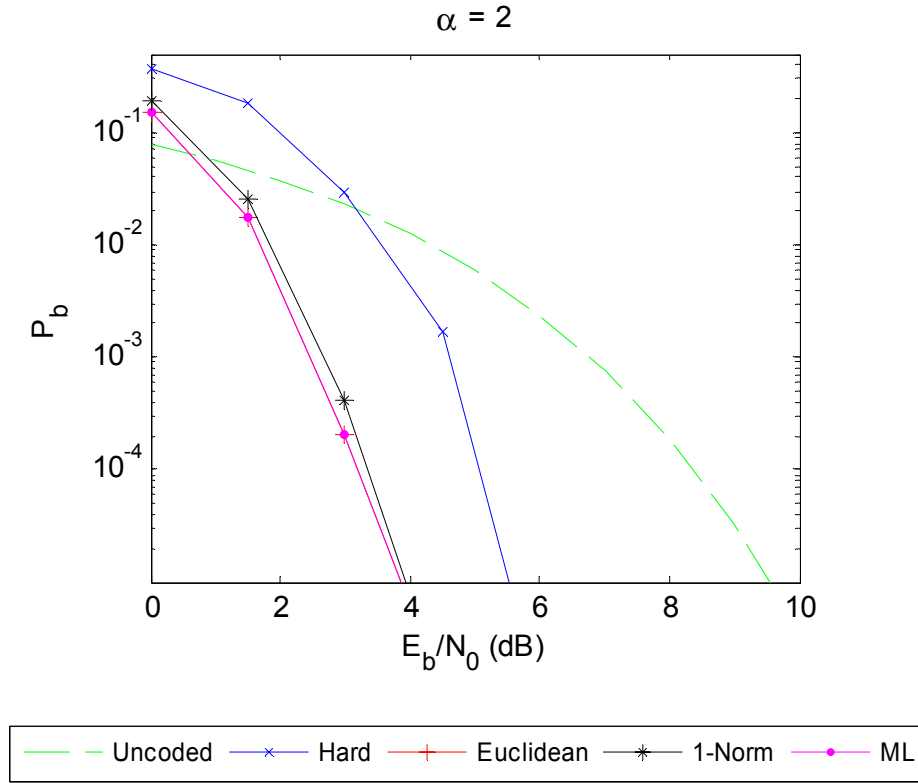


Figure 5.4. Performance of uncoded system in comparison to coded system with hard-decision decoding, Euclidean metric, 1-norm metric and ML decoding in presence of Gaussian noise

Figure 5.5 compares the performance of various decoding schemes in impulsive noise. The decoding with Euclidean metric shows poor performance with little gain over the uncoded system. The hard-decision decoding performs significantly better. As expected, the maximum likelihood decoding is optimal and demonstrates the best performance. It utilizes unquantized detector outputs and performs approximately 2 dB better than the hard-decision decoding. The performance of the decoding using the 1-norm metric is very close to that of the maximum likelihood decoding. As the computational complexity of the 1-norm metric is much lower than the maximum likelihood metric, it is a good alternative to maximum likelihood decoding. The 1-norm metric also has an added advantage that it does not require an estimate of the noise dispersion.

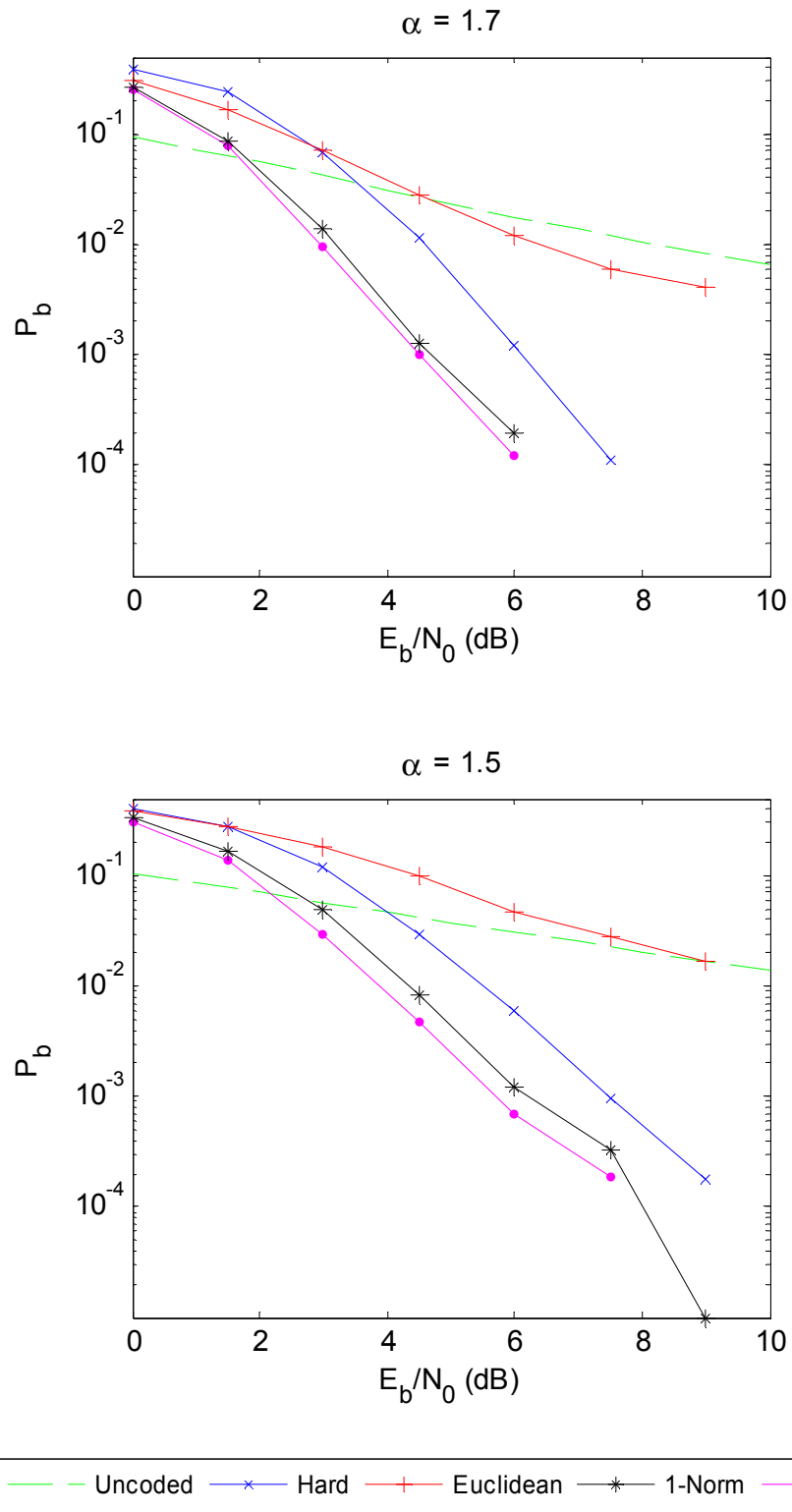


Figure 5.5. Performance of uncoded system in comparison to coded system with hard-decision decoding, Euclidean metric, 1-norm metric and ML decoding

5.5. Conclusions

Although the Gaussian noise assumption is commonly used in the analysis of communication systems, even small deviations from Gaussian-ness can have a severe impact on the performance of communication systems. We have developed an impulsive channel model using additive S α S noise and analyzed the performance of antipodal signaling in the channel.

We have derived theoretical performance bounds for Viterbi decoding of convolutional codes in a S α S noise channel for hard-decision decoding and the commonly used Euclidean metric, which is optimal in Gaussian noise. We have also derived a maximum likelihood Viterbi metric for the S α S noise channel. We adopted a p -norm based metric as an alternative to the Euclidean metric and derived an upper bound and an approximation for its performance.

Through simulations, we found that the p -norm metric (with $p = 1$) is near-optimal in both Gaussian and impulsive S α S noise. The Euclidean metric is optimal in Gaussian noise and its performance is slightly better than that of the 1-norm metric. However, in the presence of impulsive S α S noise, the Euclidean metric performs poorly while the 1-norm metric demonstrates robust performance.

6. Channel Model

In Chapter 3, we showed that the ambient noise in WSWA channel can be modeled using the SoS probability distribution. In Chapters 4 and 5, we studied the problem of signal detection and decoding in AWS α SN channel. Although the noise in the WSWA channel is similar to AWS α SN, the WSWA channel is significantly more complex due to time-varying multipath propagation, frequency-dependent absorption, fading, etc. In this chapter, we develop a mathematical model for signal propagation through the WSWA channel. The model is primarily based on the physics of ocean acoustics. In addition, the model includes some statistical variations which are not included in the physics models that we have incorporated. The channel model is calibrated and validated via experimental channel measurements.

6.1. Physical of Underwater Acoustic Propagation

6.1.1. Ray Model

Acoustic propagation in the ocean is governed by the wave equation. As solutions to the wave equation are difficult to find in general cases, approximations are often used to model propagation. The ray theory provides one such approximation, commonly used for high frequency* propagation modeling [59]. As medium range communication signals are usually high frequency, we use the ray model as a basis for our model of channel propagation.

* An acoustic wave in the ocean is considered as *high frequency* when its wavelength is much smaller than any characteristic length scale such as the water depth, the distance between source and receiver, other inhomogeneities, etc.

In the ray model, sound energy is conceptualized as propagating along *rays*, which are straight lines in the case of an isovelocity* fluid medium. They are partially reflected and partially refracted when they encounter a discontinuity in sound velocity. We model the WSWA channel as a Pekeris waveguide, consisting of an isovelocity layer over an isovelocity half-space (Figure 6.1). The isovelocity layer models the sea water while the isovelocity half-space models the seabed. The isovelocity assumption for sea water is justified as WSWA channels are usually well-mixed and have relatively small increase in pressure over the depth of the water column. The assumption is further supported by numerous sound speed measurements in Singapore waters (Figure 6.2). The sea surface is modeled as a pressure-release boundary.

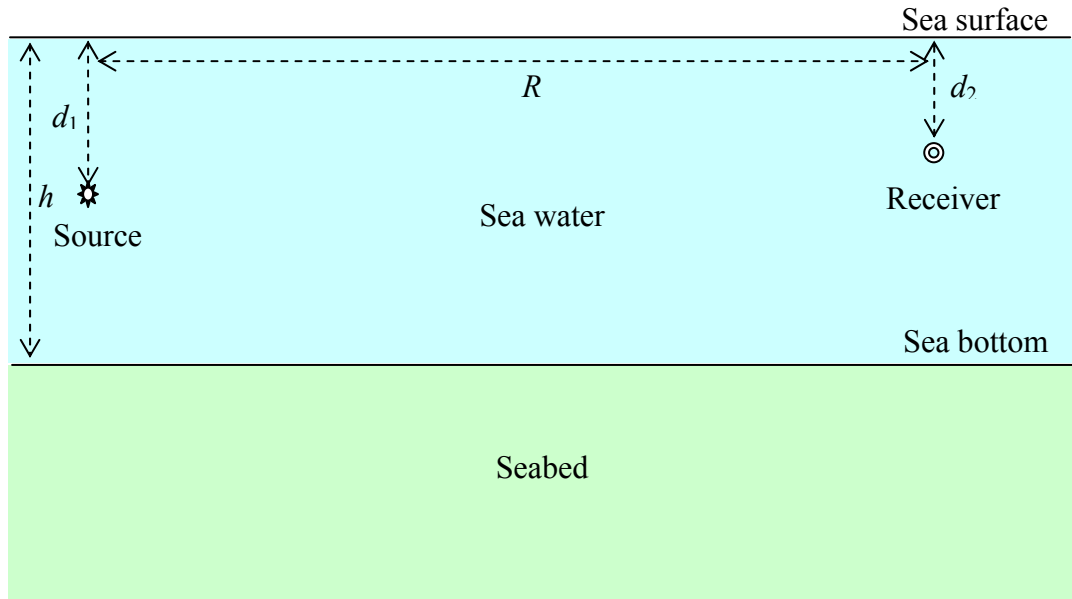


Figure 6.1. Schematic showing a Pekeris waveguide model of the WSWA channel

Let d_1 be the depth of the source, d_2 be the depth of the receiver, h be the height of the water column and R be the transmission range. The distance traveled by the

* *Velocity* here refers to the speed of sound in the fluid.

sound along various eigenrays can be computed using the method of images [59]. The distance along direct eigenray is denoted by D_{00} given by

$$D_{00} = \sqrt{R^2 + (d_1 - d_2)^2} . \quad (6.1)$$

Let D_{sb} be the distance along an upward originating eigenray with s surface reflections and b bottom reflections. For such eigenrays, $0 \leq s-b \leq 1$ and

$$D_{sb} = \sqrt{R^2 + [2bh + d_1 - (-1)^{s-b} d_2]^2} . \quad (6.2)$$

Let \underline{D}_{sb} be the distance along a downward originating eigenray with s surface reflections and b bottom reflections. For such eigenrays, $0 \leq b-s \leq 1$ and

$$\underline{D}_{sb} = \sqrt{R^2 + [2bh - d_1 + (-1)^{b-s} d_2]^2} . \quad (6.3)$$

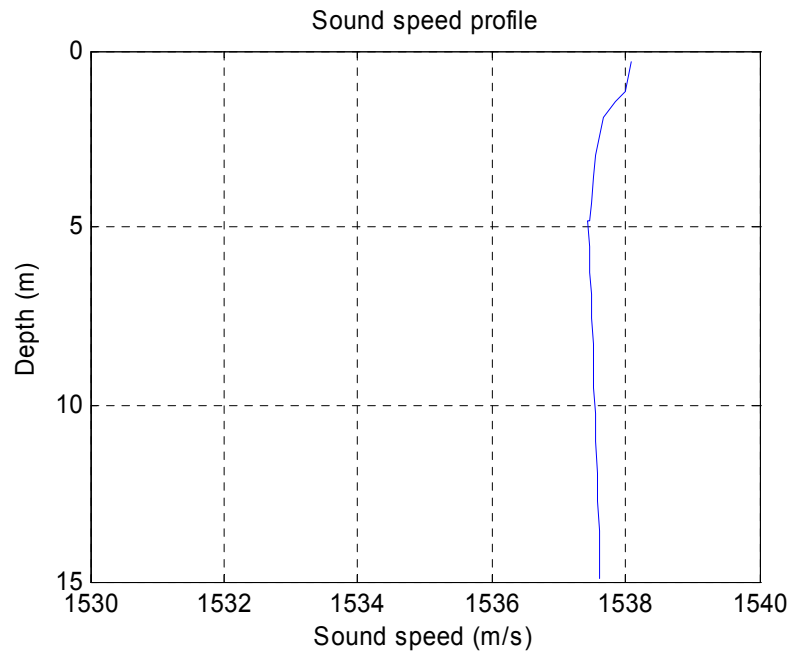


Figure 6.2. A typical sound speed profile from Singapore waters showing variation of less than 1 m/s over the depth of the water column

6.1.2. Sound Speed

Although the sound speed in a WSWA channel does not vary significantly with depth, it varies with temperature and salinity. An empirical relationship between

sound speed (c in m/s), temperature (T in °C) and salinity (S in ‰) at a nominal depth of 10 m is given by [59]

$$c = 1449.36 + 4.6T - 0.055T^2 + 0.00029T^3 + (1.34 - 0.01T)(S - 35). \quad (6.4)$$

6.1.3. Spherical Spreading

We assume that our source is omni-directional and therefore produces a spherical wavefront in an isovelocity medium. The energy intensity at any point along the wavefront will then reduce as the square of the distance traveled by the wave (Gauss' theorem). A factor representing the apparent loss in pressure amplitude due to spherical spreading along an eigenray of length D can be written as

$$L_{ss}(D) = \sqrt{\frac{1}{D^2}} = \frac{1}{D}. \quad (6.5)$$

6.1.4. Volume Absorption

When sound propagates in the ocean, part of the acoustic energy is continuously transformed into heat. This absorption is primarily due to the volume viscosity as a result of relaxation processes in sea water. An empirical expression for the attenuation coefficient β (in dB/km) at a frequency f (in kHz, between 3 kHz and 500 kHz), salinity S (in ‰) and hydrostatic pressure P (in kg/cm²) is given by [59]

$$\beta = 8680 \left(\frac{SAf_T f^2}{f_T^2 + f^2} + \frac{Bf^2}{f_T} \right) (1 - 6.54 \times 10^{-4} P) \quad (6.6)$$

where

$$A = 2.34 \times 10^{-6}, B = 3.38 \times 10^{-6}, f_T = 21.9 \times 10^6 \left(\frac{1520}{T+273} \right).$$

At a nominal depth of 10 m, the hydrostatic pressure P is approximately 2×10^5 Pa (i.e. 2 kg/cm²). Based on the attenuation coefficient, a loss factor (in pressure

amplitude) can be computed to account for the absorption at distance D along an eigenray. We have

$$\begin{aligned}
L_A(D) &= 10^{-\left(\frac{D}{1000}\beta\right)/20} = \exp\left[-\frac{D}{20000}\beta\log_e 10\right] \\
&= \exp\left[-\frac{\log_e 10}{20000}D \cdot 8669\left(\frac{SAf_T f^2}{f_T^2 + f^2} + \frac{Bf^2}{f_T}\right)\right] \\
&= \exp\left[-0.998D\left(\frac{SAf_T f^2}{f_T^2 + f^2} + \frac{Bf^2}{f_T}\right)\right].
\end{aligned} \tag{6.7}$$

The attenuation coefficient does not change significantly with small changes in depth. As the depth is constrained in a very shallow water channel, we may use this expression in WSWA channels without significant loss in accuracy.

6.1.5. Reflection at the Sea Surface

The impedance mismatch between the sea water and air causes the sea surface to be a very good reflector. If the sea surface is calm, the reflection is close to perfect but includes a phase shift by π radians i.e. the reflection coefficient is -1 [59]. If the sea surface is rough (due to waves), a small loss will be incurred for every surface interaction. We model this loss by allowing a constant loss factor of L_{SR} per surface interaction.

6.1.6. Reflection at the Sea Bottom

The impedance mismatch between the sea water and seabed causes the sea bottom to reflect some of the sound incident on it. Let ρ and c be the density and sound speed in sea water respectively. Let ρ_1 and c_1 be the density and sound speed in the seabed respectively. For a smooth sea bottom, the reflection is angle dependent and is given by the Rayleigh reflection coefficient [59] as

$$L_B(\theta) = \left| \frac{m \cos \theta - \sqrt{n^2 - \sin^2 \theta}}{m \cos \theta + \sqrt{n^2 - \sin^2 \theta}} \right| \tag{6.8}$$

where

$$m = \frac{\rho_1}{\rho}, n = \frac{c}{c_1}.$$

The angle of incidence θ can be computed based on the geometry of the Pekeris waveguide. Let angle θ_{sb} correspond to an eigenray D_{sb} and angle $\underline{\theta}_{sb}$ correspond to an eigenray \underline{D}_{sb} . Then, we have

$$\begin{aligned}\theta_{sb} &= \tan^{-1} \left(\frac{R}{2bh + d_1 - (-1)^{s-b} d_2} \right) \\ \underline{\theta}_{sb} &= \tan^{-1} \left(\frac{R}{2bh - d_1 + (-1)^{b-s} d_2} \right).\end{aligned}\tag{6.9}$$

For a rough or absorbing sea bottom, additional reflection losses may be incurred. We model these losses by allowing an additional constant loss factor of L_{BR} per bottom interaction.

6.2. Channel Measurements

Although it is known that the medium range shallow water channel is dominated by time-varying multipath, very few measurements of the variability of the multipath structure are available. To help determine a statistical model for the time-variation of the WSWA channel, we measured the channel experimentally [5].

6.2.1. Experimental Setup

The channel measurements were conducted in February 2004 in Singapore waters near Selat Pauh ($1^\circ 13.35'$ N $103^\circ 44.60'$ E). The chosen location allowed measurements up to 1 km range in a relatively flat area with an average depth of about 15 m. Transmissions were made from an omni-directional transducer located at the bottom of a 4 m pole mounted on the bow of a research vessel. The signal was received using a hydrophone located at the bottom of a 4 m pole mounted on the side

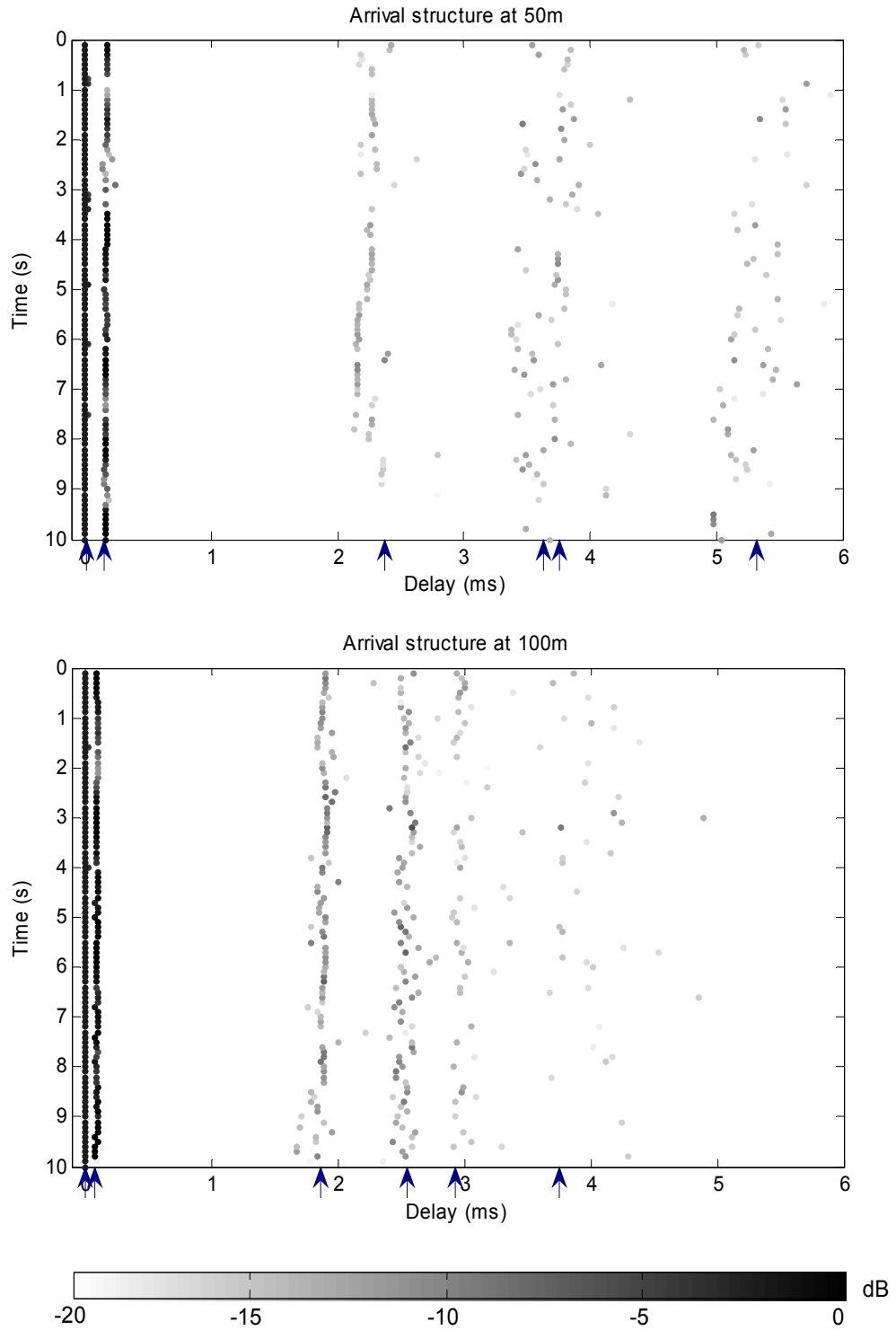
of an anchored barge. The signal was sampled at 250 kSa/s and stored for later analysis. The research vessel moved to various locations and made transmissions. GPS coordinates of the vessel and the barge were noted for range computation.

The signal used was a 30 ms direct sequence spread spectrum BPSK signal with a bandwidth of 40 kHz centered around 40 kHz. The signal was repeated 100 times at a rate of 10 Hz at each location of the research vessel. The different transmission locations corresponded to ranges of 50 m, 100 m, 550 m, 780 m and 1020 m. The measurements were made in relatively calm weather over a period of an hour.

The recorded signals were post-processed using the sign correlator to obtain estimates of the time-variability of the multi-path structure of the channel. The fading behavior of the signal was determined using the ML estimator. The SoS distribution assumed for the ML estimator was calibrated using ambient noise samples recorded at the experimental site.

6.2.2. Short Range Results

Figure 6.3 shows the time variability of the multi-path structure over 100 transmissions at short range (50 m and 100 m). The transmission time is shown on the y -axis, the delay on the x -axis and the darkness of each point represents the arrival strength. A ray model explained the observed data quite accurately. The direct arrival, surface reflected arrival and the bottom reflected arrival could be clearly distinguished. The arrival timings matched those predicted by the physics based model.



Each circular marker represents an estimated arrival. The blue arrows mark the arrival times computed using the ray theory and the best estimates of range, water depth and transducer depths. At 50m nominal range, the parameters used were – range: 55m, water depth: 12.5m, transducer depths: 2.4m & 2.6m. At 100m nominal range, the parameters used were – range: 100m, water depth: 14.5m, transducer depths: 3m & 2m.

Figure 6.3. Multipath arrival structure for 100 signal transmissions at 50 m and 100 m range

At 50 m, the direct and surface reflected arrivals are seen clearly. The surface reflected arrival shows very little variability in arrival time. However, it occasionally fades. The direct arrival and surface reflection are closely followed by secondary reflections with much lower amplitudes and are subject to more fading. The bottom reflected arrival is seen at about 2.2 ms after the direct arrival. This arrival shows considerable variability in time and amplitude.

At 100 m, the surface reflected arrival is stable in arrival time and also more stable in amplitude. The bottom reflected arrival is seen at about 1.8 ms after the direct arrival. This is much more stable in time and amplitude and shows slow variation. The variation shows a wavy pattern, which may arise from the movement of the barge and the boat with respect to the bottom. The bottom-surface and surface-bottom reflections are clearly seen at about 2.5 ms after the direct arrival.

The fading behavior of the direct arrival was determined by estimating the signal strength of 100 s sections of the received signal using the ML estimator. Figure 6.4 shows the fading of a single path as compared to Rayleigh fading. The observed fading is similar, but slightly less severe than predicted by the Rayleigh distribution. Rayleigh fading usually occurs in a sum of a large number of multipaths. However, Rayleigh fading was observed on each individual eigenray during channel measurements. This may be due to micro-multipath as the eigenray is scattered by small inhomogeneities in the medium and other suspended scatterers [82].

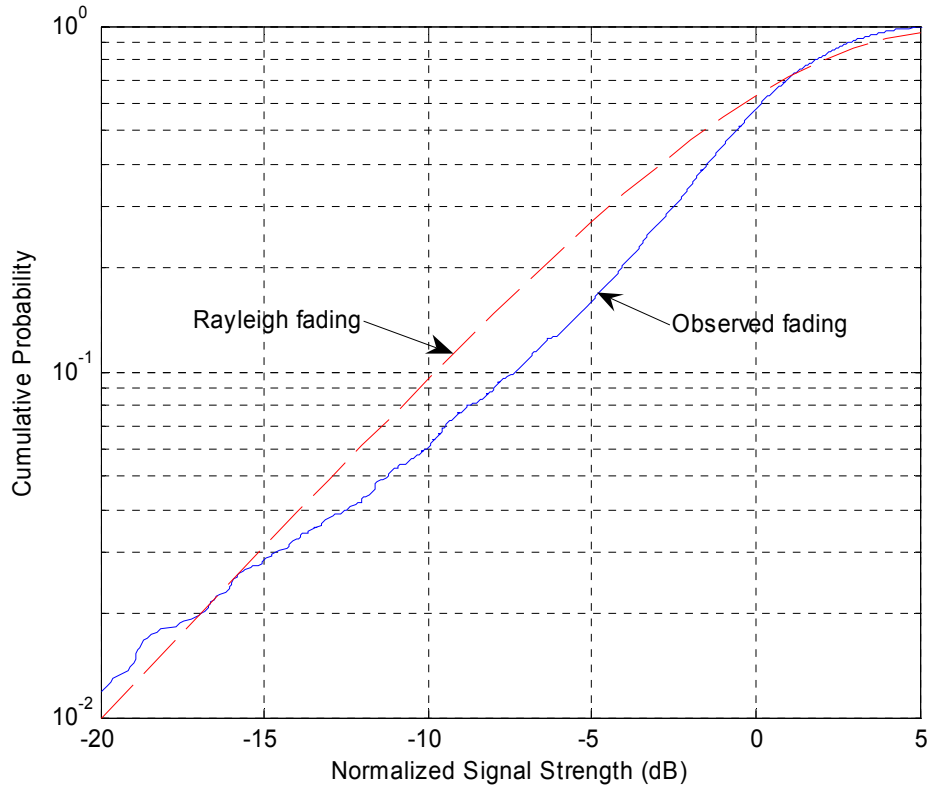


Figure 6.4. Cumulative distribution function of signal strength showing fading behavior of direct arrival at 50 m

6.2.3. Medium Range Results

The direct and surface reflected arrivals could not be independently resolved at medium range (550 to 1020 m). The interference of the two arrivals led to a Lloyds' mirror effect causing a transmission loss increase as the 4th power of range [58]. However, the combined arrival could still be detected at 1020 m and the combined fading behavior could be analyzed. The fading behavior of the combined arrival was determined by estimating the signal strength of 100 s sections of the received signal using the ML estimator as before. A cumulative distribution plot of the fading is shown in Figure 6.5. The combined arrival exhibits much deeper fading than predicted by the Rayleigh distribution.

As the combined arrival is formed by the interference of the direct and surface reflected arrival, one would expect that the fading could be explained as a function of the fading of each of the arrival. From short range measurements, we know that the direct arrival and surface reflected arrival are approximately Rayleigh distributed. As the time difference between the arrivals is small as compared to the reciprocal of the center frequency of the signal, we may assume that the two arrivals interfere destructively as the surface reflection coefficient is -1. The resulting first arrival would then be distributed as the difference of two independent Rayleigh random variables.

We simulated the above model by subtracting two sets of 5,000 Rayleigh distributed random numbers and plotting the cumulative distribution function of the resulting magnitude. The simulation yielded an expected fading as shown in Figure 6.5. The remarkable similarity in the simulated fading and the observed fading, suggests that the simple model suggested above is a good approximation. A ray model with individual rays exhibiting independent Rayleigh fading explains the short and medium range data well.

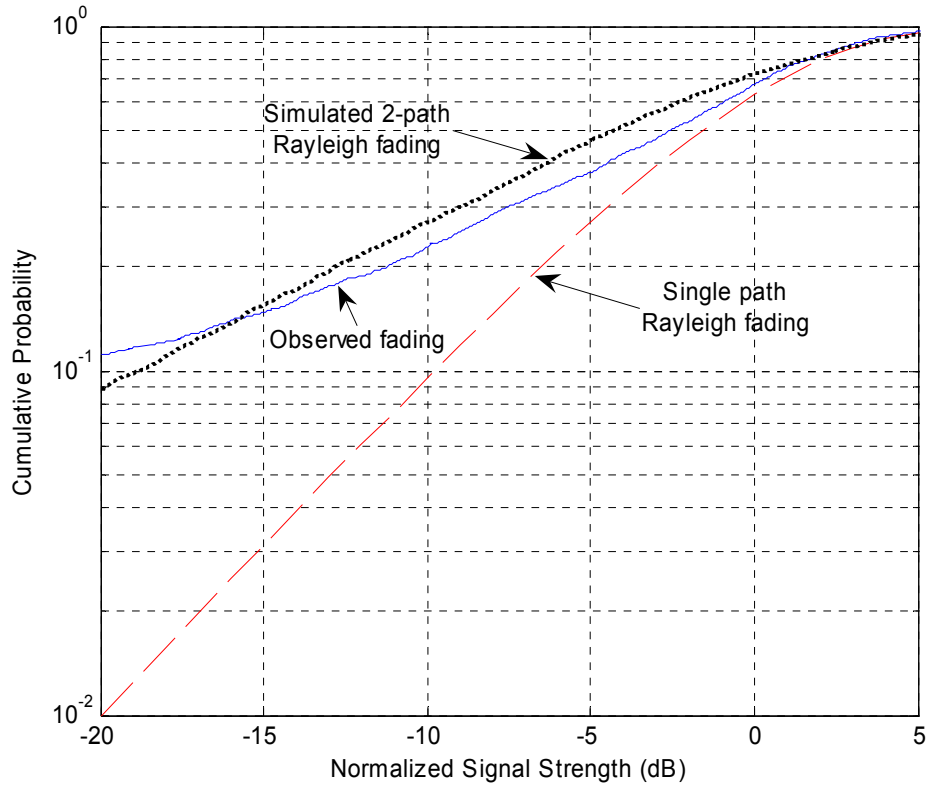


Figure 6.5. Cumulative distribution function of signal strength showing fading behavior of the combined arrival at 1020 m, compared against Rayleigh fading and simulated 2-path Rayleigh fading

6.2.4. Doppler Shift

As we do not consider fast moving communication nodes in this research, we do not expect any significant Doppler shift. The channel measurements showed no measurable Doppler shift in agreement with this assumption.

6.2.5. Doppler Spread & Coherence Time

Time-variation of the channel leads to broadening of narrowband signals in a channel. This phenomenon is known as Doppler spread [83]. Doppler spread in the channel was measured by transmitting a long sinusoidal signal and measuring the bandwidth of the received signal. Doppler spread estimates between 5-10 Hz were obtained in most configurations.

The Doppler spread is related to the coherence time of the channel. An estimate of the coherence time τ_c can be obtained based on the Doppler spread W_d [83],

$$\tau_c = \frac{0.423}{W_d}. \quad (6.10)$$

For a typical Doppler spread of 5-10 Hz, this leads to a channel coherence time of roughly 40-80 ms.

6.3. Time-varying Channel

The physics based model described in Section 6.1 yields a static model of the channel. However, the WSWA channel is a time-varying channel. To model the time variation, we introduce some statistical variations in the propagation model.

6.3.1. Ray Fading

Based on our experimental findings [5], we model the eigenray amplitude as a Rayleigh random process with a median determined by the physics based model and a time-correlation determined by the Doppler spread W_d . This leads to a statistical tapped delay line model which is a special case of the model proposed in [20], where the tap variation is modeled using Ricean statistics.

6.3.2. Arrival Time Lag Jitter

The arrival time lag of each eigenray with respect to the direct arrival is related to the difference in path length along the eigenray and the direct path. However, the arrival time lag exhibits variation over time, probably due to movement of the source, receiver and the surface. The stability of the arrival time lag with respect to small changes in source/receiver position can be analyzed using a ray model. Let τ_{sb} be the arrival time lag of eigenray D_{sb} and $\underline{\tau}_{sb}$ be the arrival time lag of eigenray \underline{D}_{sb} . We have

$$\begin{aligned}\tau_{sb} &= \frac{D_{sb} - D_{00}}{c} \\ \underline{\tau}_{sb} &= \frac{\underline{D}_{sb} - D_{00}}{c}.\end{aligned}\tag{6.11}$$

Substituting (6.1), (6.2) and (6.3) in the above, we have

$$\begin{aligned}\tau_{sb} &= \frac{1}{c} \left[\sqrt{R^2 + [2bh + d_1 - (-1)^{s-b} d_2]^2} - \sqrt{R^2 + (d_1 - d_2)^2} \right] \\ \underline{\tau}_{sb} &= \frac{1}{c} \left[\sqrt{R^2 + [2bh - d_1 + (-1)^{b-s} d_2]^2} - \sqrt{R^2 + (d_1 - d_2)^2} \right].\end{aligned}\tag{6.12}$$

As we are interested in medium range communications in shallow waters, we assume $R \gg d_1$, $R \gg d_2$ and $R \gg h$. Using the Taylor series expansion

$\sqrt{1+x} \approx 1 + \frac{1}{2}x$ if $|x| \ll 1$, we have

$$\begin{aligned}\tau_{sb} &= \frac{R}{c} \left[\sqrt{1 + \left[\frac{2bh + d_1 - (-1)^{s-b} d_2}{R} \right]^2} - \sqrt{1 + \left(\frac{d_1 - d_2}{R} \right)^2} \right] \\ &\approx \frac{R}{c} \left[1 + \frac{1}{2} \left[\frac{2bh + d_1 - (-1)^{s-b} d_2}{R} \right]^2 - 1 - \frac{1}{2} \left(\frac{d_1 - d_2}{R} \right)^2 \right] \\ &= \frac{1}{2Rc} \left[(2bh + d_1 - (-1)^{s-b} d_2)^2 - (d_1 - d_2)^2 \right] \\ &= \frac{2}{Rc} \left[b^2 h^2 + bhd_1 - (-1)^{s-b} bhd_2 + (s-b)d_1 d_2 \right]\end{aligned}\tag{6.13}$$

Similarly,

$$\underline{\tau}_{sb} \approx \frac{2}{Rc} \left[b^2 h^2 - bhd_1 + (-1)^{b-s} bhd_2 + (b-s)d_1 d_2 \right].$$

To test the stability of arrival time lag, we differentiate the above with respect to the source depth d_1 , receiver depth d_2 and range R to obtain

$$\frac{\partial \tau_{sb}}{\partial R} = \frac{\partial \underline{\tau}_{sb}}{\partial R} \approx 0\tag{6.14}$$

i.e. the arrival time jitter is, to first order, independent of the range, and

$$\begin{aligned}
\frac{\partial \tau_{sb}}{\partial d_1} &= \frac{2bh}{Rc} + (s-b) \frac{2d_2}{Rc} \\
\frac{\partial \tau_{sb}}{\partial d_2} &= -(-1)^{s-b} \frac{2bh}{Rc} + (s-b) \frac{2d_1}{Rc} \\
\frac{\partial \tau_{sb}}{\partial d_1} &= -\frac{2bh}{Rc} + (b-s) \frac{2d_2}{Rc} \\
\frac{\partial \tau_{sb}}{\partial d_2} &= (-1)^{b-s} \frac{2bh}{Rc} + (b-s) \frac{2d_1}{Rc}.
\end{aligned} \tag{6.15}$$

Using Δ as a small change operator, we can write the change in arrival time lag as a function of the change of the source depth, receiver depth and range as

$$\begin{aligned}
\Delta \tau_{sb} &= \frac{\partial \tau_{sb}}{\partial R} \Delta R + \frac{\partial \tau_{sb}}{\partial d_1} \Delta d_1 + \frac{\partial \tau_{sb}}{\partial d_2} \Delta d_2 \\
\Delta \tau_{sb} &= \frac{\partial \tau_{sb}}{\partial R} \Delta R + \frac{\partial \tau_{sb}}{\partial d_1} \Delta d_1 + \frac{\partial \tau_{sb}}{\partial d_2} \Delta d_2.
\end{aligned} \tag{6.16}$$

As the derivatives with respect to R are 0, the arrival time lags are not sensitive to small changes in range. If we model Δd_1 and Δd_2 as Gaussian random variables with variance σ_d^2 , we can estimate the variance of the arrival time lags as

$$\begin{aligned}
\sigma_{sb}^2 &= \sigma^2(\tau_{sb}) = \left| \frac{\partial \tau_{sb}}{\partial d_1} \right|^2 \sigma_d^2 + \left| \frac{\partial \tau_{sb}}{\partial d_2} \right|^2 \sigma_d^2 \\
&= \frac{4\sigma_d^2}{R^2 c^2} [2b^2 h^2 + (s-b)(d_1^2 + d_2^2 + 2bhd_1 + 2bhd_2)]
\end{aligned} \tag{6.17}$$

Similarly,

$$\sigma_{sb}^2 = \sigma^2(\tau_{sb}) = \frac{4\sigma_d^2}{R^2 c^2} [2b^2 h^2 + (b-s)(d_1^2 + d_2^2 - 2bhd_1 - 2bhd_2)].$$

From this expression, we would expect that we have less arrival time lag jitter at further ranges than nearer ranges. We would also expect that the arrival time lag jitter would increase as the number of surface and bottom interactions of the eigenray increases. Both these observations are consistent with observations made during the channel measurement experiment described in the previous section.

6.4. The Channel Model

In Sections 6.1 and 6.3 we have developed the components of a time-varying channel propagation model. We now put the components together into a ray theory based channel model.

Let $x(t)$ be a signal transmitted through the channel and $y(t)$ be the corresponding received signal. Ignoring the absolute time delay between transmission and reception, we can express $y(t)$ in terms of $x(t)$ as

$$\begin{aligned}
 y(t) &= A_{00}(t)L_{SS}(D_{00})L_A(D_{00})x(t) \\
 &+ \sum_{s=1}^{\infty} \sum_{b=s-1}^s A_{sb}(t)L_{SS}(D_{sb})L_A(D_{sb})(-L_{SR})^s L_{BR}^b L_B(\theta_{sb})^b x(t - \tau_{sb} + J_{sb}(t)) \\
 &+ \sum_{b=1}^{\infty} \sum_{s=b-1}^b \underline{A}_{sb}(t)L_{SS}(\underline{D}_{sb})L_A(\underline{D}_{sb})(-L_{SR})^s L_{BR}^b L_B(\underline{\theta}_{sb})^b x(t - \underline{\tau}_{sb} + \underline{J}_{sb}(t)) \\
 &+ n(t) \\
 \therefore y(t) &= \frac{A_{00}(t)L_A(D_{00})}{D_{00}}x(t) \\
 &+ \sum_{s=1}^{\infty} \sum_{b=s-1}^s \frac{A_{sb}(t)L_A(D_{sb})(-L_{SR})^s L_{BR}^b L_B(\theta_{sb})^b}{D_{sb}}x(t - \tau_{sb} + J_{sb}(t)) \quad (6.18) \\
 &+ \sum_{b=1}^{\infty} \sum_{s=b-1}^b \frac{\underline{A}_{sb}(t)L_A(\underline{D}_{sb})(-L_{SR})^s L_{BR}^b L_B(\underline{\theta}_{sb})^b}{\underline{D}_{sb}}x(t - \underline{\tau}_{sb} + \underline{J}_{sb}(t)) \\
 &+ n(t)
 \end{aligned}$$

where $A_{sb}(t)$ and $\underline{A}_{sb}(t)$ are modeled as independent Rayleigh processes with unit mean and an exponential autocorrelation specified by the Doppler spread W_d or channel coherence time τ_c . These processes represent the fading of individual eigenpaths. The quantities $J_{sb}(t)$ and $\underline{J}_{sb}(t)$ are random variables denoting the time jitter, modeled as Gaussian processes with zero mean, variance σ_{sb}^2 (given by (6.17)) and an exponential autocorrelation specified by a transducer position coherence time τ_d . The noise $n(t)$ is modeled as a S α S process as described in Chapter 3. We assume the noise to be white over the bandwidth of interest. This assumption is reasonable as

long as the signal bandwidth is not very large^{*}. The quantities L_{SS} , L_A , D_{sb} , \underline{D}_{sb} , L_B , θ_{sb} , $\underline{\theta}_{sb}$, τ_{sb} and $\underline{\tau}_{sb}$ are given by equations (6.1), (6.2), (6.3), (6.5), (6.7), (6.8), (6.9) and (6.13) respectively.

Although the summations in (6.18) have infinite number of terms, the terms diminish in magnitude and the summations converge. Only terms significantly larger than the ambient noise need to be included in practice. For most channels in practice, it is sufficient to include the first few terms in both summations.

The channel model in (6.18) should be interpreted as a passband channel model. The L_A terms in the model are frequency dependent. If the bandwidth of the signal $x(t)$ is much smaller than the carrier frequency F_c , the L_A terms can be computed at the carrier frequency. For broadband transmission at long distances, this approach yields lower accuracy. However, for simplicity in the analytical model, we use the L_A terms at frequency F_c irrespective of the bandwidth of the signal.

A baseband channel model can also be implemented based on (6.18) with some small changes. The L_A terms have to be computed at the appropriate carrier frequency. In addition, the real S α S ambient noise process $n(t)$ needs to be replaced with an isotropic complex S α S noise process [72] to accommodate the complex noise requirement at baseband.

This channel model can be interpreted as a tapped delay line with time-varying tap weights and tap delays. Equation (6.18) can be written in a simplified form with N significant terms, lumped coefficients B_j , delays τ_j , Rayleigh random processes $A_j(t)$, Gaussian random processes $J_j(t)$ and a S α S random process $n(t)$:

^{*} Due to limitations in efficient transducers for underwater transmission, typical acoustic communication systems are limited in usable bandwidth.

$$y(t) = A_0(t)B_0x(t) + \sum_{j=1}^{N-1} A_j(t)B_jx(t - \tau_j + J_j(t)) + n(t) \quad (6.19)$$

An implementation of this channel has been developed in MATLAB and is included as part of the communications simulation software developed in this research. The random noise process $n(t)$ is simulated using the method described in [76].

6.5. Comparison with Experimental Data

To validate the model, we compared the measured multipath structure in the channel over 100 transmissions against simulation results. Figure 6.6 shows a comparison between experiment and simulation in a 15 m deep channel at a range of 100 m. Although similar validations were successfully performed at longer ranges (up to 1 km), we present the results at 100 m due to the high SNR at this range. This enabled us to study the similarities and differences between the experimental measurements and simulation in more detail than at greater ranges.

The simulation parameters were chosen based on our knowledge of the experimental scenario. Some channel parameters were adjusted slightly to obtain a close match between measurement and simulation. The parameter values used in the simulation are listed in Table 6.1.

Both, experimental and simulated arrival structures show 5 arrivals. The first arrival is the direct arrival, closely followed by the surface reflected arrival and then the bottom reflected arrival. The next 3 arrivals are a result of multiple surface and bottom interactions. We note that the mean arrival timings (relative to the direct arrival) agree closely between the simulation and measurement, as shown in Table 6.2. The simulation also predicts the spread (standard deviation) of arrival time accurately. The measured data shows some correlation between the arrival times of

closely spaced iterations for some of the arrivals. This correlation is not captured in our simulation. However, it is not important if the transmission time between packets is large. The average measured and predicted arrival strengths (relative to the direct arrival) are quite close. The simulation predicts a little more fading than observed in the direct and surface reflected arrival. It also predicts a few stronger arrivals than those observed in the bottom reflected ray and higher order reflected rays.

Table 6.1. Simulation parameters

Parameter	Symbol	Value
Range	R	100 m
Water depth	h	14.5 m
Source depth	d_1	3 m
Receiver depth	d_2	2 m
Center frequency	F_c	40 kHz
Sampling frequency	F_s	500 kHz
Surface reflection loss	L_{SR}	3 dB
Bottom reflection loss	L_{BR}	10 dB
Water density	ρ	1023 kg/m ³
Seabed density	ρ_1	1500 kg/m ³
Seabed soundspeed	c_1	1650 m/s
Water temperature	T	27 °C
Salinity	S	35 ppt
Doppler spread	W_d	10 Hz
Ambient noise α	α	1.7
Ambient noise level (integrated over the frequency band of interest)	c	120,000 Pa
Transducer RMS movement	σ_d	0.25 m
Transducer position coherence time	τ_d	0.25 s
Number of reflection terms	N	3

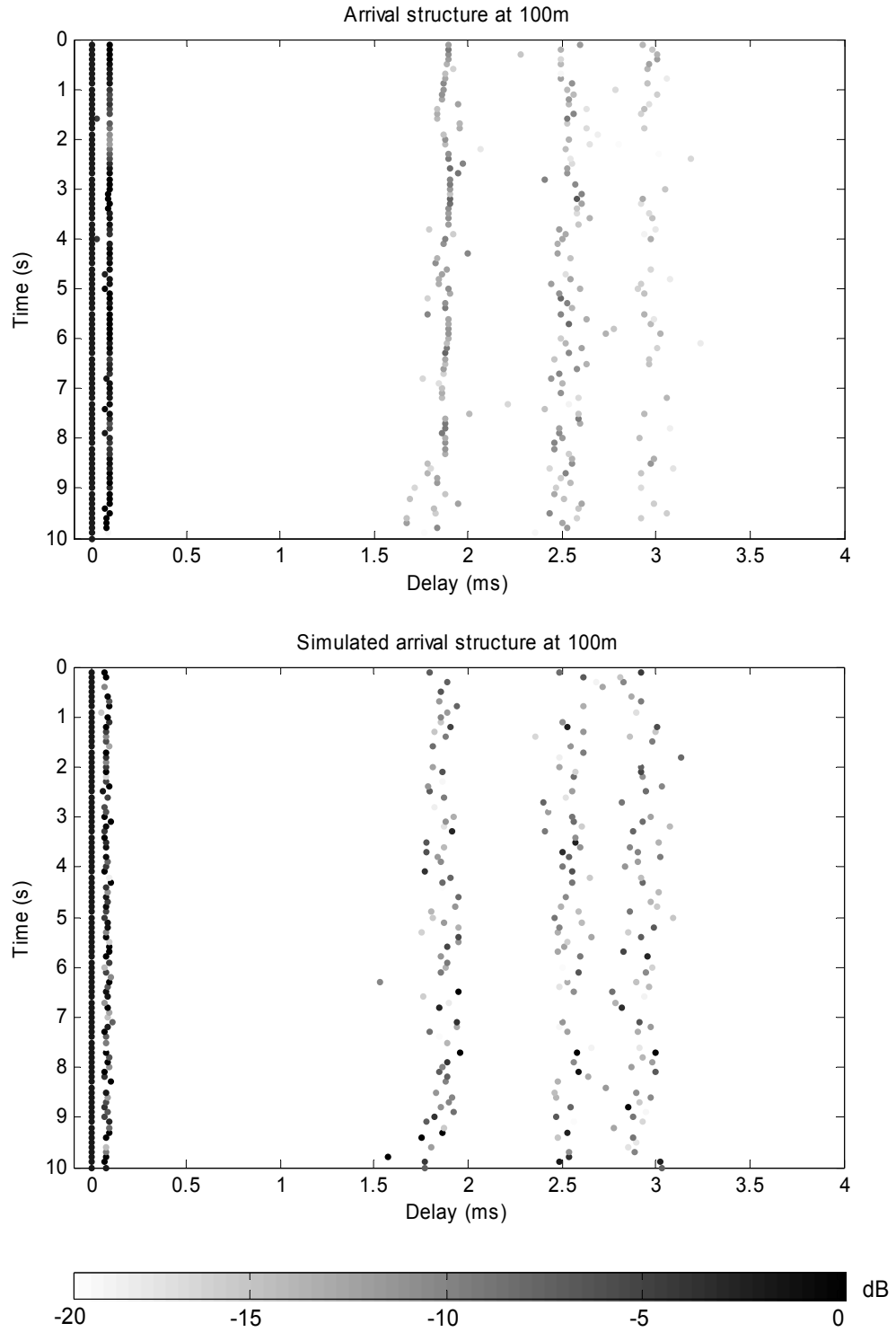


Figure 6.6. Comparison of multipath arrival structure between experiment and simulation

The slight mismatch in fading statistics between observation and simulation is a limitation of our model as we modeled all arrivals with similar fading statistics. Although a more comprehensive fading model could have been developed, we opted

to retain our simple fading model as the proposed channel model seemed to capture most of observed phenomenon in the channel.

Table 6.2. Comparison of simulated channel statistics against experimental channel statistics

		Simulation	Measurement
Arrival 2	Mean Arrival Timing	0.08 ms	0.09 ms
	Arrival Timing Spread	0.01 ms	0.01 ms
	Mean Relative Strength	0 dB	1 dB
Arrival 3	Mean Arrival Timing	1.9 ms	1.9 ms
	Arrival Timing Spread	0.08 ms	0.07 ms
	Mean Relative Strength	-7 dB	-8 dB
Arrival 4	Mean Arrival Timing	2.5 ms	2.5 ms
	Arrival Timing Spread	0.07 ms	0.07 ms
	Mean Relative Strength	-9 dB	-9 dB
Arrival 5	Mean Arrival Timing	2.9 ms	3.0 ms
	Arrival Timing Spread	0.07 ms	0.09 ms
	Mean Relative Strength	-9 dB	-11 dB

6.6. Conclusions

In this chapter, we developed a channel model for the WSWA channel. The model was derived from physics of ocean acoustics and statistical observations based on channel measurements. The model is able to explain most of the key features observed via channel measurements. The model is shown to be equivalent to a tapped delay line channel model which is common in communication systems. However, the tap weights and tap delays are modeled as time-varying random processes. The tap weights, delays and the random processes parameters are derived in terms of physically measurable parameters such as water temperature, salinity, communication range, water depth, coherence time, etc. The channel model also includes an S α S ambient noise term.

The channel model provides a basis for communication system design, performance analysis and simulation. An implementation of the WSWA channel model is available as part of a simulation tool developed in MATLAB. The channel model and implementation was tested successfully by comparing the simulation against experimental channel measurements.

7. *Proposed Communication Scheme*

In this chapter, we develop a communication scheme for use in WSWA channels. The scheme is inspired by the understanding of the channel and ambient noise developed in the previous chapters. We study the performance of the scheme via simulation.

7.1. *Communication Scheme*

7.1.1. Modulation Scheme

Incoherent digital communication techniques such as FSK are known to be robust but suffer from low bandwidth efficiency. Coherent modulation techniques such as PSK have high bandwidth efficiency, but require complex adaptive equalizers to cope with time-varying frequency-selective fading channels. The complexity of the equalizer is often a function of the channel delay spread in relation to the symbol period. As the WSWA channel exhibits delay spreads in the order of several milliseconds, equalizer complexity increases rapidly as we approach signaling rates of several tens of kbps. Spread spectrum techniques such as frequency hopping and DSSS are known to be effective in frequency-selective fading channels. However, spread spectrum techniques have low bandwidth utilization and therefore are not desirable in band-limited channels.

OFDM is a communication technique which divides the available bandwidth into several sub-carriers [26;84]. Each sub-carrier uses a narrow band (less than the coherence bandwidth of the channel) and hence experiences flat fading. This simplifies channel equalization. In addition, it increases the symbol length and consequently increases robustness to impulsive noise. Each sub-carrier in OFDM can

be modulated using any modulation scheme. We use OFDM with PSK modulation as the basis for our underwater communication scheme. As we shall show in subsequent sections, OFDM has many properties which are well suited to communications in the WSWA channel.

OFDM can be implemented efficiently using the inverse DFT (IDFT) and DFT to map a series of symbols onto carriers and vice-versa. Let N_c be the number of OFDM sub-carriers and S_{jm} be the PSK modulated symbols to be transmitted on carrier m during symbol j in OFDM symbol x_{jk} where k is the time index during symbol j . Then,

$$x_{jk} = IDFT\{S_{jm}\} = \sum_{m=0}^{N_c-1} S_{jm} F_{mk}^{-1} \quad \forall k \in [0, N_c - 1] \quad (7.1)$$

where $IDFT\{\dots\}$ denotes an IDFT operation and F_{mk}^{-1} denotes the IDFT matrix.

7.1.2. Cyclic Prefix

One of the popular ways to avoid ISI due to multipath arrivals in an OFDM scheme is to introduce a guard interval between adjacent OFDM symbols. If the guard interval is larger than the delay spread of the channel, ISI is completely eliminated and the equalization becomes trivial. The guard interval is usually introduced in the form of a symbol prefix. However, a zero-filled symbol prefix destroys the orthogonality of the sub-carriers in the OFDM symbol. A cyclic prefix, on the other hand, maintains orthogonality while eliminating ISI [26]. Although OFDM schemes based on zero-padding can be developed [85], we use the cyclic prefix in our implementation.

If we introduce a cyclic prefix of length N_p , the actual symbol transmitted is

$$\tilde{x}_{jk} = \begin{cases} x_{j, N_c - N_p + k} & \forall k \in [0, N_p - 1] \\ x_{j, k - N_p} & \forall k \in [N_p, N_p + N_c - 1] \end{cases} \quad (7.2)$$

On reception, the cyclic prefix is simply removed before demodulation of the OFDM symbols.

The use of cyclic prefix reduces the effective signaling rate due to the guard interval before every OFDM symbol. However, the benefit gained in terms of simplified equalization is often sufficient justification to accept the reduced data rate.

7.1.3. Differential Sub-carrier Modulation

The use of OFDM with cyclic prefix simplifies the equalizer for each sub-carrier to a single tap complex multiplication provided that the sub-carrier bandwidth is smaller than the channel coherence bandwidth and that the cyclic prefix length is more than the delay spread of the channel [26].

If \underline{x}_{jk} is the received OFDM symbol, $DFT\{\dots\}$ denotes a DFT operation and F^{km} denotes the DFT matrix, the demodulation operation can be written as

$$\underline{S}_{jm} = DFT\{\underline{x}_{jk}\} = \sum_{k=0}^{N_c-1} \underline{x}_{jk} F_{km} \quad \forall m \in [0, N_c - 1]. \quad (7.3)$$

Noisy estimates of transmitted symbols \underline{S}_{jm} are obtained by a single-tap equalizer,

$$\underline{S}_{jm} = C_{jm} \underline{S}_{jm} \quad (7.4)$$

where C_{jm} are the equalizer tap coefficients of carrier m during symbol j . This can be equivalently written in terms of the transmitted symbols S_{jm} and a noise term n_{jm} as

$$\begin{aligned} \underline{S}_{jm} &= S_{jm} + n_{jm} \\ \text{or} \\ \underline{S}_{jm} &= C_{jm}^{-1} S_{jm} + C_{jm}^{-1} n_{jm}. \end{aligned} \quad (7.5)$$

The equalizer tap coefficients C_{jm} can be tracked over time using known pilots transmitted along with the data. However, differential modulation can remove the need to track equalizer tap coefficients and pilots provided the OFDM symbol period

is much smaller than the channel coherence time. Let D_{jm} be the data symbols to be transmitted. We transmit symbols S_{jm} instead, such that

$$\begin{aligned} S_{jm} &= S_{j-1,m} D_{jm} \\ S_{0m} &= 1. \end{aligned} \quad (7.6)$$

The equivalent received symbols are now

$$\underline{S}_{jm} = C_{jm}^{-1} S_{jm} + C_{jm}^{-1} n_{jm}. \quad (7.7)$$

Now, we compute noisy estimates \underline{D}_{jm} as

$$\underline{D}_{jm} = \frac{\underline{S}_{jm}}{\underline{S}_{j-1,m}} = \frac{C_{jm}^{-1} S_{jm} + C_{jm}^{-1} n_{jm}}{C_{j-1,m}^{-1} S_{j-1,m} + C_{j-1,m}^{-1} n_{j-1,m}}. \quad (7.8)$$

If the symbol period is much smaller than the channel coherence time,

$$\begin{aligned} C_{jm}^{-1} &\approx C_{j-1,m}^{-1} \\ \therefore \underline{D}_{jm} &= \frac{C_{jm}^{-1} S_{jm} + C_{jm}^{-1} n_{jm}}{C_{j-1,m}^{-1} S_{j-1,m} + C_{j-1,m}^{-1} n_{j-1,m}} \\ &= \frac{S_{jm} + n_{jm}}{S_{j-1,m} + n_{j-1,m}} \\ &= (S_{jm} + n_{jm}) \frac{1}{S_{j-1,m}} \left(1 + \frac{n_{j-1,m}}{S_{j-1,m}} \right)^{-1} \\ &= \left(\frac{S_{jm}}{S_{j-1,m}} + \frac{n_{jm}}{S_{j-1,m}} \right) \left(1 - \frac{n_{j-1,m}}{S_{j-1,m}} + \text{higher order terms} \right) \\ &= D_{jm} + \text{other terms.} \end{aligned} \quad (7.9)$$

Hence, with differential modulation, the transmitted signal can be derived from the received signal without the need to track the channel. The cost of this simplification is in terms of the additional noise terms in (7.9). The BER for differential PSK has been known to be twice that of fully coherent PSK [83].

The symbols D_{jm} are obtained from the bits d_{jm} to be transmitted based on the PSK modulation order. For BPSK, the mapping is trivial (e.g. $d_{jm} = 0 \rightarrow D_{jm} = -1$, d_{jm}

$= 1 \rightarrow D_{jm} = 1$). For QPSK and higher modulation orders, the mapping should use Gray codes for optimum error performance [83].

7.1.4. Coding

Coding allows us to introduce redundancy in the transmitted data in order to improve the robustness of the communication. Although several coding techniques have been studied in literature, we adopt convolutional coding in our communication scheme [77]. This decision is motivated by the fact that convolutional codes are simple to implement and we have explored decoding of convolutional codes in S α S noise in Chapter 5. The proposed communication scheme, however, does not depend on the detailed structure of convolutional codes. Hence the coding scheme may be easily changed at a later point in time without significant impact on the analysis presented here.

A rate R_c convolutional code with a constraint length L_c spreads the energy from each bit to be transmitted over L_c coded bits. This increased redundancy improves the robustness of the scheme. The effective data rate of the communication link is reduced by a factor R_c in exchange for this higher robustness.

The coding is implemented using a standard convolutional encoder [77]. The received data is decoded using the Viterbi decoder with the 1-norm branch metric developed in Chapter 5.

7.1.5. Channel Interleaver

Convolutional coding spreads the bit energy over L_c consecutive coded bits. These bits are usually encoded as symbols and transmitted over consecutive sub-carriers over a short period of time. In the WSWA channel, we expect the noise to be impulsive. Impulses are short in time and hence have a wide bandwidth. When noise impulses occur, they affect all sub-carriers simultaneously. Moreover, for QPSK

symbols, the noise on the in-phase and quadrature channels is correlated (Theorem 7). Hence most of the energy from the L_c coded bits is likely to be affected by the noise and severely affect decoding performance. Sending the L_c coded bits over a single sub-carrier over a longer time does not solve the problem. If a sub-carrier fades, it will affect the symbols transmitted over the sub-carrier over the coherence time of the channel. If the L_c coded bits are transmitted over this time, many of the bits are likely to get affected simultaneously, affecting decoding performance.

A random block interleaver can be used to spread the coded bits in a pseudo-random pattern across a block. When the block is transmitted using OFDM, the L_c coded bits are spread randomly in time and frequency and are unlikely to be affected by impulse noise or sub-carrier fades at the same time. Hence the errors become uncorrelated over the constraint length of the code and the decoding performance becomes close to optimal. We effectively utilize the time and frequency diversity available across the OFDM sub-carriers through the use of interleaved coding.

7.1.6. Frame Synchronization

For transmission, the data is organized into packets or frames. Each frame is encoded with a known start and final encoder state, zero padded to become an integral multiple of the number of bits per OFDM symbol and interleaved with a block interleaver. The resultant data is modulated on OFDM sub-carriers, up-converted and transmitted. A short pseudo-noise sequence with the same center frequency and bandwidth as the modulated signal is sent as a frame preamble so that the receiver can identify the start of each frame. The pseudo-noise sequence is generated by BPSK modulating a carrier frequency with a long m-sequence.

7.1.7. Symbol Synchronization

Several OFDM synchronization methods have been discussed in the literature [86-88]. In [86], the authors use the correlation between the cyclic prefix and the symbol to achieve symbol synchronization. Although the method in this paper is not directly usable due to their Gaussian noise assumption, we develop a symbol synchronization method based on this idea without using the normalization term which requires the Gaussian noise assumption. The method is outlined below.

We compute a statistic based on the correlation between the received data and a time-lagged (by N_c) version of the received data. The statistic is averaged over a window of length equal to the cyclic prefix and scaled by the average energy in the window. Let $x(t)$ represent the received data and $\Lambda(t)$ represent the statistic. Then,

$$\Lambda(t - N_c) = \left| \frac{\sum_{\tau=t-N_p+1}^t x(\tau) \bar{x}(\tau - N_c)}{\sum_{\tau=t-N_p+1}^t x(\tau) \bar{x}(\tau)} \right| \quad (7.10)$$

where \bar{x} represents the complex conjugate of x .

As the correlation between the cyclic prefix and the end of the symbol is high, peaks appear in the time series of the statistic every time it encounters a cyclic prefix. A sample time series of the statistic Λ (for an OFDM signal with 512 carriers and a cyclic prefix of 32 samples) is shown in Figure 7.1. Statistic Λ has a peak at the start time of each symbol (every 22.3 ms in this example).

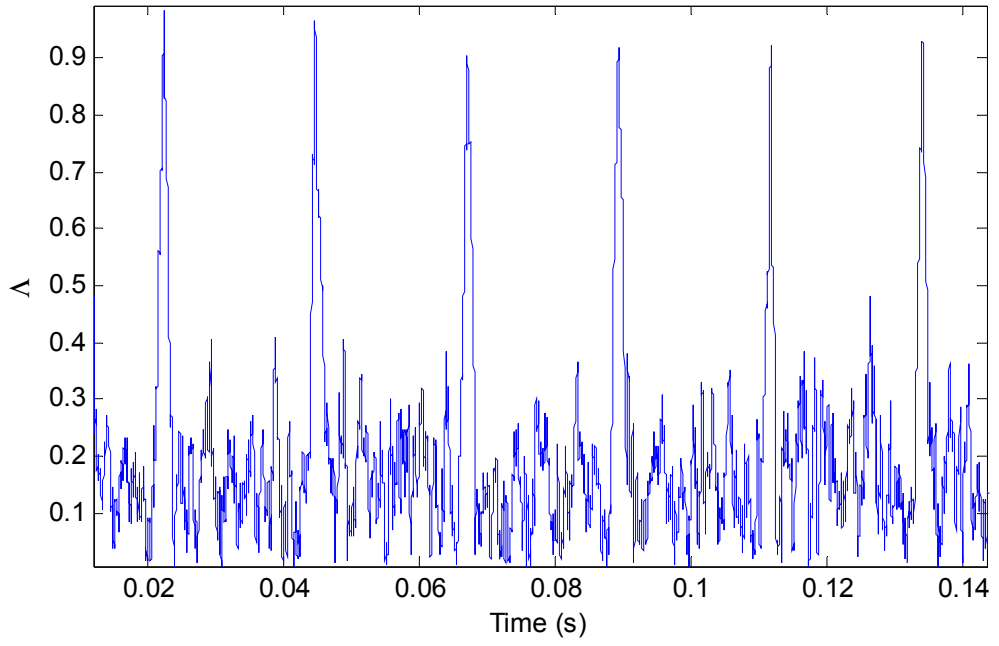


Figure 7.1. Statistic Λ shows a peak at the start of each OFDM symbol

The symbol timing estimation algorithm can be summarized as follows:

1. Start with an initial known position t_0 for the first symbol
2. Initialize $j = 0$
3. Increment j
4. Estimate the a-priori next symbol start, $t'_j = t_{j-1} + N_c + N_p$
5. Compute Λ over the local neighborhood of t'_j
6. Find position t''_j of maximum Λ over the local neighborhood of t'_j
7. Go to step 3

The output time series t''_j generated by the above algorithm is then passed through a low pass filter to yield final estimates t_j . The low pass filter helps reduce the noise in the estimate based on the knowledge that the symbol timings change slowly (primarily due to the movement of the transducers). The bandwidth of the low pass filter is chosen based on the coherence time of transducer position. The algorithm is executed on a fractionally sampled received data to achieve higher timing resolution.

7.1.8. Carrier Synchronization

A significant carrier frequency offset causes inter-carrier interference in OFDM, adversely affecting communication performance. Carrier synchronization has therefore been an area of interest among OFDM researchers [86-88].

In underwater communications, the carrier frequencies used are very low (in kHz). Hence, it is possible to sample the signal in passband and perform down-shifting and demodulation digitally. Data acquisition systems at these low frequencies have stable sampling clocks and do not result in significant carrier offset. Moreover, any small carrier offset appears as a slowly rotating equalizer tap coefficient and is automatically compensated for by the differential modulation. We, therefore, do not require any algorithm specifically for carrier synchronization.

7.1.9. Peak-to-Average Power Ratio

A common problem in OFDM communication is that the peak-to-average power ratio (PAPR) of OFDM signals is usually very high. This affects the maximum average source level that can be attained via power amplifiers and transducers with limited dynamic range. Techniques are available in the literature to reduce the PAPR of OFDM signals [89;90].

Although our signals suffer from high PAPR (usually about 5), it is not a severe limitation at the transmission range of interest as the required source power level can be achieved by power amplifiers with sufficient dynamic range. Hence we do not apply any PAPR reduction techniques to our signals. Techniques from [89;90] may be applied during communications at longer ranges, where a lower PAPR is important.

7.1.10. Proposed Scheme

The communication scheme proposed in the past few sections is summarized in the block diagram shown in Figure 7.2.

The data to be transmitted is first encoded using a convolutional code, zero padded to an integral multiple of number of bits per OFDM symbol and then interleaved with a random block interleaver, henceforth known as the channel interleaver. It is then mapped to the appropriate PSK constellation using Gray coding. The data is then converted from serial to parallel by the S2P block. It is then differentially encoded by the Δ block, OFDM modulated by the IFFT and converted back to serial by the P2S block. A cyclic prefix is then added by the CP insertion block. Finally, a pseudo-noise preamble is added, the data is up-sampled, up-converted to the carrier frequency and transmitted.

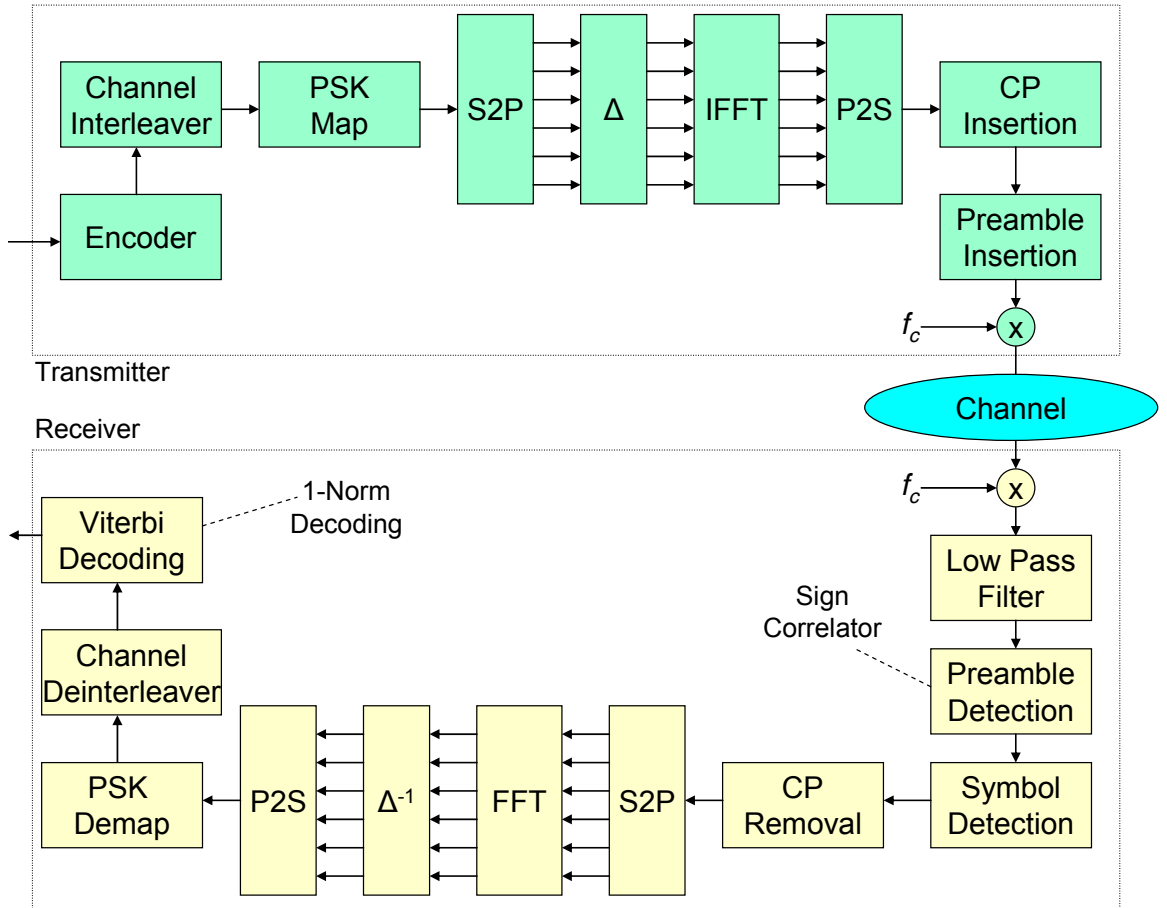


Figure 7.2. Overview of proposed OFDM communication scheme

The received data is first down-converted, filtered and down-sampled. The preamble detection block uses the sign correlator to find the start of a frame. The

symbol detection block then finds the start of each symbol. The CP removal block removes the cyclic prefix. The S2P and the FFT blocks then perform OFDM demodulation. This is followed by a differential decoding process in the Δ^{-1} block and a conversion back to serial by the P2S block. The resulting data stream is de-mapped, de-interleaved and then decoded using a Viterbi decoder. The Viterbi decoder with a 1-norm branch metric is the recommended method for decoding. However, we also present the results from hard-decision decoding and soft-decision Viterbi decoding using the conventional Euclidean norm in our simulation results and experimental analysis for comparison. The output of this decoder is the received data.

7.2. Selection of Parameters

7.2.1. Frequency Band

The bandwidth available for underwater communication is typically limited by the transmission characteristics of the transducer. Energy efficient transducers usually operate near the resonant frequency and are therefore limited to few tens of kHz of usable bandwidth. In our simulations and experiments, we assume a bandwidth availability of about 25 kHz.

The usage of the acoustic spectrum in the ocean is not regulated. However, natural characteristics of the channel and transducers limit the usable frequency band. Low frequencies are dominated by ambient noise [6]. High frequencies are attenuated by relaxation processes in sea water [59]. The optimal choice of center frequency is achieved by maximizing the SNR given the ambient noise curves and frequency dependent attenuation. If $N_A(f)$ is the ambient noise PSD at frequency f and $L_A(D, f)$ is the attenuation loss factor given by (6.7), then SNR can be maximized by maximizing the ratio L_A/N_A as a function of f at a given transmission range D .

Figure 7.3 shows a plot of L_A/N_A as a function of f at a water temperature of 27 C and typical ambient noise PSD (based on recording in Singapore waters) for various transmission ranges of interest. We can see that the maximum SNR is achieved between 42-60 kHz at a range of 500 m and between 40-55 kHz at a range of 1000 to 1500 m. A frequency band of 25 kHz centered at 50 kHz is therefore well suited for communications at 500-1500 m range.

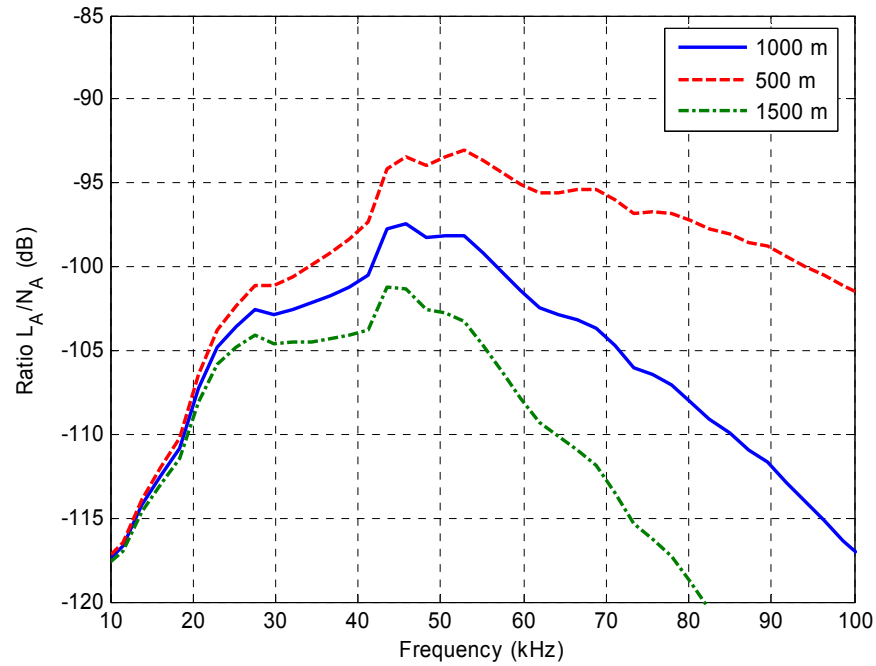


Figure 7.3. Ratio L_A/N_A plotted as a function of frequency at various transmission ranges

Although a 50 kHz center frequency is ideally suited for the communication range of interest, transducers available to us are more efficient at higher frequencies. Taking this efficiency into account, we selected a center frequency of 51 kHz for our first sea trial and 62 kHz for subsequent trials. In line with the trials, the simulation results presented later in this chapter assume a frequency band of 25 kHz centered at 62 kHz.

7.2.2. PSK Modulation Order

In our proposed scheme, the OFDM sub-carriers are modulated using PSK. Lower order PSK modulation provides lower data rates but better error performance for the same signal power. On the other hand, high order PSK modulation provides higher data rates at the cost of error performance. As bit error performance was expected to be a limiting factor at long ranges, we choose a low order PSK modulation. Gray coded QPSK in AWGN has the same bit error performance as BPSK [83]. However, in presence of S α S noise the Gray coded QPSK performance is expected to be somewhat inferior to BPSK as the in-phase and quadrature components of the baseband complex isotropic noise are correlated (Theorem 7). Nevertheless, in simulations and a majority of the experiments, we use Gray coded QPSK as the sub-carrier modulation scheme of choice.

During the first sea trial (details in the next chapter), we confirmed that the achievable effective data rates with QPSK were indeed higher than BPSK and 8-PSK. Although BPSK has the same bit error performance, it achieves a lower data rate as fewer bits are transmitted per symbol. 8-PSK transmits more bits per symbol. However, the increased BER requires a lower rate coding scheme for acceptable error performance. With the additional overhead of this coding scheme, the effective data rate is reduced to less than that provided by QPSK with higher rate coding.

7.2.3. Number of Carriers and Cyclic Prefix Length

The number of carrier N_c and the cyclic prefix length N_p are key parameters for any OFDM system. Let W be the bandwidth occupied by the OFDM signal and F_d be the symbol rate without cyclic prefix. Then,

$$W = N_c F_d . \quad (7.11)$$

The time occupied by the prefix T_p and the symbol time T_s (including the prefix) can be expressed in terms of N_c , N_p and W ,

$$\begin{aligned} T_p &= \frac{N_p}{N_c F_d} = \frac{N_p}{W} \\ T_s &= \frac{N_c + N_p}{N_c F_d} = \frac{N_c + N_p}{W}. \end{aligned} \quad (7.12)$$

For good OFDM performance, we require that the prefix should be longer than the delay spread τ_{ds} of the channel. As we use differential QPSK, we also require that the channel does not change significantly between two consecutive symbols. Hence the symbol length must be less than half the channel coherence time τ_c i.e.

$$T_p > \tau_{ds} \quad \text{and} \quad T_s < \frac{\tau_c}{2}. \quad (7.13)$$

We estimate the coherence bandwidth based on the delay spread of the channel [83],

$$W_c = \frac{0.423}{\tau_{ds}}. \quad (7.14)$$

We also require that the bandwidth of each sub-carrier be more than the coherence bandwidth of the channel so that each sub-carrier experiences flat fading. That is

$$\frac{W}{N_c} < W_c \quad \Rightarrow \quad N_c > \frac{W \tau_{ds}}{0.423}. \quad (7.15)$$

As 2 bits are transmitted per carrier (QPSK) in one symbol interval, the bandwidth efficiency η of the OFDM scheme is given by

$$\eta = \frac{2N_c}{WT_s} = \frac{2N_c}{W} \cdot \frac{W}{N_c + N_p} = \frac{2}{1 + \frac{N_p}{N_c}} \text{ bps/Hz}. \quad (7.16)$$

Thus, the efficiency depends only on the ratio N_p/N_c and increases as this ratio reduces. Subject to constraints in (7.13) and (7.15), we would like to select N_p and N_c such that the ratio N_p/N_c is as small as possible. Practical considerations limit the value of N_c to be a power of 2 (for efficient FFT implementations of OFDM) and the value of N_p to be a positive integer.

We estimate the delay spread based on significant terms in (6.18). If we assume a 1 km channel with 20 m water depth and transducers at mid-water depth, we obtain a delay spread of about 1.5 ms. With a coherence time of 70 ms and a bandwidth of 25 kHz, we represent various values of N_c from 64 to 512 and N_p from 32 to 64 on a N_c - N_p plane (Figure 7.4).

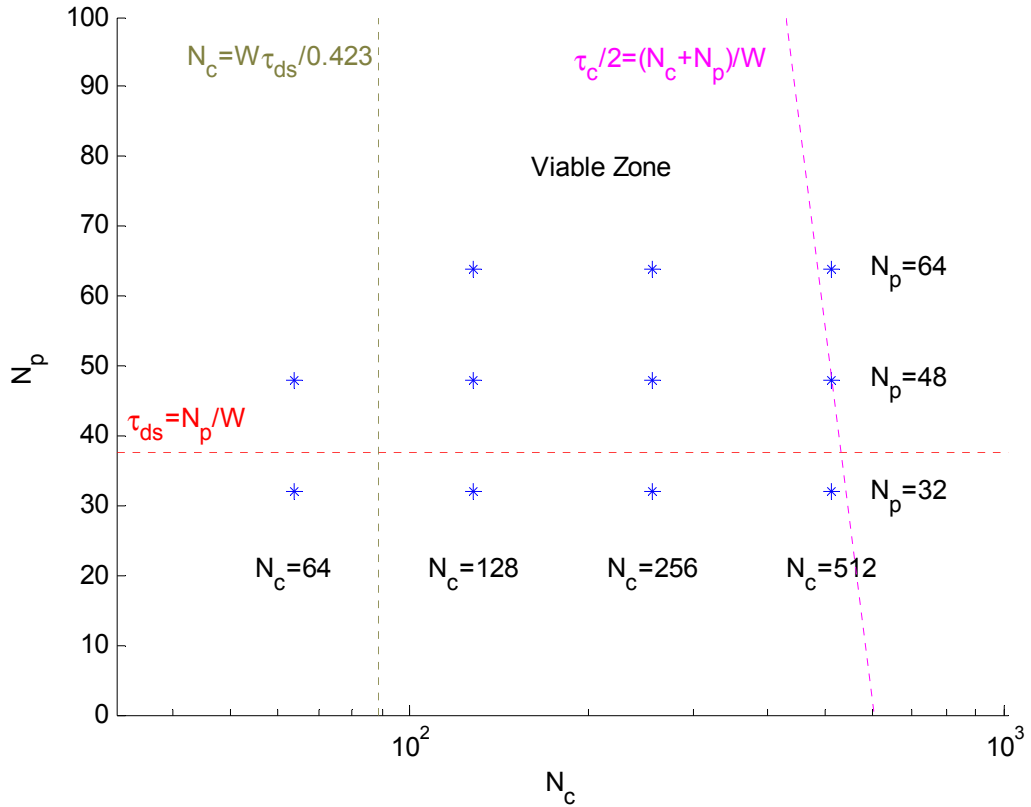


Figure 7.4. A plot of various OFDM schemes on a N_c - N_p plane and constraint boundaries for good performance marked for $\tau_c = 70$ ms, $\tau_{ds} = 1.5$ ms and $W = 25$ kHz

In Figure 7.4, the horizontal dashed line represents the constraint on prefix length. We expect that schemes with much shorter prefix lengths would not perform

well. The two vertical dashed lines represent the constraints on symbol length. We expect that schemes with symbols between the two vertical constraint lines and above the horizontal constraint line will perform well. Viable schemes lie in the zone defined by these constraints. The bandwidth efficiency increases as we move towards the bottom-right of the plane. Hence we expect that the best performing^{*} schemes would be close to the bottom-right corner of the viable zone. As the estimates for delay spread and coherence time are approximate, we consider the constraints defined by these as soft constraints. Hence we test several OFDM schemes (marked by stars) in the neighborhood of the constraint lines.

7.3. Simulations

To test the communication scheme proposed in this chapter, we simulated the performance of the scheme using the channel model developed in the previous chapter. Packets consisting of 3,456 uniformly distributed random bits were generated and coded using a serial concatenated $(1/2, 1/3)$ rate convolutional code as shown in Figure 7.5. The use of serial concatenated convolutional coding was motivated by the fact that the 1-norm Viterbi algorithm that we have developed for near-optimal decoding can be used for decoding of the component convolutional codes.

^{*} The performance criterion here is the effective data rate at a given maximum BER.

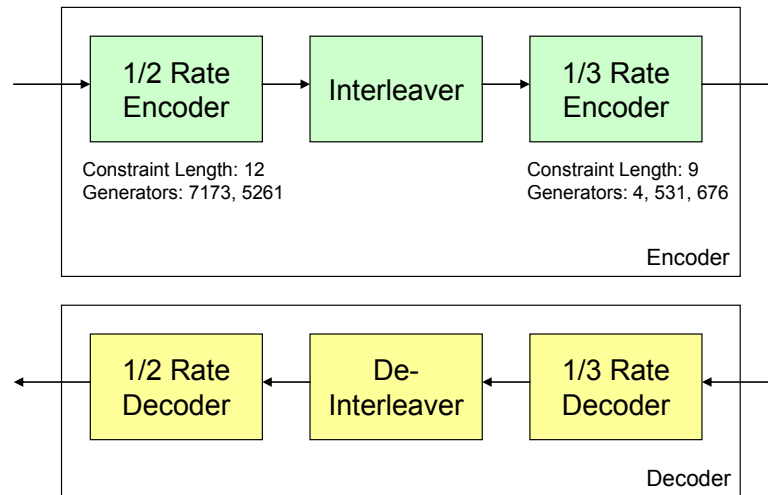


Figure 7.5. Encoder and decoder structures for serial concatenated convolutional codes

The resulting code was a 1/6 rate code with a long constraint length. A random block interleaver is inserted between the 2 encoders (and decoders) to break error bursts. The packets were modulated and transmitted through the channel simulator. The received packets were processed to estimate the raw BER (without coding), coded BER with a 1/3 rate code and the coded BER with a 1/6 rate code. The serial concatenated code was decoded using an inner Viterbi decoder for the 1/3 rate code followed by an outer hard-decision Viterbi decoder for the 1/2 rate code. Inner Viterbi decoders with hard-decision decoding, Euclidean metric soft-decision decoding and 1-norm metric soft-decision decoding were tested. Simulations were performed on a channel with 20 m water depth and transducers at near mid-water depth. Ranges from 250 m to 1.5 km were numerically tested in steps of 250 m by transmitting 8 packets from each of 11 OFDM schemes (denoted in Figure 7.4 by stars) at each range. The total bandwidth used by each OFDM signal was 24,320 Hz.

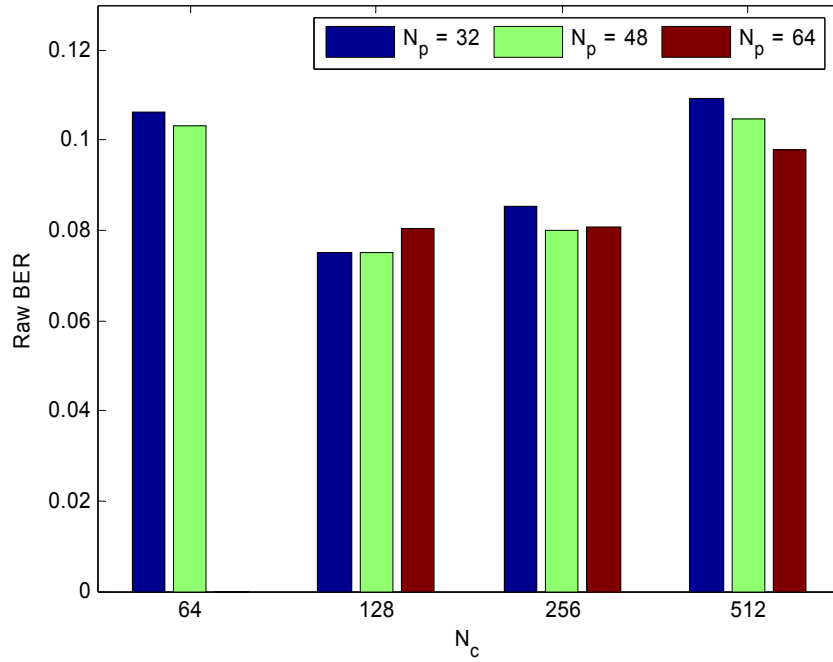


Figure 7.6. Simulation results showing raw BER for 11 OFDM schemes at 1 km range

Figure 7.6 shows the raw BER from the 11 OFDM schemes at 1 km range. The performance of $N_c = 64$ schemes is poor as the sub-carrier bandwidth is larger than the coherence bandwidth of the channel. The performance improves substantially at $N_c = 128$ but steadily decreases up to $N_c = 512$ as the symbol length approaches the coherence time of the channel.

Figure 7.7 shows the raw BER for 3 OFDM schemes with 128, 256 and 512 carriers and a cyclic prefix of length 32. All schemes show the same trend over range. It is initially surprising that the performance at short ranges is inferior to that at medium range. However, we should note that the OFDM parameters chosen were based on channel characteristics at medium range and hence optimized for the range. At small ranges, the delay spread of the channel is longer than the cyclic prefix and therefore the performance is poor. As the range increases, the delay spread reduces and the performance improves. At long ranges, absorption reduces the signal strength substantially and the SNR drops and the performance degrades. The best performance

at 1 km is the result of our choice of parameters. If communication at a shorter or longer range is desired, optimal parameters for that range can be chosen based on the revised constraints.

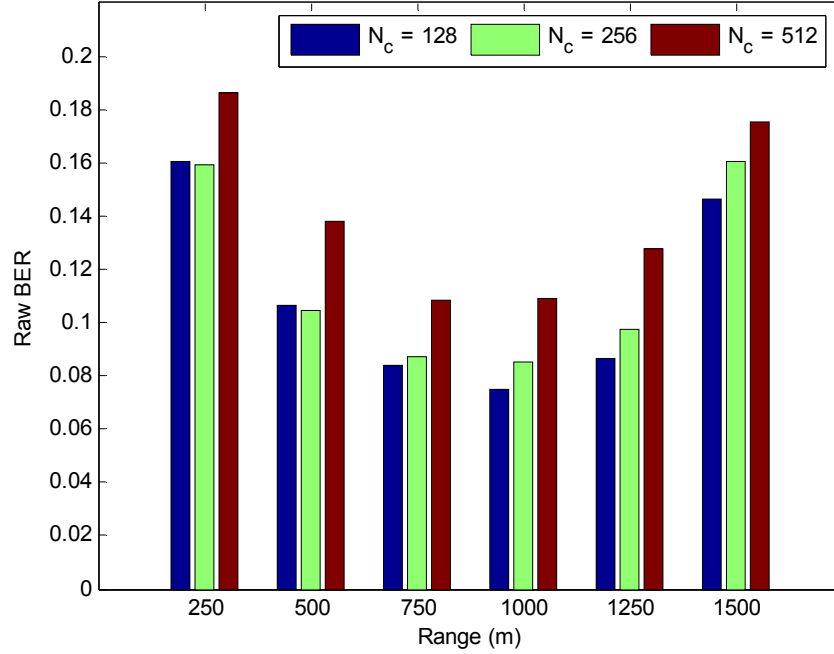


Figure 7.7. Simulation results showing raw BER as a function of range for various OFDM schemes with $N_p = 32$

Figure 7.8 shows the coded performance of the OFDM scheme with 128 carriers and a cyclic prefix of length 32. Decoding was performed with a hard-decision Viterbi decoder, a soft-decision Viterbi decoder with Euclidean branch metric and a soft-decision Viterbi decoder with 1-norm branch metric. Although all three decoders show an improvement over the uncoded data, the 1-norm branch metric based decoder performs best. The hard-decision decoder's performance is slightly inferior. The Euclidean branch metric based decoder performs considerably poorer. These results agree with the theoretical predictions from Chapter 5.

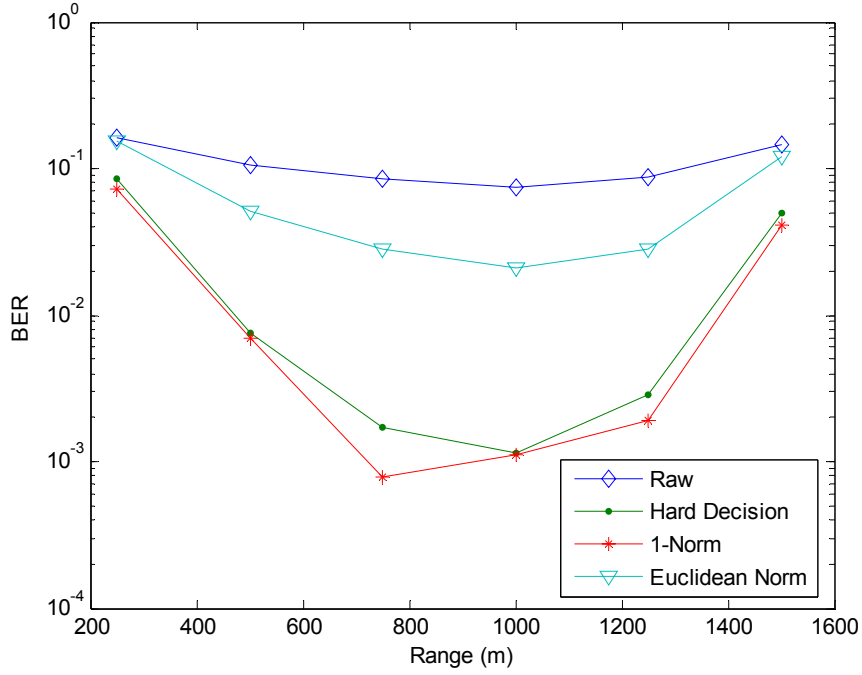


Figure 7.8. Simulation results showing the 1/3 rate coded performance of OFDM with $N_c = 128$, $N_p = 32$ with hard-decision decoding, soft-decision decoding with Euclidean norm and soft-decision decoding with 1-norm

Table 7.1 presents a summary of the simulated performance of all the 11 OFDM schemes at 1 km range decoded using a soft-decision Viterbi decoder with the 1-norm branch metric. The raw (uncoded), 1/3 rate coded and 1/6 rate coded performances are shown. We choose a performance criterion of $BER < 10^{-4}$ or better as acceptable at the physical layer for most communication applications. None of the uncoded or 1/3 rate coded schemes satisfy the performance criterion. All the 1/6 rate coded schemes satisfy the criterion. Out of the 1/6 rate coded schemes, the highest bandwidth efficiency (data rate of 7,630 bps) is achieved by the scheme with $N_c = 512$ and $N_p = 32$. If the performance criterion was relaxed to $BER < 10^{-3}$ or better, a better data rate (12,971 bps) would be achieved by the 1/3 rate coded scheme with $N_c = 128$ and $N_p = 32$. Further improvements in effective BER can be obtained at higher protocol layers via error detection and retransmission schemes.

Table 7.1. Simulated performance of various OFDM schemes at 1 km range using soft-decision Viterbi decoding with 1-norm metric

N_c	N_p	Uncoded		1/3 Rate Coding		1/6 Rate Coding	
		Data Rate (bps)	BER	Data Rate (bps)	BER	Data Rate (bps)	BER
64	32	32,427	0.1063	10,809	0.0048	5,404	0.0000
64	48	27,794	0.1033	9,265	0.0027	4,632	0.0000
128	32	38,912	0.0750	12,971	0.0010	6,485	0.0000
128	48	35,375	0.0752	11,792	0.0006	5,896	0.0000
128	64	32,427	0.0802	10,809	0.0006	5,404	0.0000
256	32	43,236	0.0855	14,412	0.0015	7,206	0.0000
256	48	40,960	0.0800	13,653	0.0034	6,827	0.0000
256	64	38,912	0.0807	12,971	0.0010	6,485	0.0000
512	32	45,779	0.1093	15,260	0.0061	7,630	0.0000
512	48	44,471	0.1049	14,824	0.0064	7,412	0.0000
512	64	43,236	0.0974	14,412	0.0057	7,206	0.0000

The simulation results confirmed that our proposed communication scheme is viable for use for underwater communications. They helped validate our understanding of the constraints on the choice of number of carriers and prefix length. Although the exact experimental conditions may not be the same as the simulated channel conditions, the channel model helped us assess the likely performance of the communication scheme in warm shallow waters. Based on the simulations, we expect to be able to achieve data rates of about 7.6 kbps at a range of 1 km.

7.4. Conclusions

In this chapter, we developed a communication scheme for use in WSWA channels. The scheme was inspired by our understanding of the WSWA channel and the impulsive ambient noise. The scheme consists of OFDM modulation at its heart,

with differential QPSK being used to modulate each sub-carrier. The differential modulation eliminates the need for channel tracking and carrier synchronization. A cyclic prefix is employed to eliminate ISI due to multipath. A symbol synchronization scheme based on the correlation of the cyclic prefix with the symbol is employed to track the slow variation in symbol timing. Convolutional coding adds error correction capability to the scheme. The decoding is performed using a 1-norm Viterbi decoder to combat non-Gaussian ambient noise. A random block interleaver is used to effectively utilize the time-frequency diversity in the channel. Finally, a DSSS preamble is added for frame synchronization.

The choice of parameters in the OFDM scheme is critical to its performance. We developed methods to select frequency band, number of carriers and the prefix length based on measurable channel characteristics such as delay spread, coherence time and ambient noise PSD.

We simulated the communication scheme with various choices of parameters in a WSWA channel using the model developed in the previous chapter. The simulations helped to validate our understanding of the channel, choice of parameters and the overall communication scheme. Based on these simulations, we expect to be able to achieve data rates of 7.6 kbps at a range of approximately 1 km.

8. *Experimental Results*

Apart from the field testing of the sign correlator described in Chapter 4 and the channel measurements described in Chapter 6, we performed two sea trials to validate our channel model and communication scheme. The first sea trial was designed primarily as an experiment to validate and calibrate the channel model at various ranges. During this trial, we captured a channel realization at 350 m range by transmitting an OFDM signal and recording the received signal. Analysis from this trial is presented in Section 8.1 [91].

The second sea trial was designed to test selected OFDM schemes developed in the last chapter at different ranges. In this trial, we successfully achieved reliable data communications up to a range of 1 km. Analysis of the data from this trial is presented in Section 8.2.

8.1. *Sea Trial 1*

8.1.1. Experimental Setup

The first sea trial was performed in February 2005 in Singapore waters at Raffles Reserve (1°12.10' N 103°44.58' E). The location has a water depth of 15-20 m and a sandy-muddy bottom. During the experiment, the sea was calm with mild winds but strong currents. The transmitter and receiver systems were deployed from two vessels as described below (Figure 8.1).

The transmission system was deployed from a vessel at anchor. The transmitter consisted of a ruggedized desktop computer with a digital-to-analog converter card, power amplifier and an ITC1042 transducer. The transducer was deployed at a depth of approximately 5 to 8 m using a 10 kg weight. The receiver system was deployed

from another vessel at anchor. This vessel moved to several distances from the transmitting vessel and re-anchored. The receiver consisted of a laptop, an external firewire analog-to-digital converter, a pre-amplifier (with band-pass filter) and a TC4013 hydrophone. The hydrophone was deployed at a depth of approximately 3 to 5 m using a 10 kg weight. The received signals were recorded for post-processing and analysis.

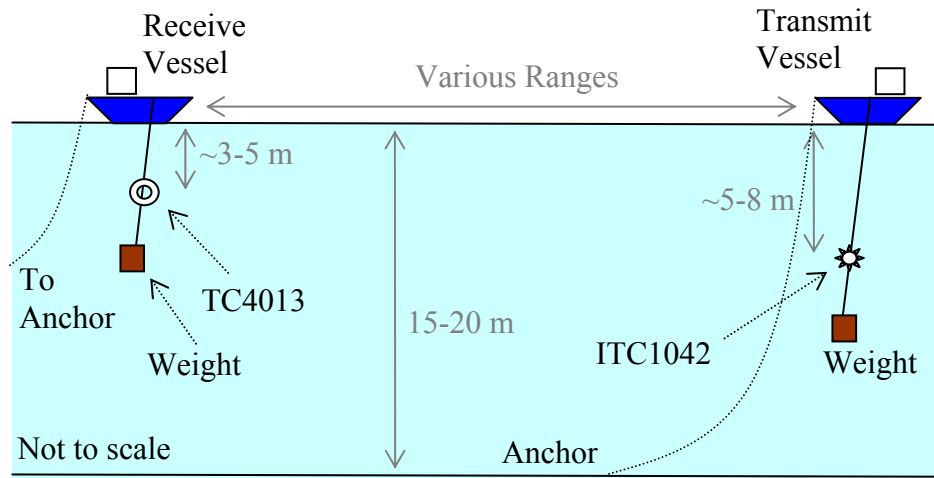


Figure 8.1. Schematic representation of the setup for Sea Trial 1

Channel measurements to estimate coherence time and delay spread were made at various ranges from 350 m to 1.1 km. Long sinusoidal signals (at frequencies 45, 55 and 65 kHz) and DSSS signals (25 kHz signals centered at 51 kHz) were used for channel measurement. An OFDM signal with 64 sub-carriers and a cyclic prefix of length 32 utilizing a bandwidth of 24 kHz around a center frequency of 51 kHz was transmitted at a range of 350 m. Although the peak transmission performance of the ITC1042 is at about 80 kHz, it has an acceptable transmit performance in the signal band (39-63 kHz). The total transmit source level was estimated to be approximately 170 dB re 1 Pa² at 1m. The TC4013 has an almost flat receive sensitivity over the above signal band.

The ambient noise at the location was analyzed and found to be non-Gaussian as expected. The average noise level was measured to be between 58 and 60 dB re 1 Pa²/Hz. This amounts to a total ambient noise level of approximately 104 dB re 1 Pa² in the signal band. The amplitude probability distribution of the noise in the signal band was found to be S α S, as expected for snapping shrimp dominated ambient noise, with characteristic exponent 1.69 and scale parameter 6.8×10^4 Pa.

8.1.2. Coherence Time and Delay Spread

The coherence time of the channel was estimated using (6.10) and the measured Doppler spread of long sinusoidal signals (at 45, 55 and 65 kHz) transmitted through the channel. The coherence times computed for the three frequencies were averaged to yield the final estimate. The delay spread was estimated based on cross-correlation of a DSSS signal transmitted through the channel with a reference copy. Table 8.1 shows the estimated coherence time and delay spread at various ranges.

Table 8.1. Measured channel coherence time and delay spread

Range (m)	Coherence Time (ms)	Delay Spread (ms)
380	93	1.2
700	62	1.3
1090	79	0.9

The coherence time of the channel is consistent with expected values documented in Chapter 6. Due to the low source level used in this experiment, the SNR is expected to be low. Weak arrivals would therefore be lost resulting in under estimating the delay spread. We compare the estimates of delay spread with simulation, taking into account only arrivals up to 20 dB lower than the direct arrival. The simulated delay spreads are shown in Table 8.2.

Table 8.2. Comparison of measured delay spreads against predictions based on simulation

Range (m)	Measured Delay Spread (ms)	Predicted Delay Spread (ms)
380	1.2	2.3
700	1.3	1.3
1090	0.9	0.8

The measured delay spreads agree closely with simulations at 700 m and 1090 m. However, at 380 m, the simulated delay spread is much longer than the measured delay spread. This may be the result of an absorbing seabed near the receiving vessel.

8.1.3. Estimation of OFDM Performance

Due to hardware constraints during this experiment, the source level of the OFDM signals was low. Hence we recorded OFDM signals with a good SNR only at the shorter range of 350 to 380 m. The OFDM signal used contained 64 sub-carriers at a spacing of 375 Hz. Based on the measured delay spread and (7.14), each sub-carrier bandwidth is slightly larger than the coherence bandwidth of the channel. The cyclic prefix length was 32 i.e. 1.3 ms, slightly longer than the measured delay spread of the channel at that range. Each symbol was 4 ms long, well within the measured coherence time of the channel. A total of 25,000 OFDM symbols (160,000 PSK symbols) were transmitted during the test.

We captured a channel realization by transmitting random data symbols T_{jm} at symbol j on sub-carrier m and recording the resulting demodulated data symbols R_{jm} . Assuming that each sub-carrier undergoes flat fading and additive noise, we have

$$R_{jm} = H_{jm}T_{jm} + N_{jm} \quad (8.1)$$

where H_{jm} is the complex channel state and N_{jm} is the complex noise.

The recorded channel realization enabled us to test various PSK modulation orders, coding schemes and interleavers in post-processing. We simulated the transmission of data symbols X_{jm} by assuming that symbols X_{jm} were mapped to T_{jm} using a set of phase rotations M_{jm} , such that

$$T_{jm} = M_{jm} X_{jm} . \quad (8.2)$$

The expected received data symbols Y_{jm} can then be estimated using

$$\begin{aligned} Y_{jm} &= \frac{1}{M_{jm}} R_{jm} \\ &= \frac{1}{M_{jm}} (H_{jm} T_{jm} + N_{jm}) \\ &= \frac{1}{M_{jm}} (H_{jm} M_{jm} X_{jm} + N_{jm}) \\ &= H_{jm} X_{jm} + \frac{N_{jm}}{M_{jm}} . \end{aligned} \quad (8.3)$$

Received data symbols Y_{jm} are therefore the symbols that would have been received in the experiment if we had transmitted X_{jm} instead of T_{jm} with the only difference arising from the noise. As X_{jm} and T_{jm} are PSK symbols, the magnitude of M_{jm} is always 1. Hence the effective noise level in the estimated received data is the same as the channel noise.

8.1.4. OFDM Performance Results

By computing phase rotations for various PSK modulations, coding schemes and interleavers, we were able to test the performance of these schemes as if the symbols transmitted through the channel were indeed generated using these schemes. All performance measurements in this section were made on a transmitted packet containing 160,000 coded symbols.

The results are tabulated in Table 8.3. With no error correction coding, the performance of the system in terms of BER was poor. As expected, the system

showed an increase in BER with increased modulation order. In the presence of Gaussian noise, we would have expected the BER of BPSK and Gray coded QPSK to be the same. However, in presence of SoS noise, the noise on the in-phase and quadrature channels of QPSK are correlated (Theorem 7). This results in a higher BER than that in BPSK as expected.

Table 8.3. Raw performance of OFDM with differential PSK during Sea Trial 1

Modulation	Effective Data Rate (bps)	BER
BPSK	16,000	7.2×10^{-2}
QPSK	32,000	1.3×10^{-1}
8-PSK	48,000	2.0×10^{-1}

With error correction coding, the BER performance of the system could be improved at the cost of reduced data rate. The performance of various combinations of modulation order and coding schemes are shown in Table 8.4. The rows where only “Code 1 Rate” is specified show results from schemes which use single convolution codes for error correction. The rows where both “Code 1 Rate” and “Code 2 Rate” are specified show results from schemes with serial concatenated convolution codes (refer to Figure 7.5 for details) for error correction. A hard-decision Viterbi decoder was used throughout this experiment.

The 5th column shows the BER without interleaver. This BER was computed by disabling the channel interleaver shown in Figure 7.2 but enabling the coding interleaver shown in Figure 7.5 during serial concatenated coding. None of the coding schemes tested with the channel interleaver switched off met a BER criterion of $<10^{-4}$.

With the channel interleaver switched on, the communication scheme can effectively utilize time and frequency diversity in the channel. Hence, the performance of the communication system could be improved via interleaving without incurring any cost in terms of data rate but a small cost in transmitter and receiver complexity. The results from schemes with coding and interleaving are shown in the 6th column (BER with interleaving). All modulation orders and coding schemes benefited from the use of the channel interleaver.

Table 8.4. Coded performance of OFDM with differential PSK during Sea Trial 1

Modulation	Code 1 Rate	Code 2 Rate	Effective Data Rate (bps)	BER (without interleaver)	BER (with interleaver)
BPSK	1 / 2	-	8,000	2.5×10^{-2}	1.2×10^{-2}
BPSK	1 / 3	-	5,333	6.8×10^{-3}	3.2×10^{-4}
BPSK	1 / 4	-	4,000	4.4×10^{-3}	$< 10^{-4}$
QPSK	1 / 3	-	10,666	3.8×10^{-2}	1.6×10^{-2}
QPSK	1 / 4	-	8,000	1.2×10^{-2}	1.5×10^{-3}
QPSK	1 / 2	1 / 3	5,333	2.3×10^{-4}	$< 10^{-4}$
8-PSK	1 / 4	-	12,000	9.4×10^{-2}	7.7×10^{-2}
8-PSK	1 / 2	1 / 4	6,000	6.2×10^{-2}	2.9×10^{-2}
8-PSK	1 / 3	1 / 4	4,000	5.0×10^{-4}	4.3×10^{-4}
8-PSK	1 / 4	1 / 4	3,000	1.3×10^{-4}	$< 10^{-4}$

Figure 8.2 shows the performance of OFDM schemes with varying modulation orders and code rates. The effective data rate is a function of modulation order and coding. The BER obtained for different schemes (with channel interleaving) are plotted as a function of effective data rate. BPSK has a good error performance and therefore requires less coding. However, it offers a low data rate. 8-PSK offers a high raw data rate but requires a large degree of coding due to the high raw BER. Hence

the effective data rate is lower than BPSK. QPSK offers the best trade off between modulation order and coding.

For a BER criterion of $<10^{-4}$, differential QPSK with a serial concatenated code (outer code rate 1/2, inner code rate 1/3) demonstrated the highest effective data rate of 5.3 kbps in this experiment.

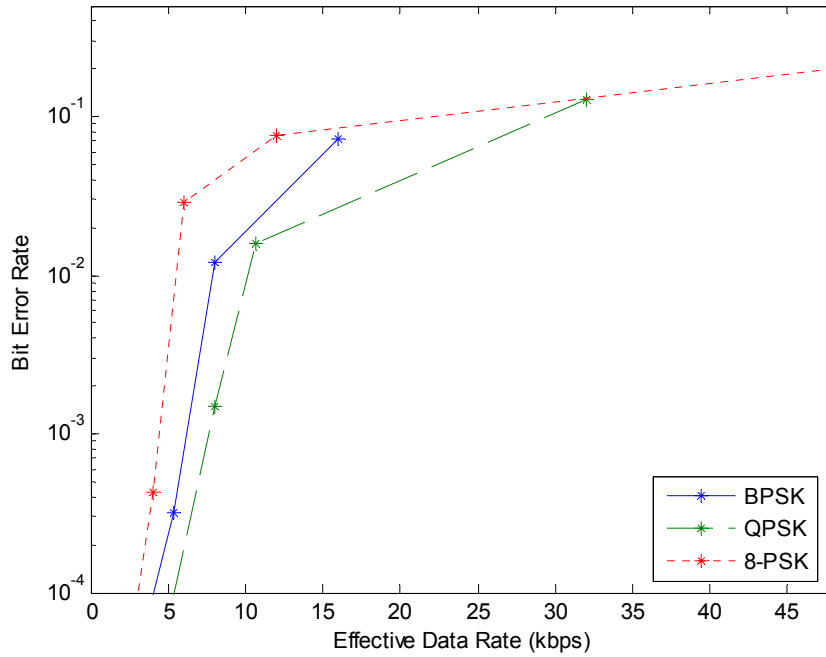


Figure 8.2. Performance of differential BPSK, QPSK and 8-PSK based OFDM schemes with different degrees of coding

In this experiment, we demonstrated that OFDM could be successfully implemented in a WSWA channel with the use of a cyclic prefix and differential PSK modulation. The BER performance of uncoded OFDM was poor. The use of serial concatenated convolution coding and a channel interleaver improved the BER performance of OFDM significantly. We were able to demonstrate transmissions at an effective data rate of up to 5.3 kbps at a range of 350 m with a BER of 10^{-4} or better.

8.2. Sea Trial 2

8.2.1. Experimental Setup

We tested the performance of selected OFDM schemes in Singapore waters during a field trial conducted at Raffles Reserve (1°11.55' N 103°45.00' E) in November 2005. The location has water depths of 16 to 18 m. The experimental setup was similar to the preliminary trials with the transmission and reception systems deployed on two anchored research vessels. The transmission/reception systems from the first sea trial were replaced by a custom designed data transmission/acquisition system described below. The transducers for transmission and reception were deployed at about 8 to 10 m depth. The weather during the trials was windy with some rain, and the sea surface was mostly disturbed. There were strong currents during a significant part of the trial.

The transmission and reception of the signals were achieved with a custom data transmission/acquisition system, capable of transmitting signals up to a source level of 193 dB re 1 Pa² at 1m. Due to the high PAPR of OFDM signals, the estimated source level during our trials was about 187 dB re 1 Pa² at 1m. The transducer has a peak transmit response near 80 kHz. We used a frequency band of 24,320 Hz centered at 62 kHz during the trials. The system was set up to record short bursts of data at a sampling rate of 250 kHz and a resolution of 12 bits. The receiving sensitivity of the transducer is relatively flat over the signal bandwidth. The system is equipped with an automatic gain control to optimize the dynamic range during acquisition.

OFDM signals similar to the ones used for simulation in Section 7.3 were used during the trial. We present the analysis for two signals – one which demonstrated lowest BER during the simulations, and another which had the highest bandwidth efficiency of all signals tested during simulations. The lowest BER signal had 128

carriers and a prefix length of 32 (referred to as OFDM-128/32). The most bandwidth efficient signal had 512 carriers and a prefix length of 32 (referred to as OFDM-512/32). Both signals used differential QPSK to modulate the sub-carriers and serially concatenated (1/2, 1/3) rate convolutional codes in line with the simulations. The channel interleaver was used in all cases. Each packet consisted of a DSSS preamble to help locate the signal, followed by a 3 ms gap and an OFDM packet with 3,456 data bits (20,736 coded bits). The packets were repeated at a rate of approximately 1 Hz. During each acquisition, a burst of 3 to 5 packets was recorded (acquisition of 4 s of data). Two bursts of each signal type were recorded at each range with approximately half hour time difference between the two recordings.

The trial was performed at 3 different ranges – 400 m, 800 m and 1 km. At 400 m, the measured delay spread was approximately 4 ms. This delay spread is consistent with predictions from our channel model. As the delay spread is significantly longer than the cyclic prefix in the signals (1.3 ms prefix), the performance at this range was expected to be poor. The measured raw BER was between 0.16 and 0.20 and the data could not be successfully decoded. At ranges of 800 m and 1 km, the measured delay spread was approximately 1 ms and packets were successfully decoded. Analysis of data collected at these ranges is presented in the next section.

8.2.2. Results

Figure 8.3 shows the raw BER performance of 7 packets of OFDM-128/32 at a range of 800 m. The BER for each packet varies between 0.06 and 0.1. The average BER is shown in the last column and is approximately 0.08. This BER agrees closely with the simulated BER at 750 m for the same OFDM scheme (Figure 7.7).

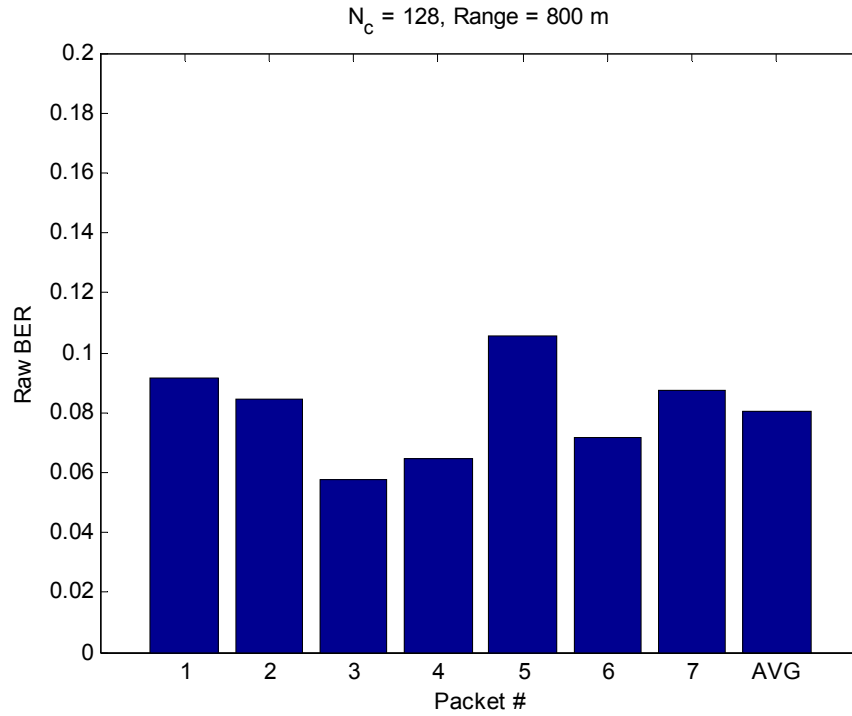


Figure 8.3. Performance of OFDM-128/32 at 800 m range without coding

Figure 8.4 shows the performance of OFDM-128/32 with 1/3 rate coding at a range of 800 m. The decoding performance of the 1-norm Viterbi decoder is better than the hard-decision and Euclidean norm Viterbi decoders for most packets. The Euclidean norm Viterbi decoder performs poorly; this was expected based on theoretical study and simulation in previous chapters. The average BER with 1-norm Viterbi decoding with the 1/3 rate code is 0.0007. This agrees closely with the simulated results (Figure 7.8). Using a 1/6 rate coding, OFDM-128/32 is able to recover all transmitted packets without any errors. With over 24,000 bits transmitted in 7 packets, this translates to a BER of 4×10^{-5} or better.

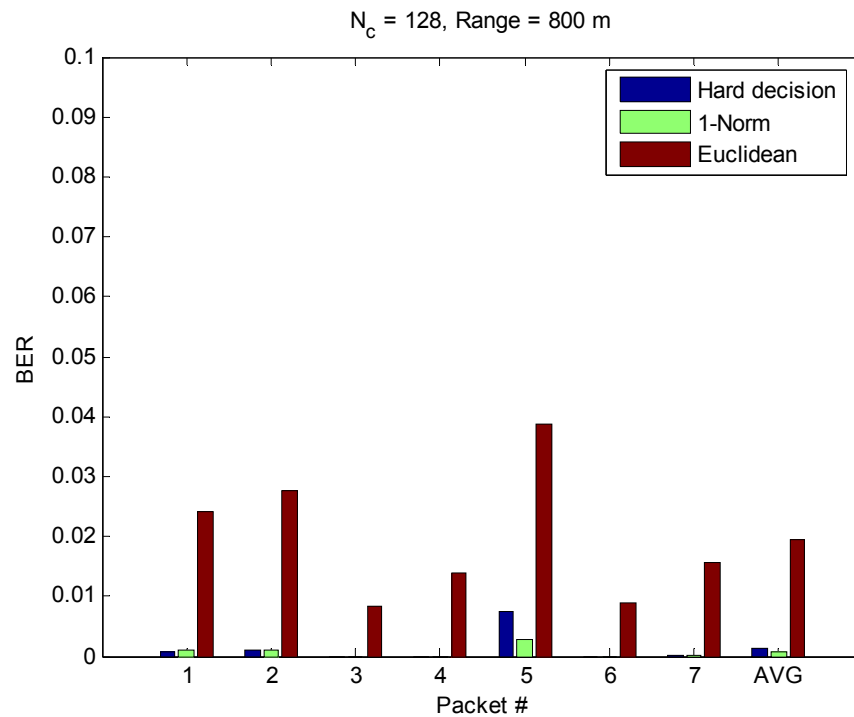


Figure 8.4. Performance of OFDM-128/32 at 800 m range with 1/3 rate coding

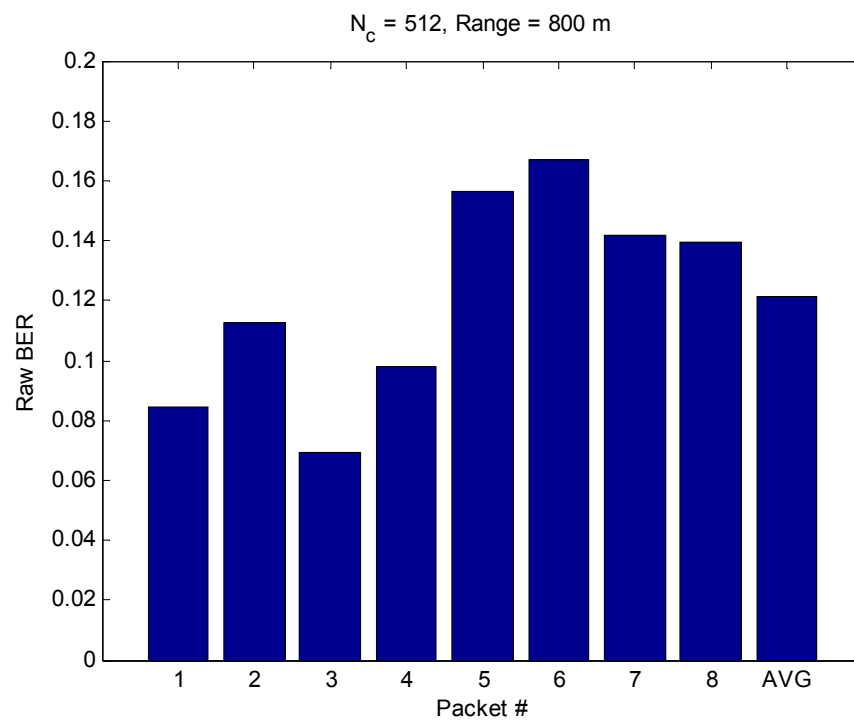


Figure 8.5. Performance of OFDM-512/32 at 800 m range without coding

Figure 8.5 shows the performance of OFDM-512/32 at a range of 800 m without coding. The first 4 packets have a significantly lower BER than the next 4 packets.

The first 4 packets were transmitted during the first burst within a few seconds of each other, while the next 4 packets were transmitted during the second burst half an hour later. The increased BER during the second burst may be due to change in channel characteristics over that time. This may be a result of tidal water depth change, change in depth of transducers due to change in currents or movement of the vessels around the anchor. The average BER of 0.12 is not significantly different than the BER predicted via simulation (simulated BER = 0.11, see Figure 7.7).

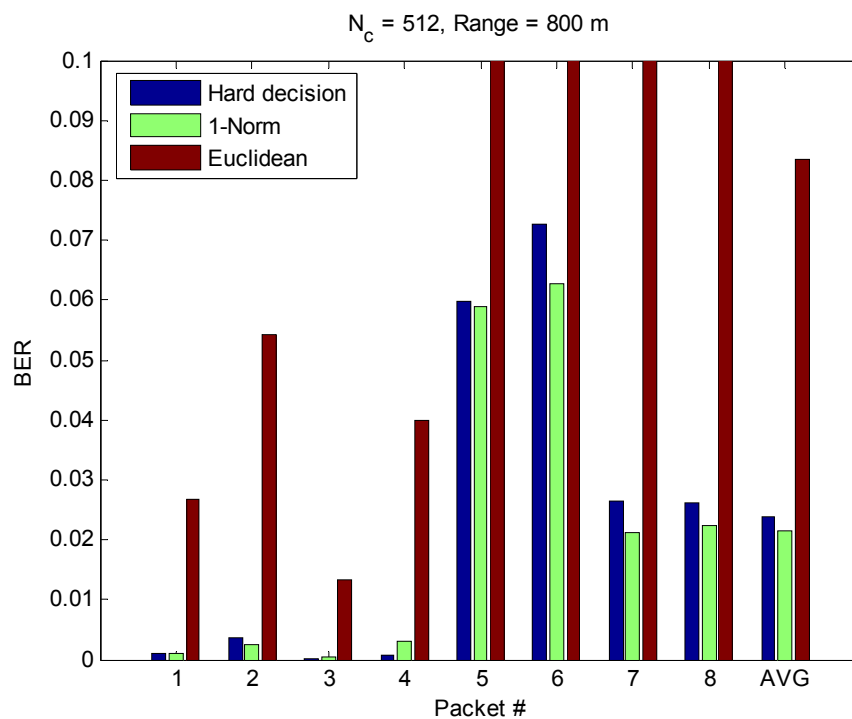


Figure 8.6. Performance of OFDM-512/32 at 800 m range with 1/3 rate coding

Figure 8.6 shows the performance of the OFDM-512/32 scheme with a 1/3 rate coding at 800 m. The Euclidean norm Viterbi decoder performs very poorly, especially for the later packets. The 1-norm Viterbi decoder demonstrates the best performance, yielding an average BER of 0.02. The hard-decision Viterbi decoder performance is only slightly inferior to the 1-norm Viterbi decoder. With a 1/6 rate coding, the OFDM-512/32 with hard-decision and 1-norm Viterbi decoding is able to recover all packets perfectly.

Figure 8.7 and Figure 8.8 show the raw and 1/3 rate coded performance of OFDM-128/32 at a range of 1 km. The first 3 packets have a much lower BER than the next 4 packets. These initial 3 packets were received during the first burst within a few seconds, while the next 4 packets were received during the second burst half an hour later. Thus the difference in BER is likely to be a result of changes in the channel as observed for OFDM-512/32 in the 800 m channel. The observed average raw BER of a little over 0.1 is somewhat higher than the simulated performance of 0.08 (Figure 7.7). This may be a result of reduced SNR due to slightly lower source level used during the experiment as compared to the simulations.

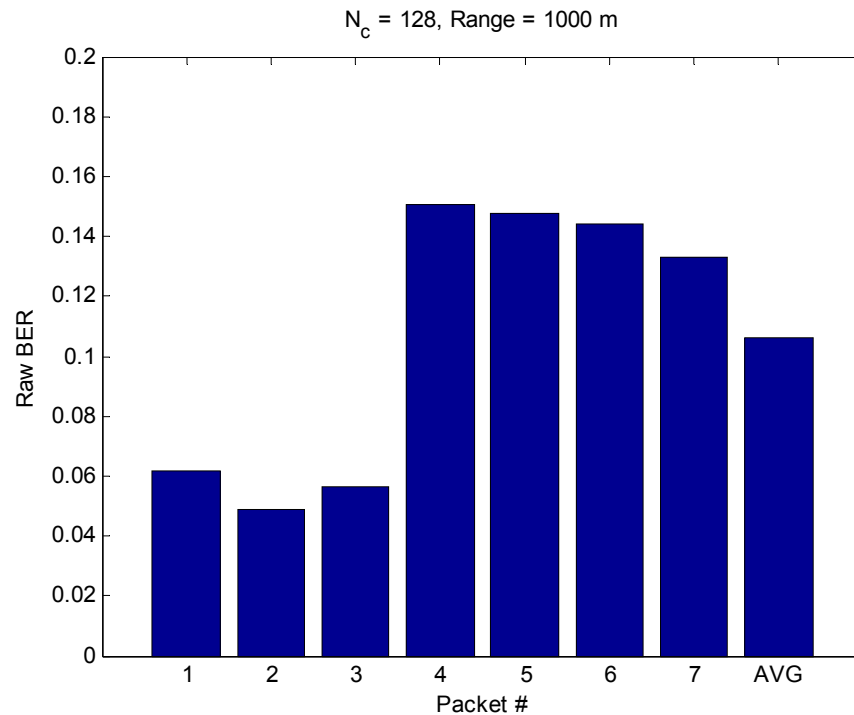


Figure 8.7. Performance of OFDM-128/32 at 1 km range without coding

The 1-Norm Viterbi decoding is able to successfully recover the initial 3 packets after the 1/3 rate decoding. However, in case of the last 4 packets, residual errors remain after the first stage of decoding. With the 1/6 rate decoding, all errors are corrected and the packets are successfully recovered.

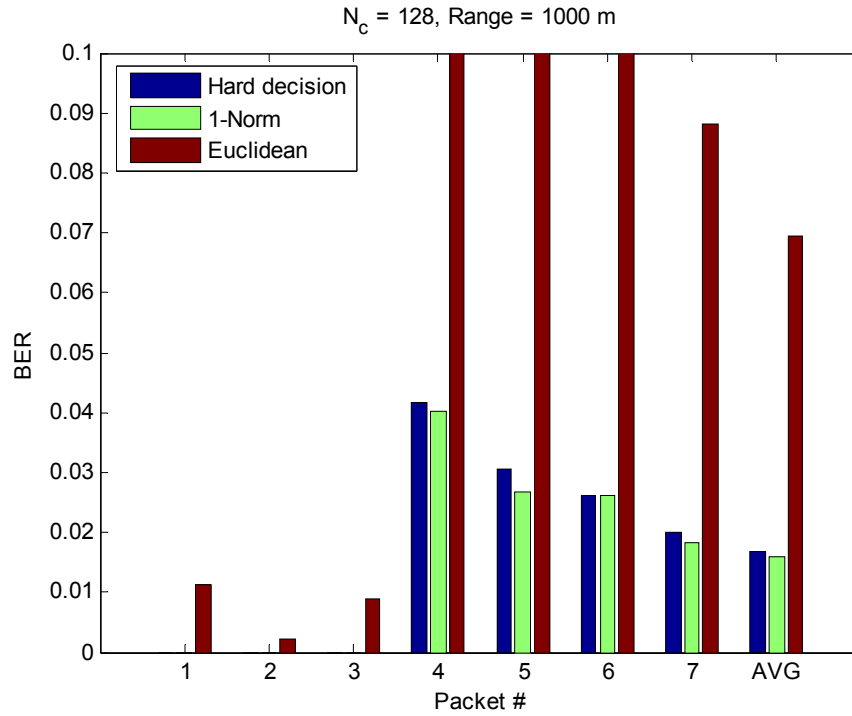


Figure 8.8. Performance of OFDM-128/32 at 1 km range with 1/3 rate coding

Figure 8.9 and Figure 8.10 show the raw and 1/3 rate coded performance of OFDM-512/32 at a range of 1 km. The average raw BER of 0.1 agrees closely with the performance predictions via simulations (Figure 7.7). The average 1/3 rate coded BER is 0.006 when decoded using the 1-norm Viterbi decoder; the equivalent simulated BER was 0.001 (Table 7.1). With a 1/6 rate code, OFDM-512/32 packets can be decoded without any errors.

The results from this experiment demonstrate that both OFDM-128/32 and OFDM-512/32 with coding are viable communication schemes in WSWA at ranges between 800 m and 1 km. The observed performance of both schemes is close to the performance predicted via simulations. With a 1/3 rate code and the use of a 1-norm Viterbi decoder, many packets are recovered perfectly. However, a 1/6 rate code was required to ensure that all the packets were recovered without any errors. OFDM-512/32 has higher bandwidth efficiency than OFDM-128/32. Its effective data rate with the 1/6 rate code was 7,630 bps.

OFDM-512/32 with 1/3 rate code was able to achieve an average BER $< 10^{-4}$ at a range of 800 m. This translates to an effective data rate of 15,260 bps.

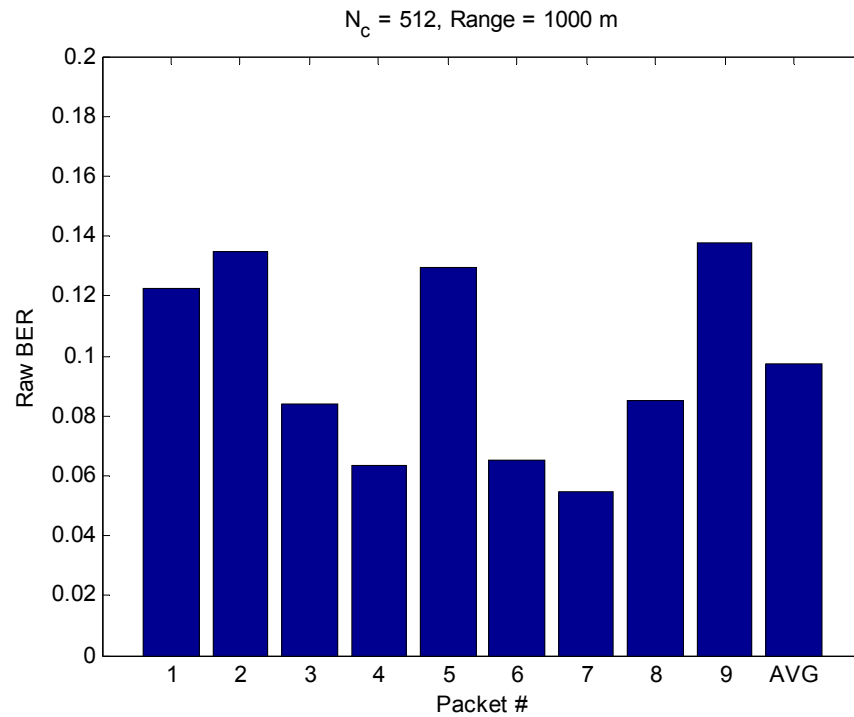


Figure 8.9. Performance of OFDM-512/32 at 1 km range without coding

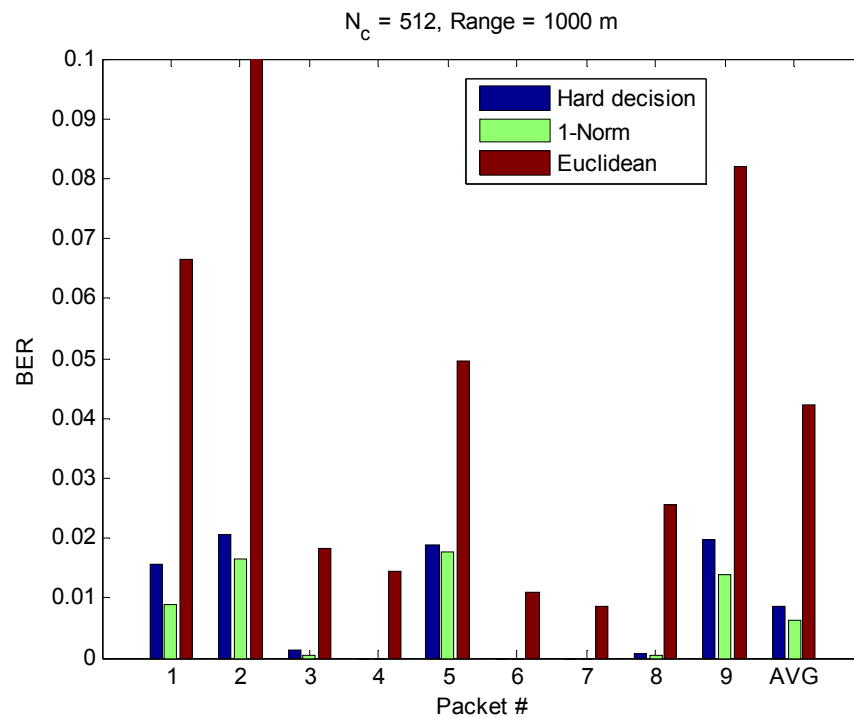


Figure 8.10. Performance of OFDM-512/32 at 1 km range with 1/3 rate coding

8.3. Conclusions

In this chapter, we described two field trials and analyzed the data collected. During the first trial, we demonstrated that coded OFDM could be successfully implemented in a WSWA channel with the use of a cyclic prefix and differential QPSK modulation. We were able to demonstrate error-free transmissions at an effective data rate of up to 5.3 kbps at a range of 350 m. We also successfully tested the prediction that a channel interleaver would improve communication performance in presence of snapping shrimp dominated ambient noise.

The second trial tested the performance of two coded OFDM schemes at ranges of 800 m and 1 km. Both schemes were able to successfully recover all packets after decoding. At a range of 1 km, we were able to achieve error-free communications at 7.6 kbps. Assuming a performance criterion of $\text{BER} < 10^{-4}$, we were able to establish communications at 15 kbps at a range of 800 m. This performance is significantly better than performance of commercially available systems in local waters. Through this trial, we validated our prediction that the 1-norm Viterbi decoder is superior to the hard-decision and Euclidean Viterbi decoders in presence of impulsive ambient noise. The performance predictions from the simulations documented in the previous chapter agreed quite closely with the measured performances. This suggests that our channel model captures the essential characteristics of the WSWA channel.

9. *Conclusions & Further Research*

9.1. *Conclusions*

The WSWA channel has posed a challenge for communication systems. The performance of commercial communication systems in this channel has been poor. No commonly accepted channel model exists for this channel, and most researchers use a white Gaussian noise assumption, which is clearly violated in the channel. A lack of accurate understanding and modeling of the channel leads to development of communication schemes that perform poorly in the WSWA channel.

We have developed a physics-based channel model for the WSWA channel. The model assumes ray propagation in an isovelocity medium and includes effects such as spreading, attenuation, reflection losses, etc. The model also includes time-varying statistical effects such as fading and movement of transducers. The model was calibrated using channel measurements made at sea. The channel was validated at two levels – the impulse response and time variation predicted by the model was compared against measurements, and the performance of OFDM in the simulated channel was compared against experimental performance of OFDM at sea. The channel model captures most aspects of WSWA channels accurately.

The channel model has an additive ambient noise component. In contrast with most UWA communications research which assumes Gaussian noise, we have modeled the ambient noise in WSWA channels as $S\alpha S$ noise. This has many implications on the design of communication systems for the WSWA channel. For example, the noise on the in-phase and quadrature components of QPSK communication links is independent in the case of Gaussian noise, whereas in $S\alpha S$ noise it is correlated. The linear correlator is optimal in Gaussian noise, but performs

poorly in S α S noise. A soft-decision Viterbi decoder based on the Euclidean branch metric is optimal in Gaussian noise but performs very poorly in S α S noise. We developed a framework for analysis of communication links in S α S noise. We also developed computationally efficient near-optimal solutions such as the sign correlator for detection and the 1-norm Viterbi decoder for decoding of convolutional codes in presence of S α S noise.

Based on the understanding of the channel developed during the research, we proposed an OFDM based communication scheme for use in WSWA channels. We used differential QPSK and a cyclic prefix to eliminate the need for an equalizer. We used a convolutional code and a channel interleaver to effectively benefit from the time-frequency diversity available in the channel. The channel interleaver avoids the performance impact from correlated errors due to broadband noise impulses, correlated in-phase and quadrature components of noise and correlated fading. The use of 1-norm Viterbi decoding ensures good decoding performance in impulsive noise. We also adapted a method which uses properties of the cyclic prefix for symbol synchronization to work in presence of non-Gaussian noise.

Given estimates of channel coherence time and delay spread, we derived constraints on the choice of OFDM parameters. These constraints guided us to choose appropriate OFDM parameters such as the number of sub-carriers and prefix length. We used the channel model to simulate OFDM communications with selected parameters and validated our choice of parameters for sea trials. Finally, we demonstrated reliable communications in very shallow waters in Singapore at ranges of 800 m and 1 km. During the experiment, more than 27 kb of data was transmitted without errors at a data rate of 7.6 kbps at a range of 1 km. More than 54 kb of data was transmitted at 15 kbps and a BER of 10^{-4} or better at a range of 800 m.

We conclude that the proposed OFDM scheme with appropriate choices of parameters can provide good communication performance in WSWA channels.

9.2. Further Research

During this work, we have assumed a static transmitter and receiver. In many real applications for underwater mobile platforms, the transmitter and receiver may be moving with respect to each other. If the relative speed is large enough, Doppler compensation will be necessary for the recommended OFDM scheme to work. Carrier offset estimation and compensation in presence of S α S noise requires further research.

We also assumed single transducers for our research. Significant amount of work has been done in the last decade with MIMO systems, space-time coding and spatial diversity combining. To achieve maximum benefit from multiple transducers, this work needs to be integrated with our understanding of the WSWA channel and S α S ambient noise.

Even with a single transducer and a non-mobile environment, several improvements may be possible to the proposed OFDM communication scheme. For example, a soft output viterbi algorithm (SOVA) can be adapted to use the 1-norm branch metric. This will enable the use of iterative decoding techniques with serial concatenated codes and turbo codes to further improve decoding performance. Development of equalization techniques for OFDM in S α S noise may enable us to reduce the length of the cyclic prefix and increase the bandwidth efficiency of the communication link.

We currently filter out all out-of-band noise to maximize SNR. However, the broadband nature of the impulses in S α S noise introduces a correlation between the

out-of-band noise and in-band noise. Thus, by observing the out-of-band noise, we may be able to partially de-noise the signal before processing. A related idea has been explored in [39;40]. Further research is required to implement such a method in UWA communications.

Once UWA communication links can be reliably established, the next natural step is towards underwater networking. Preliminary research in UWA networks suggests that the requirements for such networks are significantly different from wireless networks [92;93]. The OFDM scheme developed here has to be evaluated and modified in light of requirements such as multiple access to the channel, carrier sensing, power control, etc.

Bibliography

- [1] J. A. Catipovic, "Performance limitations in underwater acoustic telemetry," *IEEE J. Oceanic Eng.*, vol. 15, no. 3, pp. 205-216, 1990.
- [2] M. Stojanovic, "Recent advances in high-speed underwater acoustic communications," *IEEE J. Oceanic Eng.*, vol. 21, no. 2, pp. 125-136, 1996.
- [3] A. B. Baggeroer, "Acoustic telemetry - An overview," *IEEE J. Oceanic Eng.*, vol. 9, pp. 229-235, 1984.
- [4] A. B. Coates and P. Willison, "Underwater acoustic communications: A review and bibliography," in *The Institute of Acoustics* 1987.
- [5] M. Chitre, J. Potter, and S. H. Ong, "Underwater acoustic channel characterisation for medium-range shallow water communications," in *IEEE Oceans 2004, Kobe, Japan 2004*, pp. 40-45.
- [6] J. R. Potter, T. W. Lim, and M. Chitre, "High-frequency ambient noise in warm shallow waters," in *Sea Surface Sound, UK* 1997.
- [7] J. R. Potter, T. W. Lim, and M. Chitre, "Ambient noise environments in shallow tropical seas and the implications for acoustic sensing," in *Oceanology International 97 Pacific Rim, Singapore*, 1 ed 1997, pp. 191-199.
- [8] D. B. Kilfoyle and A. B. Baggeroer, "The state of the art in underwater acoustic telemetry," *IEEE J. Oceanic Eng.*, vol. 25, no. 1, pp. 4-27, 2000.
- [9] M. Stojanovic, J. A. Catipovic, and J. G. Proakis, "Adaptive multi-channel combining and equalization for underwater acoustic communications," *J. Acoust. Soc. Am.*, vol. 94, pp. 1621-1631, 1993.
- [10] M. Stojanovic, J. A. Catipovic, and J. G. Proakis, "Phase-coherent digital communications for underwater acoustic channels," *IEEE J. Oceanic Eng.*, vol. 19, no. 1, pp. 100-111, 1994.
- [11] M. Stojanovic, J. G. Proakis, and J. A. Catipovic, "Performance of a high-rate adaptive equalization on a shallow water acoustic channel," *J. Acoust. Soc. Am.*, vol. 100, no. 4, pp. 2213-2219, 1996.
- [12] K. G. Kebkal, R. Bannasch, A. G. Kebkal, and S. G. Yakovlev, "Ultrasonic link for improved incoherent data transmission in horizontal shallow water channels," in *IEEE Oceans 2003, San Diego 2003*, pp. 1786-1792.
- [13] R. F. W. Coates, *Underwater acoustic systems*. New York: Wiley, 1989.
- [14] A. Essebbar, G. Loubet, and F. Vial, "Underwater acoustic channel simulations for communications," in *IEEE Oceans'94, France 1994*, p. III.

- [15] R. H. Owen, B. V. Smith, and R. F. W. Coates, "An experimental study of rough surface scattering and its effects on communication coherence," in *IEEE Oceans'94, Brest, France*, III ed 1994, pp. 483-488.
- [16] M. Badiey, Y. Mu, J. A. Simmen, and S. E. Forsythe, "Signal variability in shallow-water sound channels," *IEEE J. Oceanic Eng.*, vol. 25, no. 4, pp. 492-500, 2000.
- [17] R. Galvin and R. F. W. Coates, "Analysis of the performance of an underwater acoustic communication system and comparison with stochastic model," in *IEEE Oceans'94, France 1994*, p. III.
- [18] J. G. Proakis, *Digital communications*, 3rd Edition ed. Singapore: McGraw-Hill, 1995.
- [19] M. Zheng, "Experimental study on statistical characteristics of pulse transmission in shallow water," in *the Institute of Acoustics* 1993.
- [20] X. Geng and A. Zielinski, "An eigenpath underwater acoustic communication channel model," in *IEEE Oceans'95, San Diego*, 2 ed 1995, pp. 1189-1196.
- [21] G. A. Tsihrintzis and C. L. Nikias, "Performance of optimum and suboptimum receivers in the presence of impulsive noise modeled as an alpha-stable process," *IEEE Transactions on Communications*, vol. 43, pp. 904-914, 1995.
- [22] S. G. Wilson, *Digital modulation and coding*. New Jersey: Prentice-Hall, 1996.
- [23] L. E. Freitag, M. Stojanovic, S. Singh, and M. Johnson, "Analysis of channel effects on direct-sequence and frequency-hopped spread-spectrum acoustic communications," *IEEE J. Oceanic Eng.*, vol. 26, no. 4, pp. 586-593, 2001.
- [24] M. Stojanovic and L. E. Freitag, "Wideband underwater acoustic CDMA: Adaptive multichannel receiver design," in *IEEE Oceans'05, Washington DC* 2005.
- [25] S. B. Weinstein and P. M. Ebert, "Data transmission by frequency-division multiplexing using the discrete Fourier transform," *IEEE Transactions on Communication Technology*, vol. COM-19, pp. 628-634, 1971.
- [26] E. Lawrey, "The suitability of OFDM as a modulation technique for wireless telecommunications, with a CDMA comparison." James Cook University, 1997.
- [27] W. K. Lam and R. F. Ormondroyd, "A broadband UWA communication system: based on COFDM modulation," in *IEEE Oceans'97*, 2 ed 1997, pp. 862-869.
- [28] W. K. Lam and R. F. Ormondroyd, "A coherent COFDM modulation system for a time-varying frequency-selective underwater acoustic channel," in *Seventh International Conference on Electronic Engineering in Oceanography* 1997, pp. 198-203.

- [29] W. K. Lam, R. F. Ormondroyd, and J. J. Davies, "A frequency domain adaptive coded decision feedback equalizer for a broadband UWA COFDM system," in *IEEE Oceans'98*, 2 ed 1998, pp. 794-799.
- [30] W. K. Lam and R. F. Ormondroyd, "A novel broadband COFDM modulation scheme for robust communication over the underwater acoustic channel," in *Military Communications Conference (MILCOM 98)*, 1 ed 1998, pp. 128-133.
- [31] S. Coatelan and A. Glavieux, "Design and test of a coding OFDM system on the shallow water acoustic channel," in *IEEE/MTS OCEANS '95*, 3 ed 1995, pp. 2065-2070.
- [32] E. Bejjani and J. C. Belfiore, "Multicarrier coherent communications for the underwater acoustic channel," in *IEEE/MTS Oceans'96*, 3 ed 1996, pp. 1125-1130.
- [33] K. Byung-Chul and L. Tai, "Parameter study of OFDM underwater communications system," in *MTS/IEEE OCEANS 2000*, 2 ed 2000, pp. 1251-1255.
- [34] Y. V. Zakharov and V. P. Kodanev, "Multipath-Doppler diversity of OFDM signals in an underwater acoustic channel," in *IEEE International Conference on Acoustics, Speech, and Signal Processing (ICASSP), 2000*, 5 ed 2000, pp. 2941-2944.
- [35] R. Bradbeer, E. Law, and L. F. Yeung, "Using multi-frequency modulation in a modem for the transmission of near-realtime video in an underwater environment," in *IEEE International Conference on Consumer Electronics (ICCE), 2003* 2003, pp. 360-361.
- [36] L. F. Yeung, R. S. Bradbeer, E. T. M. Law, W. Angus, L. Bin, and Z. G. Gu, "Underwater acoustic modem using multicarrier modulation," in *IEEE/MTS OCEANS 2003*, 3 ed 2003, pp. 1368-1375.
- [37] F. Frassati, C. Lafon, P. A. Laurent, and J. M. Passerieux, "Experimental assessment of OFDM and DSSS modulations for use in littoral waters underwater acoustic communications," in *IEEE Oceans 2005 - Europe*, 2 ed 2005, pp. 826-831.
- [38] J. K. Wolf, "Redundancy, the Discrete Fourier Transform, and Impulse Noise Cancellation," *IEEE Transactions on Communications*, vol. COM-31, no. 3, pp. 458-461, 2005.
- [39] F. Abdelkefi, P. Duhamel, and F. Alberge, "On the use of pilot tones for impulse noise cancellation in Hyperlan2," in *International Symposium on Signal Processing and its Applications (ISSPA), Kuala Lumpur, Malaysia 2001*, pp. 591-594.
- [40] F. Abdelkefi, F. Alberge, and P. Duhamel, "Impulsive noise cancellation in multicarrier transmission," *IEEE Transactions on Communications*, vol. 53, no. 1, pp. 94-106, 2005.

- [41] M. Fink, "Time reversed acoustics," *Physics Today*, vol. 50, pp. 34-40, 1997.
- [42] W. A. Kuperman, W. S. Hodgkiss, H. C. Song, T. Akal, C. Ferla, and D. R. Jackson, "Phase conjugation in the ocean: Experimental demonstration of a time reversal mirror," *J. Acoust. Soc. Am.*, vol. 103, pp. 25-40, 1998.
- [43] G. F. Edelmann, T. Akal, W. S. Hodgkiss, S. Kim, W. A. Kuperman, and H. C. Song, "An initial demonstration of underwater acoustic communication using time reversal," *IEEE J. Oceanic Eng.*, vol. 27, pp. 602-609, 2002.
- [44] D. B. Kilfoyle, J. C. Preisig, and A. B. Baggeroer, "Spatial modulation over partially coherent multiple-input/multiple-output channels," *IEEE Transactions on Signal Processing*, vol. 51, no. 3, pp. 794-804, 2003.
- [45] S. Roy, T. Duman, L. Ghazikhanian, V. McDonald, J. G. Proakis, and J. Zeidler, "Enhanced underwater acoustic communication performance using space-time coding and processing," in *IEEE Oceans'04, Kobe, Japan*, 1 ed 2004, pp. 26-33.
- [46] D. Middleton, "Statistical-physical models of electromagnetic interference," *IEEE Transactions on Electromagnetic Compatibility*, vol. EMC-19, no. 3, pp. 106-127, 1977.
- [47] D. Middleton, "Canonical non-Gaussian noise models: Their implications for measurement and for prediction of receiver performance," *IEEE Transactions on Electromagnetic Compatibility*, vol. EMC-21, no. 3, pp. 209-220, 1979.
- [48] E. J. Wegman, S. C. Schwartz, and J. B. Thomas, *Topics in non-Gaussian signal processing* Springer-Verlag, 1989.
- [49] J. H. Miller and J. B. Thomas, "The detection of signals in impulsive noise modeled as a mixture process," *IEEE Transactions on Communications*, vol. COM-24, no. 5, pp. 559-563, 1976.
- [50] C. L. Nikias and M. Shao, *Signal processing with alpha-stable distributions and applications*. New York: Wiley, 1995.
- [51] W. Feller, *An introduction to probability theory and its applications (vol. II)*. New York: Wiley, 1966.
- [52] P. A. Nielsen and J. B. Thomas, "Non-parametric detection in underwater environments," in *International Conference on Acoustics, Speech, and Signal Processing (ICASSP-89)*, 4 ed 1989, pp. 2728-2731.
- [53] D. C. Bertilone and D. S. Killeen, "Statistics of biological noise and performance of generalized energy detectors for passive detection," *IEEE J. Oceanic Eng.*, vol. 26, no. 2, pp. 285-294, 2001.
- [54] A. D. Spaulding and D. Middleton, "Optimum reception in an impulsive interference environment - Part I: Coherent detection," *IEEE Transactions on Communications*, vol. COM-25, no. 9, pp. 910-923, 1977.

- [55] A. D. Spaulding and D. Middleton, "Optimum reception in an impulsive interference environment - Part II: Incoherent reception," *IEEE Transactions on Communications*, vol. COM-25, no. 9, pp. 924-934, 1977.
- [56] G. A. Tsihrintzis and C. L. Nikias, "Incoherent receivers in alpha-stable impulsive noise," *IEEE Transactions on Signal Processing*, vol. 43, no. 9, pp. 2225-2229, 1995.
- [57] C. E. Shannon, *The mathematical theory of information* Urbana, University of Illinois Press, 1949.
- [58] R. J. Urick, *Principles of underwater sound (3rd edition)*. New York: McGraw-Hill, 1983.
- [59] L. M. Brekhovskikh and Y. Lysanov, *Fundamentals of ocean acoustics (2nd edition)*. Germany: Springer-Verlag, 1991.
- [60] K. G. Kebkal and R. Bannasch, "Sweep-spread carrier for underwater communication over acoustic channels with strong multipath propagation," *J. Acoust. Soc. Am.*, vol. 112, no. 4 2002.
- [61] S. P. Tan, T. B. Koay, P. Venugopalan, M. A. Chitre, and J. R. Potter, "Development of a shallow water ambient noise database," in *Underwater Technology 2004, Taiwan 2004*.
- [62] R. J. Urick, *Ambient noise in the sea*. Los Altos: Peninsula Publishing, 1986.
- [63] T. B. Koay, E. T. Tan, M. Chitre, and J. R. Potter, "Estimating the spatial and temporal distribution of snapping shrimp using a portable, broadband 3-dimensional acoustic array," in *IEEE Oceans 2003, San Diego 2003*.
- [64] M. Chitre, T. B. Koay, and J. Potter, "Origins of directionality in snapping shrimp sounds and its potential," in *IEEE Oceans 2003, San Diego 2003*.
- [65] J. Chambers, W. Cleveland, B. Kleiner, and P. Tukey, *Graphical methods for data analysis* Wadsworth, 1983.
- [66] S. A. Kassam, *Signal detection in non-Gaussian noise*. New York: Springer-Verlag, 1988.
- [67] J. H. McCulloch, "Numerical approximation of the symmetric stable distribution and density," in *A practical guide to heavy tails*. R. J. Adler, R. E. Feldman, and M. S. Taqqu, Eds. USA: Birkhauser, 1998.
- [68] J. H. McCulloch, "Simple consistent estimators of stable distribution parameters," *Communications in statistical simulation*, vol. 15, no. 4, pp. 1109-1136, 1986.
- [69] E. F. Fama and R. Roll, "Parameter estimates for symmetric stable distributions," *J. Am. Stat. Assoc.*, vol. 66, pp. 331-338, 1971.

- [70] G. Snedecor and W. Cochran, *Statistical methods*, 8th ed Iowa State University Press, 1989.
- [71] I. M. Chakravarti, R. G. Laha, and J. Roy, *Handbook of methods of applied statistics, volume I*. USA: John Wiley and Sons, 1967.
- [72] G. Samorodnitsky and M. S. Taqqu, *Stable non-Gaussian random processes*. New York: Chapman & Hall, 1994.
- [73] E. Artin, *The Gamma Function*. New York: Holt, Rinehart, and Winston, 1964.
- [74] M. A. Chitre, J. R. Potter, and S. H. Ong, "Optimal and near-optimal signal detection in snapping shrimp dominated ambient noise," 2005.
- [75] M. A. Chitre, J. R. Potter, and S. H. Ong, "Viterbi decoding of convolutional codes in symmetric α -stable noise," 2005.
- [76] J. M. Chambers, C. L. Mallows, and B. W. Stuck, "A method for simulating stable random variables," *J. Acoust. Soc. Am.*, vol. 71, pp. 340-344, 1976.
- [77] R. Johannesson and K. Sh. Zigangirov, *Fundamentals of convolutional coding*. New York: IEEE Press, 1999.
- [78] P. Frenger, P. Orten, and T. Ottosson, "Convolutional codes with optimum distance spectrum," *IEEE Communications Letters*, vol. 3, no. 11, pp. 317-319, 1999.
- [79] T. Oberg and M. Mettiji, "Robust detection in digital communications," *IEEE Transactions on Communications*, vol. 43, no. 5, pp. 1872-1876, 1995.
- [80] X.-Y. Hu, C.-M. Zhao, and X.-H. Yu, "A robust Viterbi decoder and its application to terrestrial HDTV broadcasting," *IEEE Transactions on Broadcasting*, vol. 43, no. 2, pp. 227-234, 1997.
- [81] J. P. Odenwalder, "Optimal decoding of convolutional codes." Ph.D. dissertation, School of Engineering & Applied Science, University of California, Los Angeles, 1970.
- [82] R. Dashen, W. H. Munk, K. M. Watson, and F. Zachariasen, *Sound transmission through a fluctuating ocean* Cambridge University Press, 1979.
- [83] B. Sklar, *Digital communications: Fundamentals and applications*, 2nd ed. New Jersey: Prentice-Hall, 2001.
- [84] J. Bingham, "Multicarrier modulation for data transmission: An idea whose time has come," 1990, pp. 14-15.
- [85] B. Muquet, Z. Wang, and G. Giannakis, "Cyclic prefix or zero padding for wireless multicarrier transmissions?," *IEEE Transactions on Communication Technology*, vol. 50, no. 12, pp. 2136-2148, Dec.2002.

- [86] J. J. van de Beek, M. Sandell, and P. O. Borjesson, "ML estimation of time and frequency offset in OFDM systems," *IEEE Transactions on Signal Processing*, vol. 45, no. 7, pp. 1800-1805, 1997.
- [87] T. Keller, L. Piazzo, P. Mandarini, and L. Hanzo, "Orthogonal frequency division multiplex synchronization techniques for frequency-selective fading channels," *IEEE Journal on Selected Areas in Communications*, vol. 19, no. 6, pp. 999-1008, June 2001.
- [88] M. Luise, U. Mengali, M. Moeneclaey, J. G. Proakis, E. Strom, and W. H. Tranter, "Signal synchronization in digital transmission systems," *IEEE Journal on Selected Areas in Communications*, vol. 19, no. 12, pp. 2293-2297, 2001.
- [89] C. R. Nassar, *Multi-carrier technologies for wireless communication*. Boston: Kluwer Academic Publishers, 2002.
- [90] J. Tellado, *Multicarrier modulation with low par : applications to DSL and wireless*. Boston: Kluwer Academic Publishers, 2000.
- [91] M. Chitre, S. H. Ong, and J. Potter, "Performance of coded OFDM in very shallow water channels and snapping shrimp noise," in *IEEE Oceans'05, Washington DC* 2005.
- [92] E. M. Sozer, M. Stojanovic, and J. G. Proakis, "Underwater acoustic networks," *IEEE J. Oceanic Eng.*, vol. 25, no. 1, pp. 72-83, 2000.
- [93] S. Shahabudeen and M. Chitre, "Design of networking protocols for shallow water peer-to-peer acoustic networks," in *IEEE Oceans'05 Europe, Brest, France* 2005.